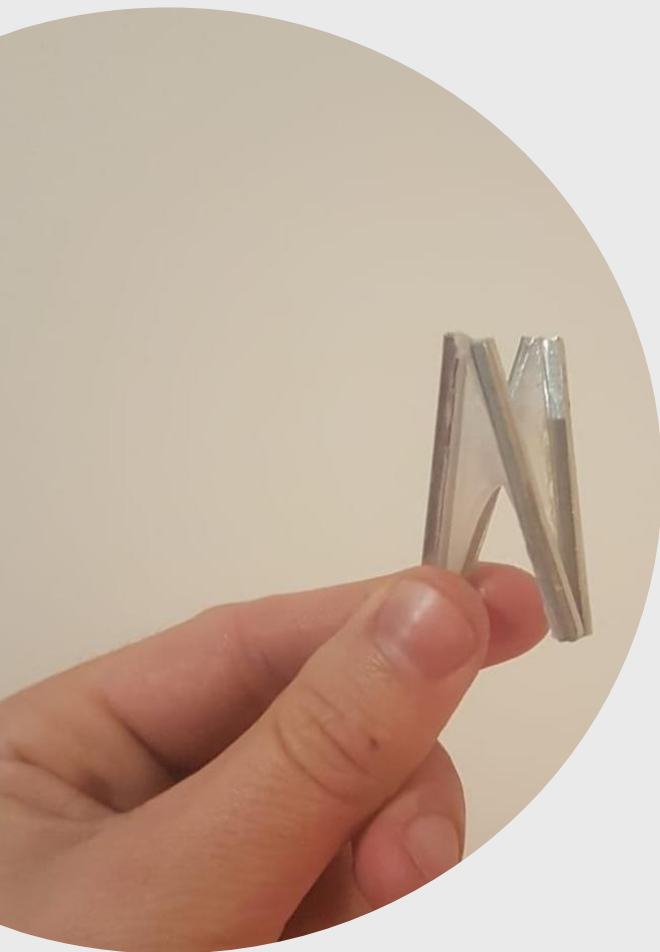


Shape-shifting of hyperbolic surfaces

Design and analysis of a shape-shifting method for complex hyperbolic surfaces, based on a passive frame in combination with an active shape-memory polymer.

R.J.C. Uyttendaele

Technische Universiteit Delft



Shape-shifting of hyperbolic surfaces

Design and analysis of a shape-shifting method
for complex hyperbolic surfaces, based on a
passive frame in combination with an active
shape-memory polymer

by

R.J.C. Uyttendaele

to obtain the degree of Master of Science
at the Delft University of Technology,
to be defended publicly on Friday April 3, 2020 at 10:00 AM.

Student number: 4256743
Project duration: April 1, 2019 – April 3, 2020
Thesis committee: Prof. dr. ir. A.A. Zadpoor, TU Delft, supervisor
Ir. S.J.P. Callens, TU Delft, daily supervisor
TU Delft, External committee member

This thesis is confidential and cannot be made public until April 3, 2021.

An electronic version of this thesis is available at <http://repository.tudelft.nl/>.

Acknowledgements

This thesis marks the end of an important period in my life. With this work, I proudly finish my life as a student having obtained a bachelor in Mechanical Engineering and Master in Biomedical Engineering. I really enjoyed this interesting and educational period and now I am looking forward to the new challenges lying ahead. This thesis and my period as a student would not have been a success without the help and support of several people.

Firstly, I would like to thank my daily supervisor Sebastien Callens very much. He supported me during my complete thesis and literature study and he came up with the basis of the researched idea. Sebastien always made time for me in order to help and to share his views, despite his own busy schedule and his period abroad. Next to that, Sebastien coached me during more difficult periods and kept believing in a positive outcome.

Secondly, my sincere gratitude goes to Prof.dr. Amir A. Zadpoor. Amir's interesting and inspiring course during my master, inspired me to graduate in the (bio)material science field. Next to that, Amir acted as the supervisor of this thesis work. During our meetings, Amir helped me to maintain focus and directed me towards the right objective.

Further, I am grateful for the support of different other researchers and technicians of the Biomaterials & Tissue Biomechanics department. They were always in for a nice chat, showed great interest in my work and gave me different ideas and insights. I especially want to thank Mirzaali Mazandarani for helping me with the 3D scanner and Sander Leeftang for his ideas and help in the Biomaterials lab.

Aside from those who helped me from an academic perspective, I would like to thank my close family and friends: My parents, for giving me the possibility and believe to accomplish my goals in life and for their unconditional love. My sisters, for their love and support and for keeping me down to earth whenever needed. My friends and roommates, with whom I have experienced beautiful, fun and memorable moments. Lastly, I of course want to express my sincerest gratitude to my lovely girlfriend Anne, she is always there for me and always knows how to put a smile on my face.

*R.J.C. Uyttendaele
Delft, April 2020*

Contents

1	Introduction	1
1.1	Porous and curved biomaterials	1
1.2	Shape-shifting	2
1.3	Shape shifting of hyperbolic structures	4
1.4	Research objective	6
1.5	Background: Curvature & minimal surfaces.	7
1.5.1	Curvature	7
1.5.2	Minimal surfaces.	7
2	Materials & Methods	9
2.1	The basic patch	9
2.1.1	Basic patch design	10
2.1.2	SMP materials	10
2.1.3	Frame materials and fabrication	11
2.1.4	Activation methods	11
2.1.5	Assembly.	12
2.2	Patch groups	12
2.2.1	3D-printed patch	13
2.2.2	Aluminium discrete patch	14
2.2.3	Aluminium continuous patch	16
2.3	Experimental set up.	17
2.3.1	3D-printed group	17
2.3.2	Both aluminium groups	17
2.3.3	Pre-strained SMP verification	17
2.4	Data generation and Measurement	18
2.4.1	Basic measurements	18
2.4.2	Scanning and cleaning.	19
2.4.3	Rotation, distance and global principal curvatures algorithm	20
2.4.4	Surface evolver and Hausdorff distance	20
2.4.5	Scan correction and curvature calculations	21
2.4.6	Statistical significance	22
2.5	FEM model	22
2.5.1	Design and assembly.	22
2.5.2	Material properties	23
2.5.3	Mesh.	23
2.5.4	Activation	23
2.6	Abbreviations & Acronyms	24
3	Results	25
3.1	Shape memory polymer behaviour	25
3.2	Behaviour of 3D-printed patches	26
3.2.1	Effect of hinge type.	26
3.2.2	Effect of foil type	30
3.3	Behaviour of aluminium discrete patches.	32
3.3.1	Effect of orientation	33
3.3.2	Effect of corner aspect ratio	34
3.3.3	Temperature and time effects	34
3.3.4	Effect of beam thickness	36
3.3.5	Scaling effects	36

3.4	Behaviour aluminium continuous patches	38
3.5	FEM model	39
3.5.1	Convergence	39
3.5.2	Analysis of stress and strain distribution	39
3.5.3	Validation	41
4	Discussion	45
4.1	Patch design for hyperbolic shape-shifting	45
4.2	Material selection for hyperbolic shape-shifting	48
4.3	SMP shape-shifting and the “idealized” minimal surface	50
4.4	Measuring hyperbolic shape-shifted patches	51
4.5	Outlook & applications	52
5	Conclusion	55
A	Decisions for basic design	57
B	Test matrix for different patch groups	59
C	Additional experiments	61
D	Other	63
	Bibliography	65

Abstract

Almost every tissue in the human body is curved in a certain way. Examples are the extracellular matrix of different tissues such as trabecular bone, different acini and blood vessels. As such, the ability to create complex curved structures is crucial in the development of biomimetic biomaterials that could be used, for example, for tissue regeneration purposes. Currently, most of these different curved substrates and porous materials are fabricated with 3D-printing techniques. These techniques, however, have limitations. The 3D-printed structures, for example, have limited resolution and the production process is not compatible with planar functionality-inducing processes. A solution for these problems could be the concept of shape-shifting. Shape-shifting is the process through which an object transforms itself into a different shape under the influence of an external stimulus, such as temperature or light. A special interest goes to shape-shifting of initially flat materials (2D) into different complex 3D structures. This method has as main advantage that planar printing, patterning or other 2D processing techniques can be used on the planar (non-shape-shifted) state. In this research, the most important principles of shape-shifting of curved hyperbolic surfaces are explored. With this technique, the benefits of both hyperbolic surfaces and shape-shifting can be combined and exploited. A new way of hyperbolic shape-shifting is introduced. This is done by using a passive rigid frame and an active shape memory polymer (SMP). The passive material determines how and where the structure will fold, while the active SMP generates the force in order to fold and forms a curved (hyperbolic) surface spanned between the frame. A simple square patch design consisting of four rigid beams and an SMP was used as the basis of this research. When activated, this patch forms a saddle shaped (hyperbolic) surface. The design, activation and materials of the patch were changed and manipulated in different ways in order to perform a parametric study and to analyse different important aspects of the process. In order to quantify and assess the quality of the different patches and the effects of the manipulations, different test set-ups were made and the most valuable output parameters were chosen. Lastly, a finite element model of the principle was developed in order to further analyse the concept.

It has been demonstrated that different changes in the design of the patch have a significant effect on the shape-shifting process. Hinges can manipulate how the patch folds and to what extent. In general, the following correlation is found: the further the patch folds and thus the more hyperbolic the shape-shifted patch becomes, the further the surface deviates from a minimal surface (surface with zero mean curvature). Another important design parameter is the thickness, and thus stiffness, of the frame. An equilibrium between the stiffness/thickness of the frame and the shrink force of the sheet has been demonstrated. In order to clarify this principle, a dimensionless parameter is formulated that permits a quantification of this relationship. Other trade-offs such as the aspect ratio between the corners of the frame, the size of the patch (scaling) and the activation method have shown to be important design considerations for the shape-shifting of hyperbolic surfaces. Furthermore, material choice for both the active SMP and the passive frame have shown to be of great importance. Examples are the shrink percentage, shrink type and thickness of the active material and the stiffness, temperature resistance and fabrication method of the passive frame material.

This research covers different aspects of the concept of hyperbolic shape-shifting with a passive frame and a heat shrinkable polymer and substantiates its potential. The research, however, also introduces new problems and questions that have yet to be solved. New combinations of both the frame (design) and SMP's should be tested in order to evaluate if similar effects occur and if the assumptions made in this research are correct. For future application, larger and more complicated curved structures should be shape-shifted, by connecting multiple patches. It is likely that larger structures will behave differently compared to a single patch and that different aspects such as frame mass and folding sequence will become more important. Lastly, the scaling of the concept should be elaborated further as the concept of shape-shifting hyperbolic surfaces has multiple applications in smaller scale (micro-scale) fields.



Introduction

This thesis work introduces a new method for the shape-shifting of complex hyperbolic surfaces. This concept has different interesting and relevant applications in the field of (bio)materials. In the introduction, first the relevance of curvature in biomaterials will be explained and the shortcomings in the current fabrication methods will be introduced. Secondly, the proposed solution to these shortcomings will be introduced: shape-shifting. Subsequently, the research objective with corresponding research questions is given. Lastly, a general explanation and definition will be given for curvature and curved surfaces, with a focus on minimal surfaces.

1.1. Porous and curved biomaterials

Research has shown that cells react to various physical cues in their surroundings. Different cellular processes such as tissue growth, cell differentiation and cell migration can be influenced and directed by these cues. Examples are the stiffness of the cell's surrounding, mechanical stretch and different geometrical cues [19][53][10]. These physical cues can be exploited when designing different artificial scaffolds and porous biomaterials. Curvature is known to be an important physical cue. It has been demonstrated in many studies that (hyperbolic) curved substrates can induce different cell reactions. This reaction of cells to curvature is called curvotaxis [4][48][3][58][57][35]. Almost every tissue in the human body is curved in a certain way. Examples are the extracellular matrix of different tissues such as trabecular bone, different acini and blood vessels. As such, the ability to create complex curved structures is crucial in the development of biomimetic biomaterials that could be used, for example, for tissue regeneration purposes [31][57]. A special interest goes to the biomedical/biomaterial possibilities of minimal surfaces structures. These are hyperbolic surfaces with a zero mean curvature, that locally minimize their surface energy. The definition of minimal surfaces is further explained in section 1.5. This type of hyperbolic surfaces is of special interest as it is demonstrated in previous research, that tissue growth is linked to surface tension [44]. Next to that, the extracellular matrix of trabecular bone approaches zero mean curvature [30]. By mimicking the (zero mean) curvature of different tissues or by exploiting other properties of minimal surfaces, they can be of great added value in the development of biomaterials (for tissue regeneration) [60][32]. Triply periodic minimal surfaces (TPMS) are a special type of minimal surfaces that show extra potential in the biomedical field. TPMS consist out of unit cells with zero mean curvature, which are translational in three dimensions. Porous biomaterials based on TPMS do not only have the benefit of having zero mean curvature, but also show excellent material properties such as permeability and elastic moduli for the use of biomaterials [61].

Currently, most of these different curved substrates and porous materials are fabricated with 3D-printing techniques. These techniques, however, have limitations. The 3D-printed structures have limited resolution and the production process is not compatible with planar functionality-inducing processes. Examples of these functionality-inducing processes are planar printing and imprinting techniques. These techniques could, for example, create (nano)patterns and structures on the surface of the material. These patterns can, amongst other, improve the optical, osteogenic and antimicrobial properties of the designed surface [6][20][22]. A solution for the fabrication problems of these structures could be the concept of shape-shifting (i.e. 4D-printing) [29].

1.2. Shape-shifting

Shape-shifting is the process through which an object transforms itself into a different shape under the influence of an external stimulus, such as temperature or light. This concept has multiple interesting applications and therefore emerges in different research fields. A special interest goes to shape-shifting of initially flat materials (2D) into different complex 3D structures. This method has as main advantage that planar printing, patterning or other 2D processing techniques can be used on the planar (non-shape-shifted) state. Afterwards, the material can be triggered to shape-shift in its final 3D form. This makes it possible to create complex 3D folded structures with an increased surface functionality, whereas this would not be possible if the materials were directly fabricated in their 3D shaped final form [9]. Other benefits are the easy transport and fabrication of flat materials as well as the fact that the flat material can initially be programmed to make certain pre-described motions when triggered [42]. Examples of applications for of 2D-to-3D shape-shifting are self folding furniture and architecture, grippers and robots, different sensors and electrical actuators and again a wide range of applications in the biomedical field [55] [28][46][51][47]. It has been demonstrated that cells and tissues react to different mechanical cues in their surroundings on both nano and microscale [45]. These cues can easily be added to the biomaterials, trough 2D-to-3D shape-shifting. Next to that, the curvature of the cell's surroundings also plays an important role in cell behaviour as previously explained in chapter 1.1 (curvotaxis). With the help of shape-shifting, these curved surroundings (curved biomaterials) can be fabricated easier, compared to conventional methods. This will be further introduced in chapter 1.3.

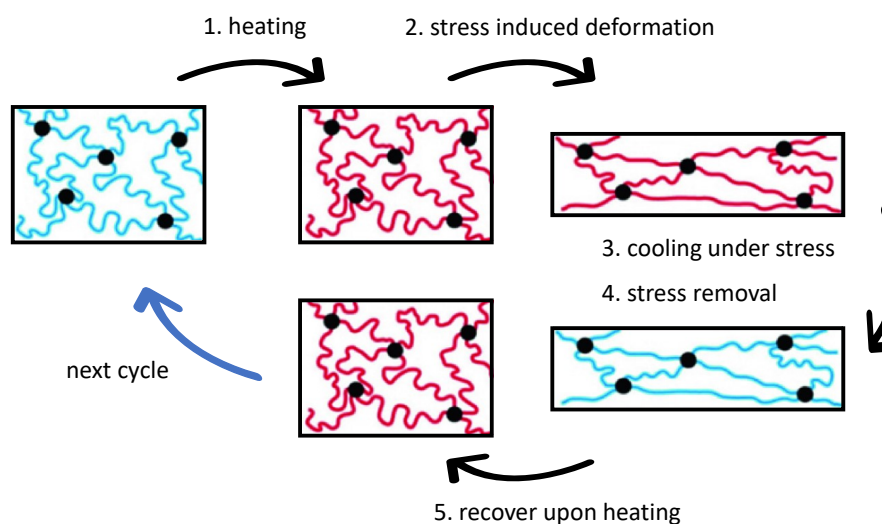


Figure 1.1: The complete cycle of programming and recovery of a shape-memory polymer (SMP) is shown. 1 First the material is heated above its glass transition temperature. 2 An external stress is applied to the material, while the material is continuously heated. By doing this, the material is deformed. 3 The material is cooled below its glass transition temperature, while the stress is still being applied. 4 The stress is taken away and the material stays in its deformed shape. 5 When the material is heated again, it will return to its initial shape. Important to notice is that in order to start the cycle again a new external stress has to be applied. Only changing the temperature would not be sufficient and this is why the process is irreversible [59]

There are different ways to create 2D-to-3D shape-shifting components. In all cases an active material is needed, that can be triggered by a certain external stimulus. In this work, we will focus on a special type of active materials used for shape-shifting: shape-memory polymers (SMP's). SMP's are polymers that can store their initial shape and recover it, by applying a heat stimulus. The polymer in its initial shape is first heated above its glass transition temperature. By doing this, the polymer comes in its rubbery state and can be deformed easily. This deformation is achieved by applying an external stress to the material. Subsequently, the deformed material is cooled down, while the stress is still being applied. Now the material is back in its glassy state and it will maintain its deformed state even when the stress is taken away. This complete process is called the programming of the material. When the polymer is heated again above its glass transition temperature, it will shrink back to its initial shape. This is called the recovery phase of the SMP [62] [59]. A visualisation of the complete cycle is given in figure 1.1.

It is also important to take the different ways of programming into consideration and how this influences the

behaviour of different SMP's. In most cases the SMP's are strained in one direction during their programming. This means that the material will only shrink unidirectionally when activated. For some applications, however, an isotropic SMP is more suitable. These materials are strained evenly in all directions during their programming. This process is more difficult, but can be used for more complex applications. Lastly, there are also materials that are strained in different directions, but not isotropically. This will result in an anisotropic shrinking process. Different studies have shown that these differences can have a significant effect on how the shape-shifting material will behave [17] [42] [63].

SMP's have the great advantage that they have excellent mechanical properties, when used below their glass transition temperature. Next to that, there are different bio-compatible and biodegradable SMP's, which make them of special interest in the field of (bio)materials [36] [56]. A downside is that the process of shape-memory polymers is irreversible, without applying a new external stress to the material. This makes it not suitable for certain shape-shifting applications [42]. On the other hand, in multiple applications, it is not desirable that the design changes again after activation. So this property could also be seen as an advantage in order to make mechanically strong and robust shape-shifted materials.

In 2D-to-3D shape-shifting, the material should deform out of plane, or in other words, there should be an out of plane movement in order to create a 3D shape. This can only be achieved if there are differences in the shrink ratio of the material of the initial 2D design. If the complete 2D design would have the same shrink rate, it would of course stay a 2D object and only become smaller when heated. There are multiple methods to achieve this out of plane deformation using SMP's. In order to give a clear overview, we have divided these methods into four main types:

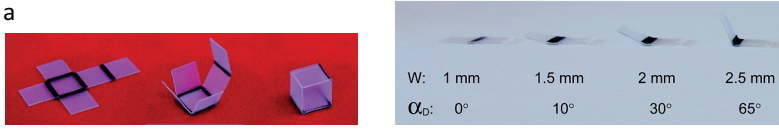
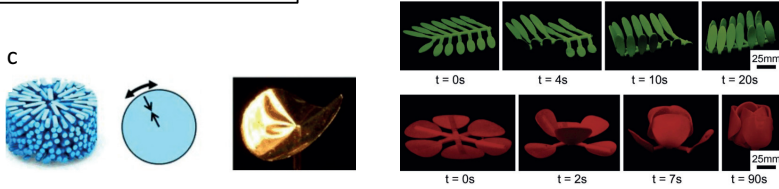
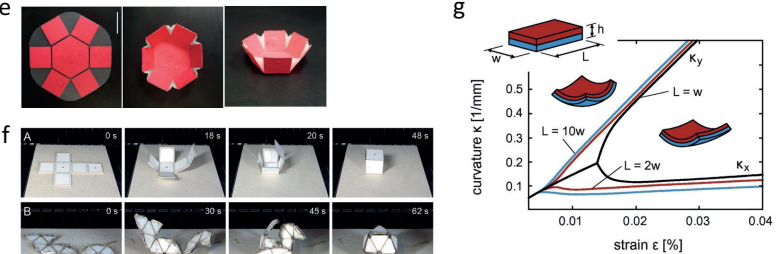
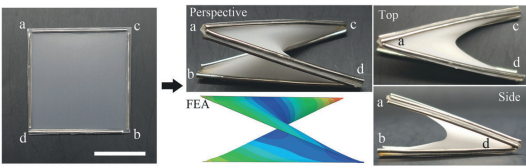
1. The first method makes use of selective or local heating of one single material. With this method, certain parts of the same material are activated and shrink, while the rest of the material does not shrink (or to a lesser extent). This can, for example, be achieved by colouring certain parts of the material black and subsequently heating the material with an IR lamp [38]. The major benefit of this method is the simplicity of most of the designs and the fact that it can be used on one single material.
2. The second method also uses one single material, but here certain parts of the material itself are manipulated. The material is, for example, pre-strained in certain regions during its production process. When the complete design is heated, these pre-strained regions will shrink faster. This creates the desired out of plane motion [41]. Fabrication with this method is in general more complex compared to the previous method. However, more complex shapes can be accomplished.

The desired out of plane motion can also be created by the use of two or multiple materials, that all have different shrink rates. One material (or a group of materials) can be seen as active and the other material (or group of materials) can be considered passive. In general the active shape-memory polymer generates the force in order to create the deformation and movement, while the passive material determines how and where the design is going to fold. There is a clear distinction between two groups, listed as shape-shifting methods 3 and 4 here below:

3. In the first group the passive material forms the largest and most important part of the design, when shape-shifted. Planar sheets of (semi) rigid materials are triggered to fold in a certain way by the attached SMP. Benefit of this method is its robust folding. However, it is very difficult to create curved designs as in most cases the planar sheets are only rotated and translated around each other and not curved.
4. In the second group the active SMP forms the largest and most important part of the shape-shifted material. Here, the passive material is in general a certain frame or a combination of rigid beams. When activated, the active material spans itself between this frame. This does not only create the desired out of plane motion, but also a curved (hyperbolic) surface spanned between the frame. This is exactly what makes this last method so interesting. With relatively simple 2D designs, complex and highly curved 3D objects can be created. As Callens et al. explained in their paper, you can not create intrinsically curved substrates from flat sheets, if the material is not expanded or shrunk in a certain way [8]. Using the last method this difficult problem is resolved.

An overview with examples of the four different methods is given in table 1.1, together with their main advantages and disadvantages.

Table 1.1: The four different methods in order to create out of plane deformation during shape-shifting from 2D-to-3D are presented with their corresponding (dis)advantages. For each method examples are given. a: A pre-strained SMP is activated locally, by colouring certain areas black and activating them with an IR-lamp. As proof of concept a square box is folded [38]. b: Here graphene ink is used in combination with microwaves. The microwaves heat and activate the parts coloured with graphene ink [17]. c: Polymer chains are bundled and aligned in different directions. When triggered these differences will create an out of plane deformation. In this example the bundles are aligned radial, creating a concave shape [25]. d: With the use of simple 3D-printing techniques and different printing characteristics, the printed material can be manipulated. By smart use of this concept certain shape-shifting sequences can be programmed. Here two complex shapes (a leaf and tulip) are folded using this method [41]. e: Shape-shifting is accomplished by planar rigid sheets combined with active SMP at the creases [16]. f: Again shape-shifting is accomplished with the use of planar rigid sheets and active SMP at the creases. In this example a shape-shifting cubic and icosahedron box are created [52]. g: A bilayer sample consisting of an active and a passive material is shown. This results in a convex shape when activated, due to the strain differences. In the table, curvature is given as a parameter of the strain difference and different dimensions [42][1] h: Shape-shifting with an active pre-strained SMP sheet constrained by a rigid frame. In this case, the initial frame is a square created by four rigid beams. When activated, it results in a saddle shaped sample [16].

<p>1. One material local/selective activation</p> 	<ul style="list-style-type: none"> + Single material + Simple fabrication + Distinct hinge - Limited curvature - Difficult initiation - Difficult for complex and larger/repeating structures - Imperfection sensitive - Soft materials only
<p>2. One material locally manipulated</p> 	<ul style="list-style-type: none"> + Single material + Complex small shapes + Uniform initiation - Limited curvature - Difficult for larger/repeating structures - Complex fabrication - Soft materials only
<p>3. Two or multiple materials, with passive material as main surface</p> 	<ul style="list-style-type: none"> + Robust folding + Uniform initiation + Rigid structures - Highly limited curvature - Difficult for complex structures and (3D) larger/repeating structures - Complex fabrication
<p>4. Two or multiple materials, with active material as main surface</p> 	<ul style="list-style-type: none"> + Complex curvature possible + Repeating/larger structures + Uniform initiation + Rigid structures - Imperfection sensitive

1.3. Shape shifting of hyperbolic structures

Until now, complex hyperbolic surfaces and especially triply periodic minimal surfaces (TPMS) are fabricated with 3D-printing. As discussed earlier, this entails the downside that the surface cannot be manipulated by planar printing, patterning or other 2D processing techniques. By directly shape-shifting the desired hy-

perbolic surface from an initially flat 2D configuration, this limitation is avoided. This way, the benefits of both curved (hyperbolic) surfaces and shape-shifting can be combined and exploited. The earlier introduced shape-shifting method 4 is most beneficial when shape-shifting these structures. With relatively simple 2D designs, complex and highly curved 3D objects can be created. The other methods can not create highly curved surfaces, need complex material programming in order to do so or are only compatible with relatively soft materials.

The idea of shape-shifting hyperbolic surfaces with this method is relatively new and hardly researched. One concept of it is introduced by Callens et al [9]. In their paper they describe a way to fold TPMS structures with the help of a pre-strained elastomer and a rigid frame. A TPMS can be divided into repeating unit cell's, which can be seen as the basic 'building block' of TPMS. Callens et al. show in their paper that these unit cells subsequently can be divided into relatively simple self folding patches, that can be formed through 2D-to-3D shape-shifting. An example of the folding patches and unit cells for a Schwarz P TPMS is given in figure 1.2a. By combining and attaching these patches to each other in certain sequences, unit cells and - in the end - complete TPMS materials can be folded from an initially flat 2D material. In their paper, Callens et al. mainly focus on the concept itself and only introduces a small proof of concept, with a rigid frame and a pre-strained elastomer. The idea is not proven to work for SMP's, although SMP's show great benefits over simple pre-strained elastomers. They especially have better mechanical properties and in addition, they can be made bio-compatible and biodegradable [36] [56]. Cui et al. introduced a so called 'minimal surface gadget' in their paper [16]. Here they show that an initial square patch consisting of four rigid beams in combination with a pre-strained SMP, forms a (minimal surface) saddle when activated (see figure 1.2b). The concept is introduced, but further research and elaboration is still missing. In our research, we want to take a step back and analyse the basic concept of shape-shifting of hyperbolic surfaces with a simple rigid frame and an SMP. As a basis, the simple square patch design with four rigid beams is chosen. This design is changed and manipulated in different ways in order to find relevant and important information about the concept. The idea is that this fundamental research can make a start in the development of shape-shifting of hyperbolic surfaces with SMP. Subsequently, this research can contribute to the shape-shifting of more complex curved (minimal) surfaces and intrinsically curved designs, such as the folding of complex TPMS materials. The great benefit of using a rigid frame in combination with an active SMP, is that the frame can be used as a guide that determines how and where the design is going to fold, while the active material is used to activate the shape-shifting and subsequently spans itself between the rigid frame, creating a curved surface.

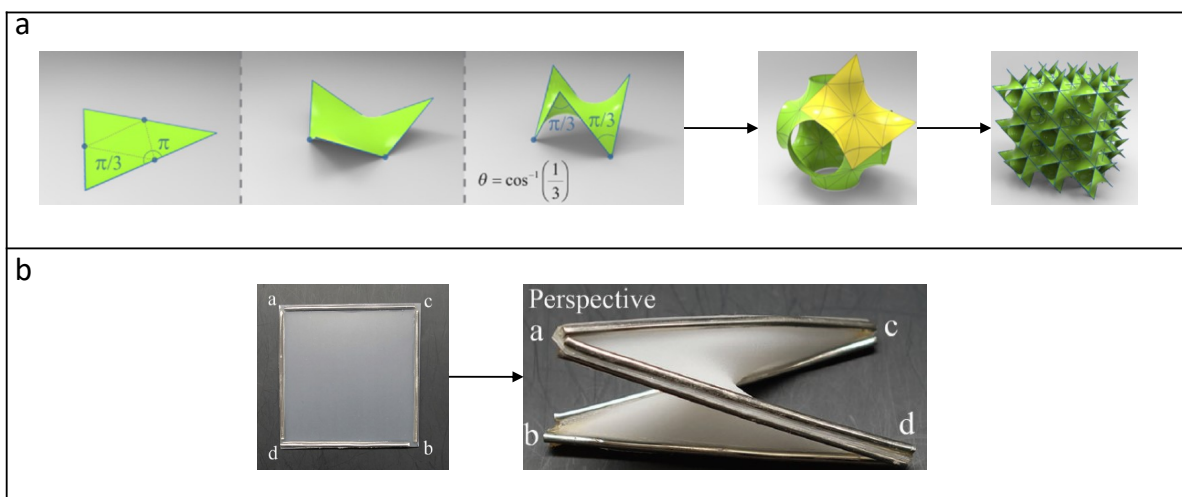


Figure 1.2: a: On the left, the folding from 2D-to-3D of a single patch is shown. The middle image shows a unit cell of the TPMS in green. In yellow a folded single patch is shown, multiple folded patches can form a unit cell, when they are correctly connected. Subsequently, when even more patches are connected, larger TPMS structures can be created as shown on the right. Important to notice is that these patches are connected in their initial 2D flat state and are afterwards shape-shifted into the desired TPMS. This particular example is for a Schwarz P TPMS, but the idea is also applicable for different other TPMS structures. [9]. b: Shows the folding of the so called 'minimal surface gadget' introduced in the paper of Cui et al [16]. A square frame consisting of four rigid beams is glued on a sheet of pre-stretched SMP. When activated this combination forms a saddle shape.

1.4. Research objective

In this research, we want to discover the basic and most important principles of shape-shifting of hyperbolic surfaces. As discussed before, the use of a passive rigid frame and an active SMP is best suited for this application of shape-shifting. We have chosen a basic design of a square patch with four rigid beams as the basis of this research. When activated, this patch will form a saddle shaped surface. The design and materials used will be changed and manipulated in different ways in order to perform a parametric study and to test the effects of different input parameters. This will be further explained and elaborated in chapter 2. Examples include changes in the materials of both the rigid beams and the SMP, different designs of hinges between the four beams and changes in the patch size. In order to quantify and assess the quality of the patch and the effects of the manipulations, different test set-ups will have to be made and the most valuable output parameters will need to be chosen. Lastly, a finite element model will be made in order to further investigate the concept. The scope and main focus of this thesis can be summarized with the research objective shown below. Subsequently, this objective is divided into five main research questions. They are each introduced and briefly explained below.

"The purpose of this research is to explore the combination of rigid frame elements and heat shrinkable polymer sheets as a basis for hyperbolic shape-shifting, by selecting suitable material combinations, designing and manufacturing the structures, constructing test set-ups for the analysis of these structures, and lastly by modelling the concept using finite element simulations."

1. What are the different ways hyperbolic shape-shifting with rigid frame can be designed and manufactured, what are the advantages and disadvantages of these different designs? The basic design chosen can be changed and adjusted in different ways. All these different design solutions will have effects on the final shape-shifted patch. Also, consideration needs to be given to how this design can be manufactured, what the most convenient production process is and even whether it is possible at all to manufacture the chosen designs. Next to that, the activation method is an important parameter in the process. The SMP has to be activated with the application of heat, which can be done in different ways.

2. What are suitable materials to be used in hyperbolic shape-shifting for both the frame and sheet? As explained earlier, differences in the chosen SMP can have major effects on the design. Will an anisotropic SMP for example, have a different effect compared to an isotropic SMP? Also differences in the passive rigid material can be tested. Lastly, the choice of materials is also related to the design, manufacturing process and activation method.

3. How can the quality of the self-folding methods be experimentally quantified, taking into account different important aspects of the shape-shifted hyperbolic surfaces? The quality of the patch has to be assessed. Is it for example even possible to create hyperbolic surfaces with this methods and how close can the special case of hyperbolic surfaces with zero mean curvature (minimal surfaces) be approached? Decisions have to be made on how to measure and quantify this. Next to that, other important aspects and parameters have to be found in order to quantify the complete process.

4. How can the basic patch design be modelled and is it possible to subsequently analyse the shape-shifting process with this model? This model could be used to do different parametric studies on the basic design, without the need of creating 'real life' patches. Next to that, different insight in the concept can be given with for example a stress analysis.

5. What are the difficulties and important key factors when scaling the concept? The concept of shape-shifting hyperbolic surfaces has multiple applications in the smaller scale (micro-scale) fields. Production of the patches on this scale is not yet possible, mainly because of fabrication difficulties. It is, however, of clear added value to already assess important factors that will play a role, when scaling the concept.

1.5. Background: Curvature & minimal surfaces

Basic knowledge of curvature is needed in order to understand different aspects of this thesis. Curvature is an ambiguous concept and a small introduction will be given for a basic understanding of the definition of curvature. Subsequently, a special interesting group of curved surfaces, minimal surfaces, is further explained. For a more elaborate explanation of curvature, we advise you to read the paper of Callens et al. [8].

1.5.1. Curvature

There are two important measures to define surface curvature on a certain point: Gaussian curvature (K) and mean curvature (H). Their equations are stated below (1.1 and 1.2).

$$K = k_1 \cdot k_2 \quad (1.1)$$

$$H = \frac{1}{2}(k_1 + k_2) \quad (1.2)$$

The k_1 and k_2 used in both formulas are called the principal curvatures of the surface at a certain point. This is the minimum and the maximum value of normal curvature of a chosen point in the surface. The concept of principal curvatures is most easily explained with the help of the normal vector perpendicular to the surface. Through this normal vector, multiple normal planes can be plotted. The easiest way to do this, is to choose a normal plane randomly as a starting point and subsequently to rotate the plane around the normal vector with a certain step size. Each normal plane has an intersection with the surface and this intersection can be seen as a curve with a certain 'normal' curvature. The maximum and the minimum curvature of all the different curves intersecting the different normal planes, are the principal curvatures. This idea is clearly visualized in figure 1.3. A flat surface for example has two principal directions of zero, so both the mean and the Gaussian curvature will be zero. A cylinder on the other hand has one principle direction that is zero and one principle direction that is positive or negative, depending on whether you take your reference point inside or outside the cylinder. This means that a cylinder has a negative or positive mean curvature, but a Gaussian curvature that equals zero. This is explained by the fact that the Gaussian curvature is the multiplication of the two principal directions. A saddle/hyperbolic surface is a surface with a negative Gaussian curvature as both principal curvatures are of opposite sign. With these two definitions, every curved surface can be defined.

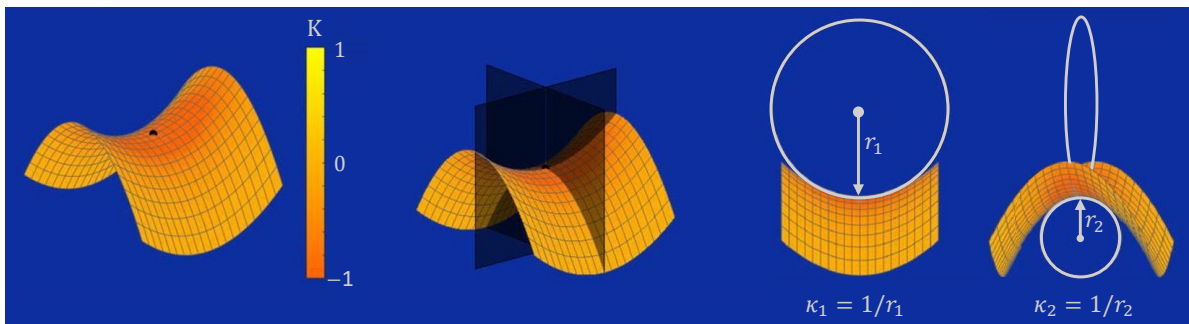


Figure 1.3: This figure visualizes the concept of the maximum and minimum principal curvature for a certain point on a curved surface (k_1 and k_2). On the left the chosen point is shown and subsequently the two normal planes through this point containing the maximum and minimum 'normal' curvature are visualized in black. Of course there are more normal planes for this point, but we are only interested in the two that contain the principal directions. The intersection of each normal plane and the surface is a curve, from this curve the curvature can be calculated as shown. The maximum and minimum value of all the different curves intersecting the different normal planes, are the principal curvatures [8].

1.5.2. Minimal surfaces

The concept of minimal surfaces was first described by Lagrange in the 18th century. However, at that time this discovery was mainly out of mathematical interest. The last decades, the concept of minimal surfaces regained attention. It shows high potential in different new (metamaterial) fields of study. In our study, a special interest goes to the biomedical/biomaterial possibilities of minimal surfaces as explained earlier. The easiest way to define a minimal surface is by its surface curvature. Minimal surfaces can be seen as a special type of hyperbolic surfaces and have a constant zero mean curvature throughout the surface. In other words,

they are surfaces with two equal principal curvatures, but of opposite sign. Flat surfaces are officially also minimal surfaces, because both their principal directions are zero. Such flat minimal surfaces will, however, be disregarded in this research. The Gaussian curvature of minimal surfaces can change continuously, but is zero or of negative sign. Minimal surfaces are surfaces that minimize their overall surface energy within a certain bounded configuration [18]. In order to do this, they create the smallest possible surface area between the bounded configuration [18]. Due to their surface area minimization, these minimal surfaces have zero mean curvature. This can be derived from the Young-Laplace equation 1.3 [34]. This equation states that the pressure difference (Δp) on a liquid film is proportional to the mean curvature (H), multiplied with the surface tension (σ) times two. As the surface tension and pressure difference is equal over the complete surface in case of a minimal surface, the mean curvature has to be zero. Simple examples of minimal surfaces are soap bubbles and soap films spanned between a frame, as shown in figure 1.4 [24].

$$\Delta p = 2\sigma H \quad (1.3)$$

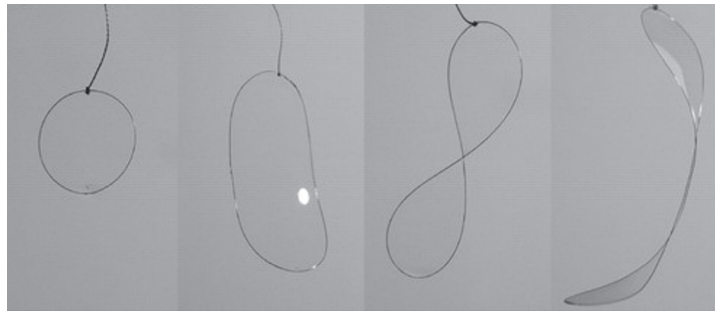


Figure 1.4: Example of soap films forming minimal surfaces between different bounded configurations [24].

2

Materials & Methods

This chapter consists out of five main sections. First the basic patch design will be introduced and further elaborated together with the chosen fabrication method, materials and activation method. This design forms the basis of this research. In order to completely cover and test all aspects of the concept, this basic design will be adjusted and manipulated in different ways. This results in different patches all of which are derived from the basic design. In order to give a clear overview, these patch types are divided in three different groups. These different groups will be introduced and subsequently for each group the different input parameters per group will be discussed. These different parameters are summarized in a test matrix for each group, which can be found in Appendix B. Subsequently, the different experimental set-ups will be explained for the activation of the different patch groups and for the verification of the chosen pre-strained shape-memory polymers (SMP's). Thereafter, the different chosen output parameters will be introduced and it will be explained how these data are measured and generated. Lastly, the finite element model (FEM) of the concept will be explained.

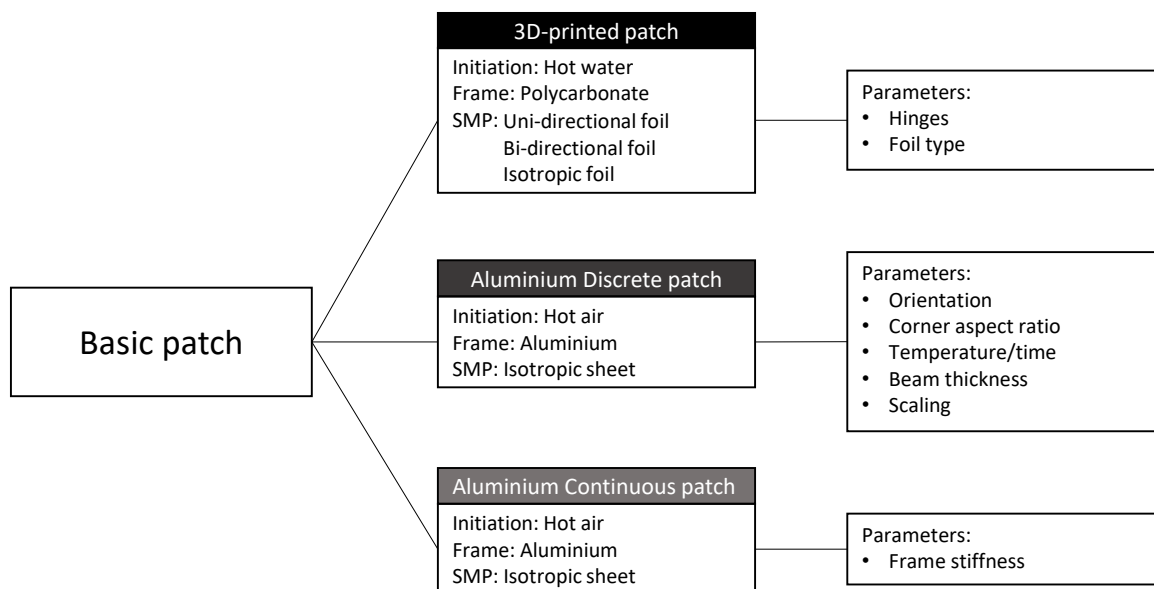


Figure 2.1: The basis of our design is called the basic patch and is introduced in section 2.1. From this patch three different groups can be derived, each with their own characteristics. For each of the three different groups, multiple different aspects (input parameters) of the concept can be investigated.

2.1. The basic patch

The concept of shape-shifting with a rigid frame and a thermally-activated SMP can of course be carried out in many different forms. First a study was done to consider and analyse the different possibilities and choices.

An overview of the different ideas has been added to the appendix A. We chose to use a square design based on the research of Cui et al. as the basis of our research [16]. This design is chosen due to its simplicity, making it suitable for parametric testing of the concept. Three different groups can be derived from this basic design, each testing their own aspects (input parameters) of the concept. An overview is given in figure 2.1. In this section the basic design will be introduced, together with the chosen materials, fabrication methods and activation methods.

2.1.1. Basic patch design

Our basic patch consists out of four rigid beams with an outer length of each 45 mm. The section area of the beams will be 3 mm width and 2 mm thick. These four beams will be placed in a square and will be attached to a pre-strained SMP sheet with an area corresponding to the outer area of this square. At both ends the beams are cut diagonally at an angle of 45°. This is the reason that the outer length of the beams is 45 mm, but the inner length is 39 mm. Due to these corners it is possible to correctly fit the four beams into one single square. In the basic design, the distance between the beams in the corners is taken at 1 mm. At these locations the beams can rotate around each other, when the patch is activated. This means that in the basic design, the corners are only restricted by the SMP of 1 mm between the beams as the four beams itself are not connected. It is important to note that the 'active' area of the SMP or in other words the area that will form the curved surface when activated, is smaller compared to the complete area of the SMP. This is due to the fact that part of the SMP is attached (glued) to the frame and can therefore not be part of the curved substrate when activated. The complete design of the basic patch is shown in figure 2.2.

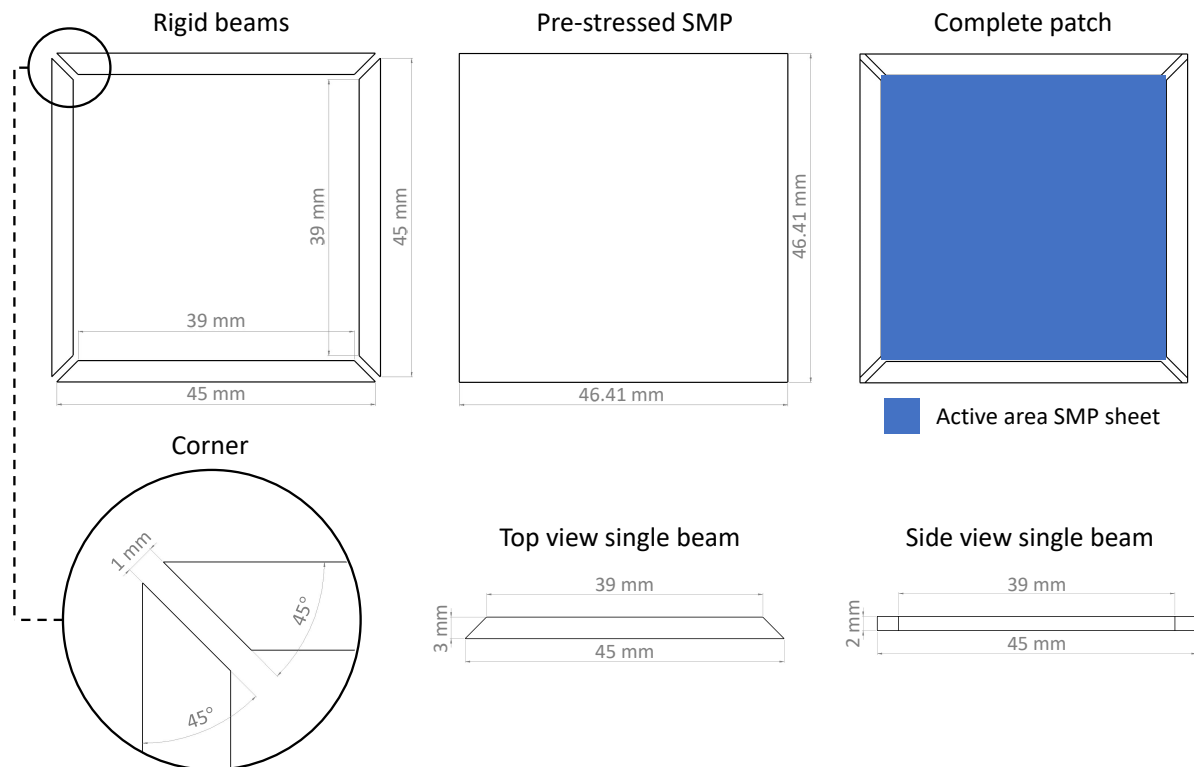


Figure 2.2: The design and dimensions of the basic patch. On the top left, the four beams are shown in their correct configuration. In the upper middle the pre-strained SMP sheet is shown. On the top right, the assembled combination of rigid beams and SMP is shown. In blue the so called 'active' area of the SMP sheet is marked. At the bottom of the figure, a close-up of the corner design is given and the design of a single beam is shown in different perspectives.

2.1.2. SMP materials

Different types of pre-strained thermally-activated SMP's were used. The first distinction can be made between foils and sheets. foils are thinner materials that have the advantage that their activation temperature is relatively low. Next to that, they do not completely harden after the shrink process. This means that the material has to be spanned between a frame in order to create a rigid patch. The foil itself will not create any

rigidity. The thicker sheet material on the other hand will harden when fully shrunk and thus can itself take care of the stiffness of the patch. However, these sheet materials typically need a higher activation temperature. The second important distinction between SMP's is their shrink type. They can be divided in isotropic shrink material that uniformly shrinks the same extent in all directions, an uneven bidirectional shrink material that shrinks in both directions but to a different extent and lastly a unidirectional material that only shrinks in one direction. These different types of SMP will have different effects on the shape-shifting process. An overview of the final different pre-strained SMP's used is given in table 2.1.

Table 2.1: The four different pre-stressed SMP materials used in this research. A clear distinction can be made between foils and sheets and between the different shrink types. Further information about the activation methods and temperatures will be given in the section 2.1.4. The ideal activation temperature is the temperature recommended by the manufacturer.

Name used	Type	Shrink type	Company	Material	Thickness	Ideal activation temp (°C)	Activation method	Activation temp (°C)
Unidirectional foil	foil	unidirectional	Eshuis	PET	45 μm	+/- 90	Boiling water	100
Uneven bidirectional foil	foil	bidirectional	Magicwater	PVC	25 μm	+/- 135	Boiling water	100
Isotropic foil	foil	isotropic	Balore	PE	19 μm	90-150	Boiling water	100
Isotropic sheet	sheet	isotropic	Shrinkme	PS	+/- 0.2 mm	170	Oven	170

2.1.3. Frame materials and fabrication

The choice of frame material depends on the pre-strained SMP they are combined with. The frame material has to be able to resist the activation temperature of the SMP's and also provide enough stiffness to act as a rigid frame. The decision has been made to use two different materials and fabrication methods for the frame. The isotropic sheets have a higher activation temperature and therefore aluminium is used for the frame. This frame is cut from an aluminium sheet with the help of a laser cutter. The foils have a lower activation temperature and a different fabrication method for the frame can be used for the frame. They will be 3D-printed with the help of an ultimaker 2+. With this ultimaker, the design can be changed more precisely and accurately. Compliant hinges can, for example, be added to the design, where this is not possible with aluminium and a laser cutter. After testing different materials compatible with an ultimaker, polycarbonate(PC) is chosen as a material for printed frames. This is because of its relatively high glass transition temperature and its elastic modulus around 2000 MPa [54]. This elastic modulus makes it suitable for printing compliant hinges. An overview of both materials is shown in table 2.2.

Table 2.2: The two chosen frame materials are shown. The aluminium frame is laser-cut and can resist high activation temperatures. The Polycarbonate (PC) frame is printed with an ultimaker 2+ and has a relatively low glass transition temperature [54].

Material	Fabrication	E modulus (MPa)	Glass transition temperature (°C)	Key characteristics
Aluminium	Laser cutter	69000	-	- High elastic modulus and melting point - Compatible with sheet SMP material
Polycarbonate (PC)	Ultimaker 2+	2134	112	- Lower elastic modulus - Relatively high glass transition temperature - Not compatible with sheet SMP material - Possibility of more complex designs

2.1.4. Activation methods

In every design process, fabrication, material choice and design choice are inextricably linked to each other. In our design, however, it is important to note that not only the classic three aspects of fabrication, material and design play a role. The activation method, or in other words the way the shape-shifting is triggered, is a fourth aspect that influences the other three. This is visualized in figure 2.3a. In our case, this activation is heat, but this can of course be applied in multiple different ways. An overview of the different tested possibilities is shown in the appendix in figure A.3. In our case we have chosen to activate the two material types (sheet and foil) in different ways. The foil materials will be activated by immersing the patch in boiling water. Because the foils are very thin, other activation methods will not uniformly heat the material resulting in an unequal shrinkage of the foil. For the thicker sheet material, activation with hot air in an oven was chosen. Submerging the sheet material in boiling water would not satisfy as the activation temperature of the sheet is higher than 100 °C. Because of the thickness of the sheet, the non-uniform heating does not occur when heating it with hot air. For now, these two methods are the most useful as the patches can be heated uniformly. In the future, however, larger structures will be created by different patches attached to each other. In that case it would be useful to heat some patches earlier than others, this concept is called sequential folding. In case of sequential folding method other than hot air and boiling water, would be more beneficial. Both chosen activation methods are shown in figure 2.3b and 2.3c.

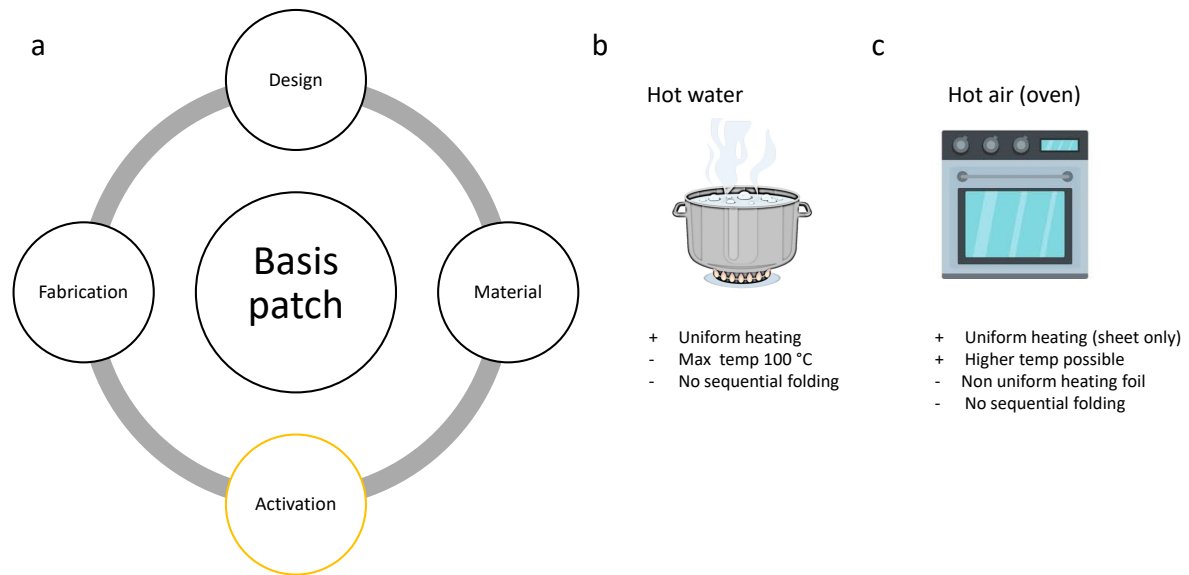


Figure 2.3: a: As in most design projects, design, fabrication and material choice are inextricably linked. There is however a fourth important marker in our design process that influences the others, which is the chosen activation method. b: The first chosen activation method and its main (dis)advantages. This method will be used for the activation of the foil SMP's. c: The second chosen activation method and its main (dis)advantages. This method will be used for the activation of the sheet SMP's.

2.1.5. Assembly

All frames are glued on the pre-strained SMP's. For the thicker isotropic sheet, a basic cyanoacrylic adhesive is used (Bison Super Glue liquid CONTROL 3g). The thinner foils however were not compatible with this adhesive and a special two component adhesive of Aliphatic amine and cyanoacrylic for plastics was used (Loctite SuperGlue-3 All Plastics). The frames are first glued on to the pre-strained SMP's and subsequently cut out. Every patch is glued in the same rectangular orientation on to the sheet and the four corners are numbered in the same way. This is necessary to keep the experiments consistent and to be able to read out the results easily. An example of an assembled patch is given in figure 2.4.

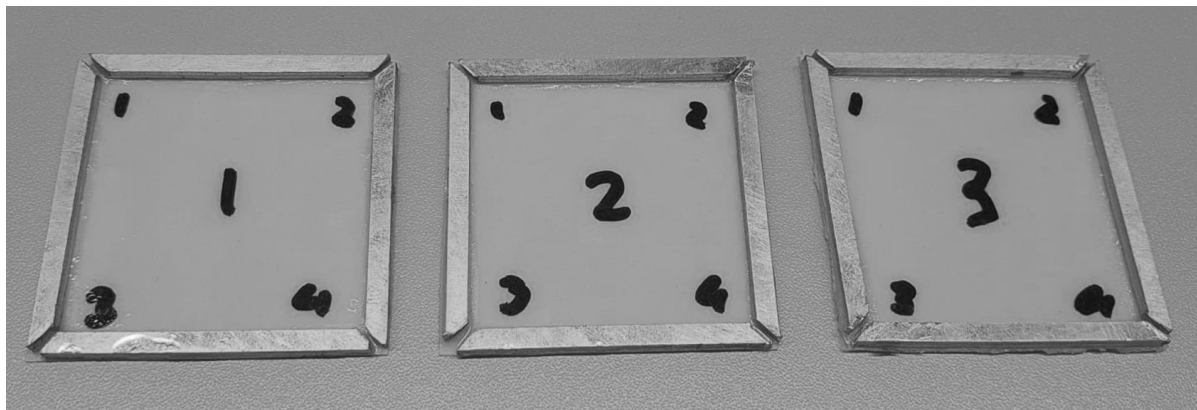


Figure 2.4: This figure shows an example of three patches after their assembly. In this example, an aluminium frame is used in combination with an isotropic SMP sheet. The number in the middle is used to label the different patches.

2.2. Patch groups

As earlier introduced, three different groups can be derived from the basic patch. With each group, different aspects (input parameters) of the concept can be tested. In this section each patch group will be introduced and their different input parameters will be described. A complete overview (test matrix) of the input parameters for every patch group is added in appendix B. A main distinction is made between the thicker SMP sheets in combination with the aluminium frame and the thinner SMP foils in combination with the 3D-printed Polycarbonate (PC) frame.

2.2.1. 3D-printed patch

For the 3D-printed PC patch all three types of foil are used. The activation method for this group is to submerge the patches in water. The focus of the printed patch is on testing different hinge designs. In addition, this patch is also used for testing the effect of different foil shrink types. Important to note is that apart from the changing parameters, everything else is kept constant (*ceteris paribus*). The test matrix for this patch group is added in appendix B.1.

Hinges

As previously shown, the four corners of the basic patch design are only restricted by the small area of SMP sheet between the adjacent beams. During activation the polymer is heated and becomes weak and due to its relatively big area, these corners without hinges will have a low stiffness. In order to see the effect of hinges and to be able to influence the way the patch folds, different hinges have to be added to the design. We have chosen to use simple compliant hinges of the same material as the rigid beams (PC). These hinges are relatively simple and easy to fabricate. An overview of the various hinge options considered has been added to appendix A. Three different compliant hinges were used in our design taking into account that they must be 3D-printed. The first hinge can only rotate over a single axis and therefore has one degree of freedom. This hinge and its so called axis of rotation are indicated in figure 2.5a. This hinge is called the 'slide hinge' as it can only slide in plane. The second hinge also rotates over a single axis and has one degree of freedom. This hinge's axis of rotation, however, is perpendicular compared to the 'slide hinge' and can therefore bend out of plane. This so called 'bend hinge' is shown in figure 2.5b. The third hinge can rotate in any direction possible and subsequently has three degrees of freedom. This hinge is called the 'rotation hinge' and is shown in figure 2.5c. By making simple derivations of the equation for the hinges based on the Euler-Bernoulli beam theory [7] [49], the bending stiffness of the hinges can be estimated. The equations are shown under their corresponding hinge in figure 2.5. For the 'bend hinge' and the 'slide hinge' the stiffness around the bending axis is calculated. For the 'rotation hinge' however the stiffness is taken as the average of the two main perpendicular bending axes.

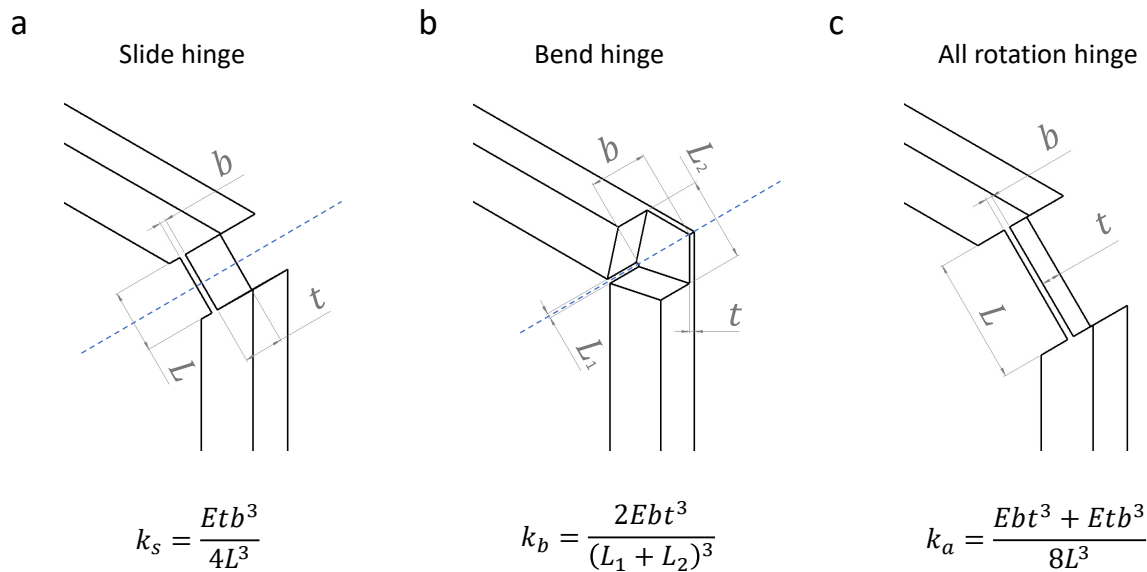


Figure 2.5: The three single-material hinges that were selected. a: The 'slide hinge' and its derived stiffness equation. b: The 'bend hinge' and its derived stiffness equation. In blue the bending axis of both hinge types is shown. c: The 'rotation hinge' and its derived stiffness equation.

Once the hinge types were defined, three different 3D-printed frame designs were made. In order to test the need for hinges, the first printed frame design has no hinges and is exactly the same as the basic patch design. The second printed frame design uses two types of hinges: the slide hinge and bend hinge. Important to note is that in this design, diagonally opposite hinges are always of the same type. With this design, different stiffnesses will be used for both the bend and slide hinge pairs. An overview of the chosen stiffnesses can be found in the test matrix for 3D-printed patches in appendix B.1. The combination of slide and bend hinges in a single frame was used, because a frame with only bend hinges or only slide hinges

would not fold properly. The last frame design has four all rotation type hinges with one stiffness. the three final frame designs are shown in figure 2.6. For testing all these specific frame designs, only the isotropic foil will be used.

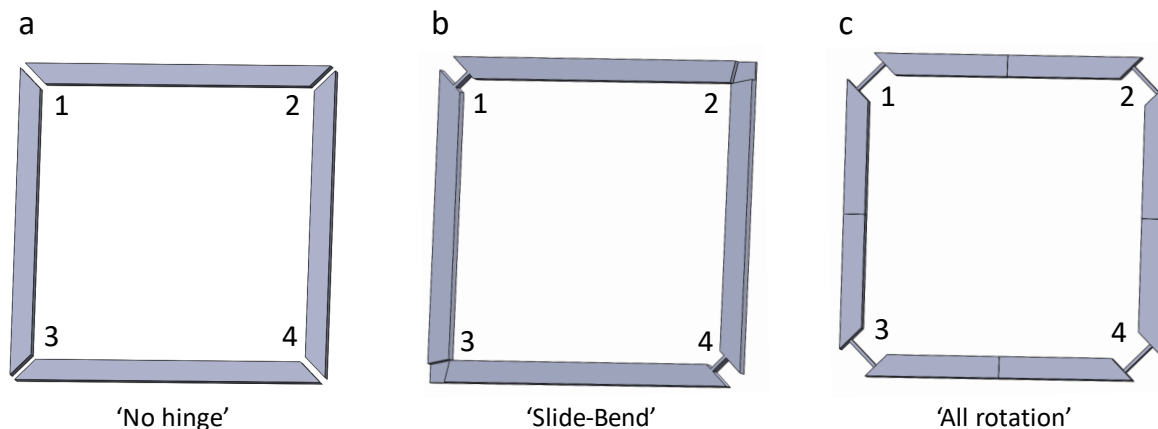


Figure 2.6: The three final frame designs with the different hinge types are shown. a: This design has no printed hinges and consists out of four separate beams (NH frame). b: Here the slide hinge and bend hinge are combined in one design. Important to note is that the opposite hinges are the same. Different stiffness for both hinges will be tested (S-B frame). c: This design has four all rotation hinges (AR frame). For all three patches only the isotropic foil will be used.

Foil type

As a next step, the different foil types will be tested. An isotropic shrink foil that uniformly shrinks the same extent in all directions, an uneven bidirectional shrink foil that shrinks in both directions but to a different extent and lastly an unidirectional foil that only shrinks in one direction. These foil types, also listed in table 2.1, were applied on two types of printed frames: the 'no hinge' design and the 'all rotation' design. These frame types were introduced earlier in figure 2.6.

2.2.2. Aluminium discrete patch

The aluminium discrete patch uses an aluminium frame in combination with the thick isotropic sheet. No other SMP is used. In this patch group, the four rigid beams from the basic patch design are never connected. Here too each time a single parameter is adjusted from the basic design, while everything else is kept constant (*ceteris paribus*). An overview of the complete test matrix for the aluminium discrete patch is added in appendix B.3.

Orientation

Normally, the patches are always orientated in the same way before activation, as will be explained later in the experimental set-up. This is done to keep the tests as consistent as possible. Here however, this standard orientation is changed in order to find out what effect this orientation has on shape-shifting. Next to the normal orientation, a second orientation is chosen where the patch is turned around and where the frame is thus located above the sheet. As a third orientation, the patch is aligned under a corner of 45° , instead of perpendicular. The three different orientations are shown in figure 2.7.

Corner aspect ratio

The corner aspect ratio of the two opposite corners pairs is changed contrary to the basic patch design where all unfolded corners make an angle of 90° . Three different corners ratio's are chosen, namely $90^\circ/90^\circ$, $70^\circ/110^\circ$ and $45^\circ/135^\circ$. An example of how the corner ratio is calculated is shown in figure 2.8. Important to note is that diagonally opposite corners form a pair with the same angle in their unfolded configuration.

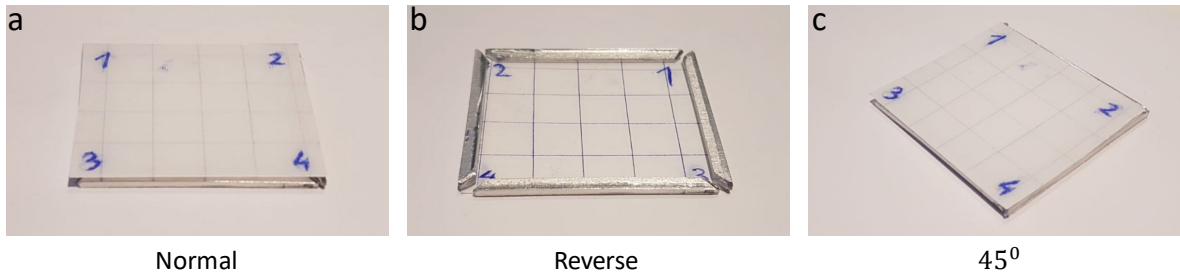


Figure 2.7: The three different patch orientations. a: This is the normal orientation used in all other experiments as explained in section 2.3. b: In the second orientation the patch is turned around before activation. c: Here the patch is aligned under a corner of 45°, instead of perpendicular.

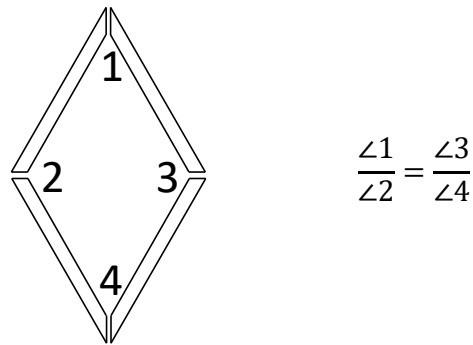


Figure 2.8: Example of the corner ratio. The angle of opposite corners are always equal. The corner ratio can be calculated by dividing the angle of one corner pair by the angle of the other opposite corner pair.

Temperature and time effects

In all other tests with of the aluminium discrete patches, the activation temperature is 170 °C and the activation time is 60 seconds. This will be further elaborated in section 2.3. Here both the activation time and activation temperature will be changed. By doing this, the robustness of the patch folding process, or in other words the activation process, can be qualified. The different activation temperature and activation times are summarized in table 2.3. For the lower temperatures in general a longer activation time is chosen, whereas for higher temperatures this time is shorter.

Table 2.3: The different combinations of activation temperature and activation time used as input parameter.

Combination #	activation temperature (°C)	activation time (sec)	Combination #	activation temperature (°C)	activation time (sec)
1	130	120	5	170	60
2	150	60	6	170	120
3	150	120	7	190	30
4	170	30	8	190	60

Beam thickness

Normally the thickness of the beam is 2 mm as shown in the basic design of the patch. Here this thickness will be used as a parameter and changed. Next to the 'standard' 2 mm, a beam thickness of 0.1, 0.3, 0.5, 1 and 4 mm is chosen. This parameter can expose two different aspects of the patch folding. The first one is the effect of the weight of the beam, this weight is of course changed due to the different thicknesses. The second aspect is the effect of the bending stiffness of the beam, which can be estimated based on the Euler–Bernoulli beam theory. In order to do this, a simply supported beam with uniform load is chosen as approximation 2.1. In this equation for the bending stiffness (S_{beam}) E is the elastic modulus of the frame material, b the width of the beam, t the thickness of the beam and L the length of the beam.

$$S_{beam} = \frac{32Ebt^3}{5L^3} \quad (2.1)$$

Scaling

The last changing parameter for the aluminium discrete patch is scale. The complete basic patch design is scaled by a factor 0.44 and a factor 1.55. The thickness of the SMP however could not be scaled, because a thinner isotropic sheet was not available. This means that only the area of the SMP is scaled and not the volume. Next to this 'complete scaling' the patch is also scaled in a different way. Again the scaling factors of 0.44 and 1.55 are used, but now only the length of the beams and the area of the patch are scaled. The cross section of the beams remains equal to the basic patch design (2 mm x 3 mm).

2.2.3. Aluminium continuous patch

The aluminium continuous patch could be seen as a variation on the previous two patch groups and a variation on the basic patch design. Again an aluminium frame and the isotropic sheet SMP are used. However where the previous two patch groups were based on rigid beams with or without hinges, this design consists out of a 'continuous' square frame with the same dimensions as the basic patch. This means that all four beams form one frame that continues in the corners. For clarification, this continuous design is shown in figure 2.9. The width, length and thickness of the frame are used as input parameters. Important to notice is that the thickness is constant for each frame, but will be used as changing input parameter. The idea of this frame is that it will not act rigid, but will deform together with the SMP to its final shape. This also means that the complete patch can be seen as the active part. This in contrast to the basic patch design, where only the SMP will form a curved shape.

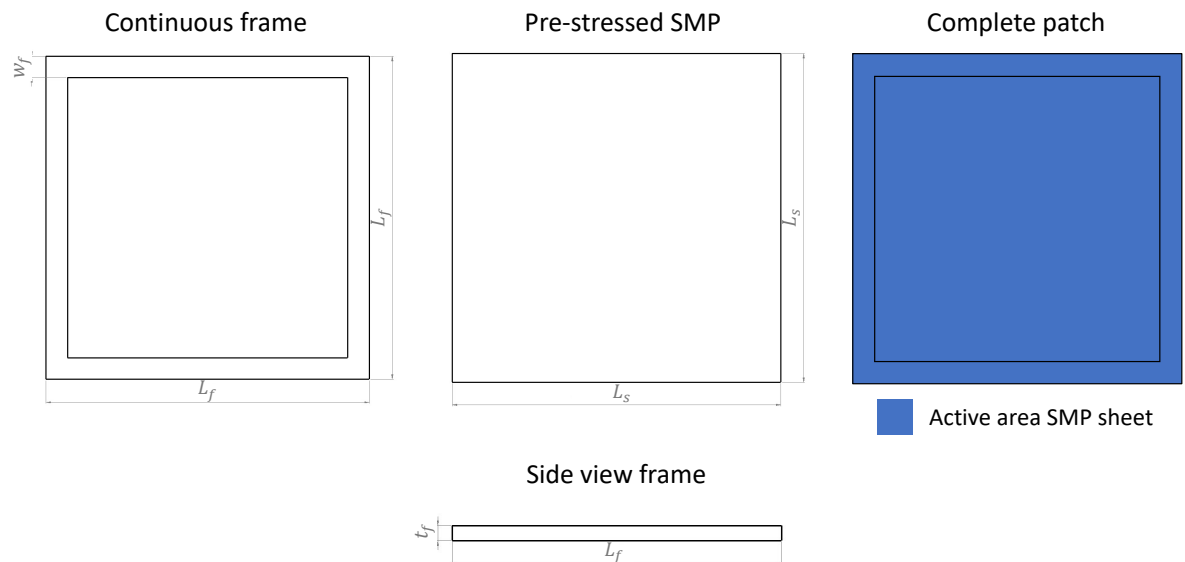


Figure 2.9: The design and dimensions of the continuous patch. On the top left the complete frame is shown. In the upper middle the pre-strained SMP sheet is shown. On the top right the assembled combination of the continuous frame and SMP sheet is shown. In blue the active area of the patch is marked. At the bottom a side view of the frame is given. Frame thickness (t_f), frame width (w_f) and Length L will all be used as input parameters. Note that the length of the frame (L_f) and the length of the sheet (L_s) are equal.

As previously explained, different combinations of the frame thickness, frame length and width will be used as input parameters. When activated, a trade-off is expected between the force the sheet can generate and the stiffness of the frame. In order to give a clear overview of this concept, the dimensionless parameter C_d is composed. Its equation consists out of the stiffness of the frame based on the Euler-Bernoulli beam theory divided by the elastic modulus and thickness of the sheet. In this equation t_f, w_f and E_f are respectively the thickness, width and elastic modulus of the sheet. t_s and E_s are the thickness and elastic modulus of the SMP sheet and L is the length of the frame and sheet. In this research both elastic moduli and the thickness for the sheet are constants, as the same SMP is used for all continuous patches and all frames are made from aluminium. For this sheet a thickness of 0.2 mm was taken and the elastic modulus of the sheet was based on the research of Mailen et al [39] [40]. An overview of all different input combinations and their corresponding C_d is shown in table 2.4. This table is also added to Appendix B.2.

$$C_d = \frac{E_f b_f t_f^3}{E_s t_s L^3} \quad (2.2)$$

Table 2.4: An overview of all different input parameter combinations for the continuous aluminium patch and their corresponding C_d . C_d is based on equation 2.2

Combination #	Length (mm)	Thickness frame (mm)	Width frame (mm)	C_d
1	45	0.5	3	$7.95 \cdot 10^{-4}$
2	60	0.5	4	$4.48 \cdot 10^{-4}$
3	80	0.5	5	$2.36 \cdot 10^{-4}$
4	100	0.5	6	$1.45 \cdot 10^{-4}$
5	45	0.1	3	$6.37 \cdot 10^{-6}$

2.3. Experimental set up

For our research, three different experimental set-ups were needed. One set-up for the printed patches, one for both aluminium patch groups and one for the verification of the different pre-strained SMP's. In this section, every experimental set-up and the different steps taken during the experiments will be introduced. The verification of the pre-strained material has not been previously introduced, but will be explained in this section and is done to check how the four different SMP's behave without a frame. Important to note is that for every test i.e. for every set of different parameters, three samples were created. In other words, every test consists out of three identical patches.

2.3.1. 3D-printed group

As previously explained, the printed patches with their corresponding foils are activated by hot water. For this experiment a large bowl, a gripper and a normal kettle is used. The bowl has to be relatively large in order to influence the activation process as little as possible. The experiment can be broken down into the following three steps.

1. The patch is placed in the middle of the bowl in such a way that the frame is on the downside and the foil on the upside.
2. Boiling water is poured into the bowl in a calm but smooth motion until the water level has a height of 70 mm. The patch has to stay submerged in the water for 60 seconds, while the activation process takes place.
3. Subsequently, the patch is carefully removed from the water with a pair of pliers and laid on a flat and dry surface. After the activation process, the patch is cooled in the open air for two minutes.

2.3.2. Both aluminium groups

The aluminium patch groups, both the discrete and the continuous patches, are activated in an oven by hot air. The activation process for the aluminium discrete patch group and aluminium continuous patch group is the same. For this experiment, a Nabertherm air circulation chamber oven and thin and flat aluminium bowl are used. Here too the experiment can be broken down into the three steps shown below. Important to note is that in the given example the standard perpendicular orientation, an activation temperature of 170 °C and an activation time of 60 seconds are used. This is the case for most of the patches, unless these values are changed as an input parameter as explained earlier.

1. The oven is pre-heated to 170 °C, when it reaches the desired temperature the aluminium bowl is placed in the oven. This aluminium bowl also has to be pre-heated for 3 minutes before the next step.
2. The patch is placed in the middle of the bowl in a perpendicular orientation (aligned with the oven walls) and with the frame on the downside and the isotropic sheet on the upside. The oven is closed and the patch is heated for 60 seconds during which the activation process takes place.
3. The complete aluminium bowl with the patch on top is taken out of the oven and is cooled in the open air for two minutes. When starting a new activation process, the aluminium bowl has to be pre-heated again for 3 minutes.

2.3.3. Pre-strained SMP verification

In order to know how the four different SMP's will behave when they are activated and not connected to a frame, an SMP verification experiment is done. In this experiment, the different materials are cut into

square sheet samples of 45 mm x 45 mm and are activated. Afterwards, the length of the horizontal and vertical direction can be measured and the amount of shrinkage can be determined. The activation is done at different temperatures starting from 30 °C until 210 °C with intermediate steps of 20 °C. The experiment is done in a Nabertherm air circulation chamber oven for all four SMP's. The experiment can be broken down in the following five steps.

1. In the oven an aluminium framework with a height of 0.5 mm is placed. This is done in order to prevent the SMP sample from coiling and bending during activation. This framework is shown in figure 2.10a.
2. The pre-strained material is cut in a square sample of 45 mm x 45 mm, an example is shown in figure 2.10b.
3. The oven with the framework is pre-heated to the desired temperature, for every SMP multiple temperatures are tested as previously explained.
4. The square sample is placed under the framework and the oven is closed. The sample will be heated for 60 seconds.
5. The sample is taken out of the oven with a gripper and cooled in the open air on a flat surface for two minutes. After finishing the activation process, the length of the vertical and horizontal directions can be measured with the help of a caliper.

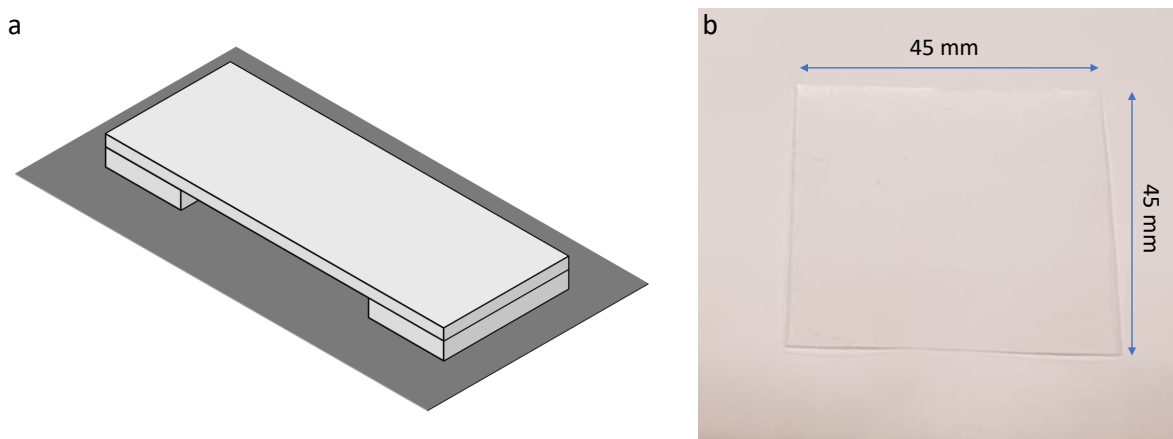


Figure 2.10: a: Drawing of the aluminium framework used in the SMP verification experiment. This framework prevents the SMP samples from coiling and bending during the activation process. b: An example of a square 45 mm x 45 mm sample cut out of a pre-strained SMP.

2.4. Data generation and Measurement

After the patch activation, the effects of different parameters need to be measured. There is however no protocol or previous research done that shows how to measure and quantify different important aspects of curved shape-shifted patches. This is why all chosen 'output parameters' and the process of data measurement and generation will be explained in this section. In figure 2.11 an overview of the complete process is given. This process is divided and explained in 5 different subsections. At the outset, it was not known whether every output parameter would actually contain useful information as this kind of data measurement was not performed before. The data generation process is equal for every patch group.

2.4.1. Basic measurements

These are the measurements that can be done without the interference of a computer and are relatively simple. The first one is the folded corner angle, where the corner angle between the adjacent beams is measured after activation as shown in figure 2.12a. This is done for all four corners of the patch. Every corner of every patch is numbered in the same way in order to keep the measurements consistent. The other two measurements are qualitative. First, the patch is analysed with the naked eye and by observing its rigidity. Next to that, a grid analysis is done. Before activation, a 10 mm x 10 mm grid is drawn on the SMP as shown in figure 2.12b. After activation, the shrinking behaviour (strain) of the SMP is mapped on the basis of this grid.

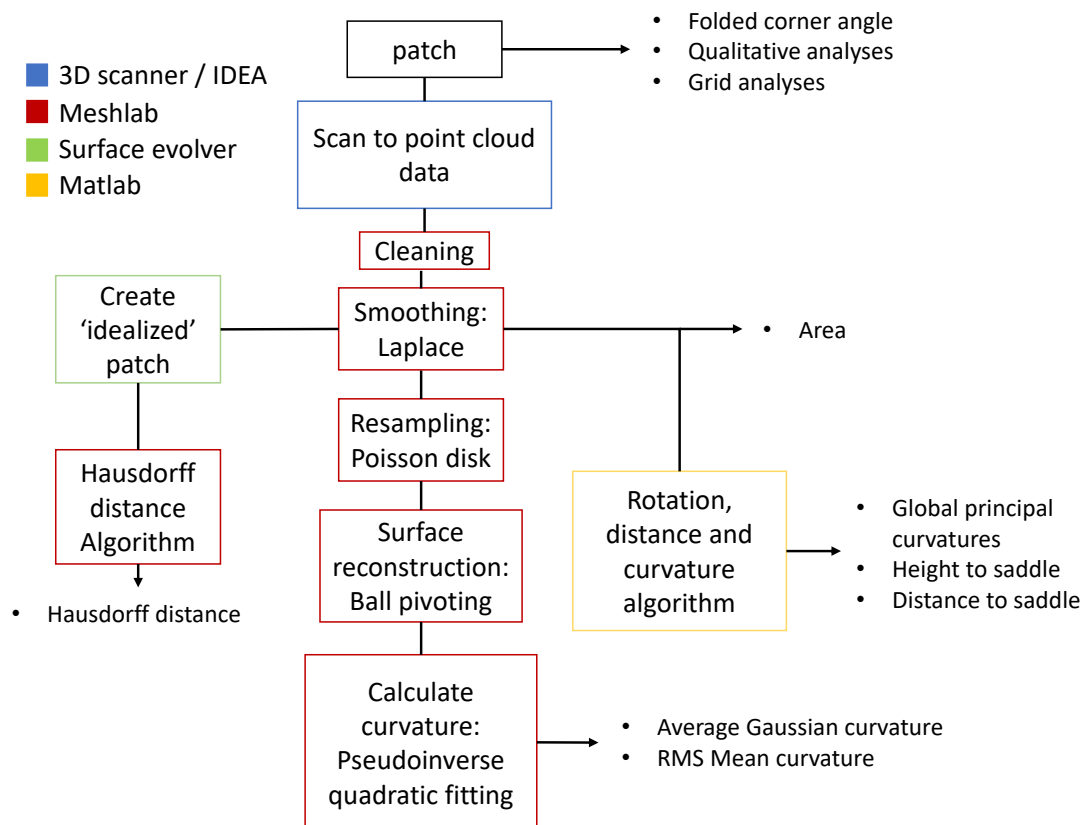


Figure 2.11: Overview of the complete data generation and measurement process.

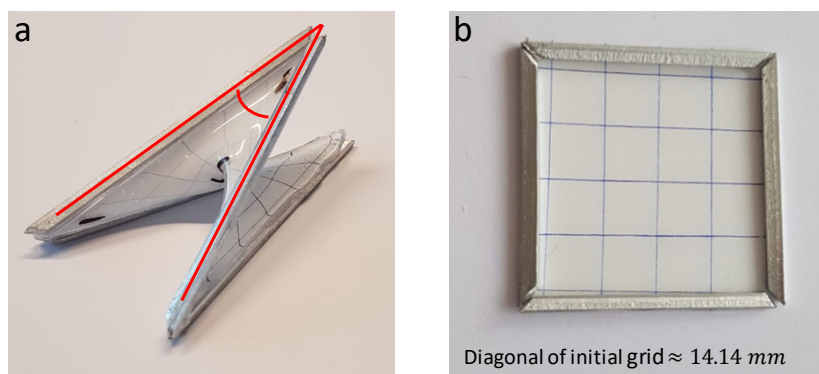


Figure 2.12: a: Example of measured folded corner angle of one corner of a patch after activation. b: 10 mm x 10 mm grid for grid analysis drawn on the SMP.

2.4.2. Scanning and cleaning

The surface of the patch is scanned with a 3D scanner (SCAN in a BOX) and is then converted to a point cloud with the help of the corresponding software program Idea. Because the SMP of many patches is transparent, which inhibits the scanning process, the folded patches are sprayed with metal paint before scanning. Afterwards the point cloud is meshed in Idea and can be uploaded into Meshlab. This program is a mesh processing and editing tool with various capabilities [13]. Irregularities on the edges of the scanned patch can be removed as it is important that only the active area of the patch is used in further calculations. Afterwards the patch is smoothed with a simple laplacian smoothing function. This function calculates the average position of the vertex based on surrounding vertices [26]. This is done in order to smooth out small disturbances due to the scanning process. Afterwards the area of the scanned patch can be calculated. The process of scanning and cleaning/smoothing is shown in figure 2.15.

2.4.3. Rotation, distance and global principal curvatures algorithm

The cleaned and smoothed point cloud can be exported and uploaded into Matlab. Here an algorithm is written that rotates the point cloud into an upright position in order to perform its calculations correctly. Subsequently, the saddle point of the point cloud is calculated by selecting the point which is lowest in direction of the upper opposite corner pair and highest in direction of the lower opposite corner pair. When this saddle point is calculated, the algorithm calculates the length from this saddle to the corners of the patch. This is done both in the horizontal projected plane and the vertical projected plane, called distance to saddle and height to saddle. In order to get an overview on how the patch is curved on a large scale and to know how the patch is folded into different directions, a 8 mm radius circular area of the patch is selected. This radius can be seen as the neighbourhood over which the local curvature is calculated. The middle point of the circular surface is the saddle point. Through this surface, the two principal curvatures (K_1 and K_2) can be calculated. From now on these two principal curvatures will be called the global principal curvatures of the patch in order to avoid confusion with other output parameters introduced later. The term global is chosen as the principal curvature are calculated over a relatively large area (radius of 8 mm). An example of every step of the Matlab algorithm is shown in figure 2.13.

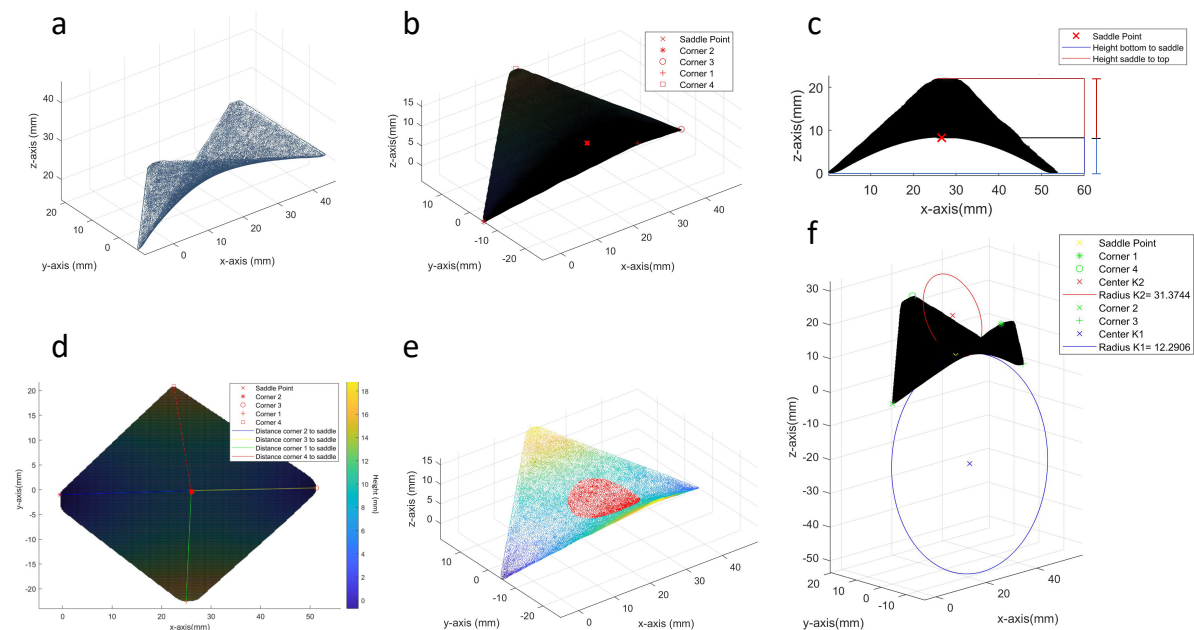


Figure 2.13: Example of the patch processing steps in Matlab. a: Shows the initial point cloud imported from Meshlab. b: The patch is rotated into an upright position and the saddle point of the patch is calculated. c: The height of the saddle point to the corners in the vertical projected plane is calculated. d: The distance of the saddle point to the corners in the 2D horizontal plan is calculated. e: The 8 mm radius circle with the saddle as middle point is shown in red. f: The two global principal curvatures plotted through this circular surface are shown.

2.4.4. Surface evolver and Hausdorff distance

Surface evolver is a software for modelling the influence of various forces and constraints on the shape of (liquid) surfaces. In this research, the software is used to numerically minimize the surface energy of a surface between given constraints [5]. As explained earlier in section 1.5, a surface with minimized area, and therefore minimized surface energy, is called a minimal surface. By entering the outer border of the scanned patch as a constraint in surface evolver, the minimal surface between this outer border can be calculated. An example of such a calculated minimal surface is shown in figure 2.14a. This 'ideal surface' can be exported back to Meshlab, where it can be placed over the original scanned patch. By doing this, the difference between the 'idealized' patch and the real patch can be compared. This can be seen as a measure of how close the real patch approaches a minimal surface. This difference was calculated by the Hausdorff distance filter in Meshlab [12]. In this algorithm, the surface is sampled and the closest point over to the other surface is found for every point [2]. An example of the Hausdorff distance between the 'idealized' and real patch is shown in figure 2.14b.

2.4.5. Scan correction and curvature calculations

In Meshlab the mean and Gaussian curvature can be calculated for every vertex of the meshed surface with the pseudoinverse quadratic fitting algorithm. The mesh used is created between all the points of the initial scanned point cloud. Because the pseudoinverse quadratic fitting algorithm uses the surrounding vertices in order to calculate the local curvature of each point, the distance between these vertices should be approximately equal. This is necessary in order to consistently calculate the curvature of each point and to be able to compare the curvature of different patches. In the initially scanned point cloud, the distance between these points is not equal and the distribution is not uniform. This is why the initial patch is re-sampled according to the Poisson-disk distribution with an explicit radius of 0.3 mm. By doing this, a uniform distributed point cloud is created with a nearly constant distance of 0.3 mm between the points [15]. Subsequently, the surface is reconstructed (remeshed) with the ball pivoting algorithm available in Meshlab [33]. Now the mean and Gaussian curvature for every vertex of every patch can be calculated in a consistent manner with the pseudoinverse quadratic fitting algorithm. In order to do this first the principal curvatures of every vertex are calculated, the difference with the previously introduced global principal curvatures, is that the neighborhood used in this calculation is significantly smaller (0.3 mm). The resampling and reconstruction of the patch's mesh is shown in figure 2.15. The curvature information of each vertex can be used to calculate two important measures namely the average Gaussian curvature and the root mean square of the mean curvature. The average Gaussian curvature is calculated by taking the average of the Gaussian curvature of every vertex and can be seen as a measure for how much the patch is intrinsically curved. The root mean square of the mean curvature is a measure for how much the mean curvature differs from zero. As a minimal surface has zero mean curvature, this can again be seen as a measure for how close the patch's surface approaches an ideal minimal surface. Both values are made dimensionless in order to make it possible to compare the values for patches of different sizes. This is done by multiplying the RMS mean curvature with the length of the patch (L) and the average Gaussian curvature with L^2 . These calculations are done in matlab, both formulas are shown below (2.3 and 2.4). k_n is the Gaussian curvature for each vertex and h_n the mean curvature for each vertex.

$$K_{avg} = \frac{L^2}{n} (k_1 + k_2 + \dots + k_n) \quad (2.3)$$

$$H_{RMS} = L \sqrt{\frac{1}{n} (h_1^2 + h_2^2 + \dots + h_n^2)} \quad (2.4)$$

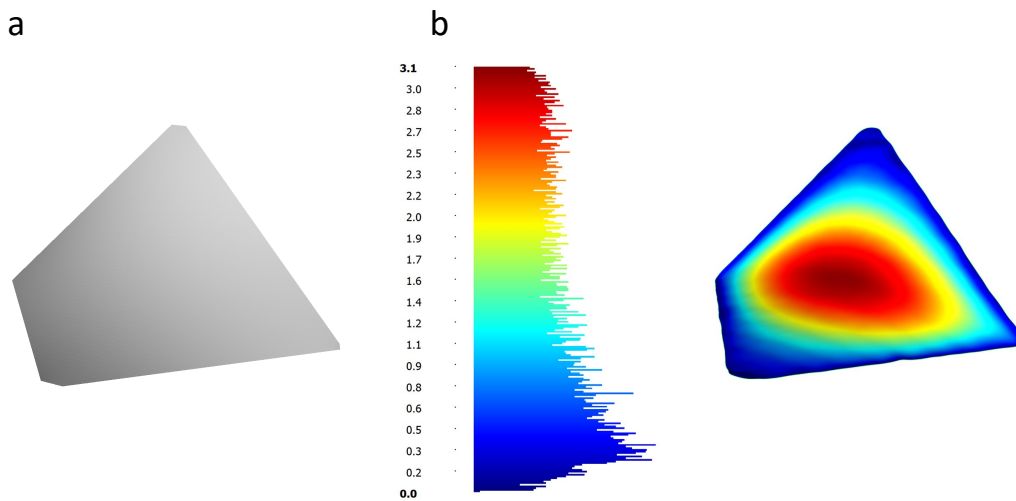


Figure 2.14: a: Example of a minimal surface created by surface evolver, spanned between the outer boundaries of the real patch. b: The Hausdorff distance between the 'idealized calculated patch' and the real patch. This distance is projected on to the real patch.

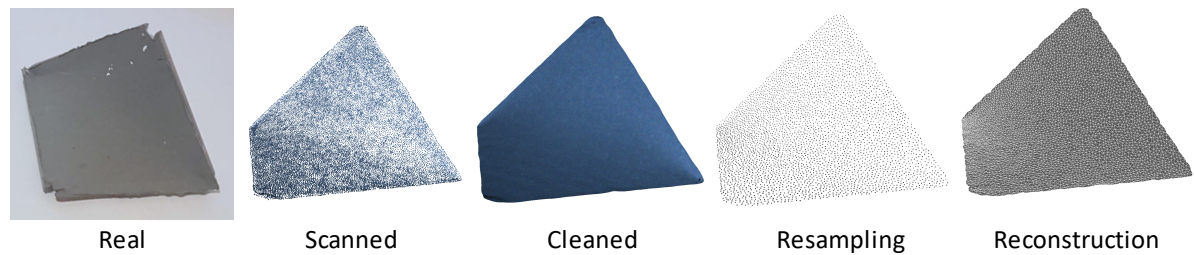


Figure 2.15: The complete scanning and mesh processing steps. First the surface of the patch is scanned and converted into a point cloud. Afterwards, the patch is cleaned and smoothed with the laplacian smoothing algorithm. In order to fairly calculate the curvature of the surface, the patch is resampled into an uniform point cloud. subsequently the surface of the patch needs to be reconstructed.

2.4.6. Statistical significance

In order to assess if there are statistically significant differences between the shape-shifted patches, unpaired two-sided t-test's will be performed between the measured output parameters of different patch types. This t-test is used as the measured output is independent for every patch. Next to that, it is assumed that the measured parameters of each patch have a normal distribution and that the values will have the same standard deviation. Two significance levels were chosen: 0.05 and 0.01.

2.5. FEM model

In order to predict and further explore the behaviour of the patches, a finite element model was constructed. The finite element analysis software Abaqus version 2017 was used [50]. This model tries to simulate the real aluminium discrete patch, originally based on the research of Cui et al [16]. The frame is based on aluminium and the SMP on the isotropic sheet material.

2.5.1. Design and assembly

For the design of the FEM model, a simplified version of the basic patch introduced in figure 2.2 is used. The four rigid beams are modelled as four separate deformable wire parts and the SMP sheet is modelled as a deformable shell part. The cross section of the beams is set at 3 mm x 2 mm similar to the basic patch design. The area of the modelled SMP sheet is taken at 39 mm x 39 mm. This is the same area as the active part of the SMP in the basic patch design. The thickness of the sheet material is set on 2 mm, this is similar to the thickness of a completely shrunken isotropic sheet. In this simplified model, the beams also have a length of 39 mm, again similar to the inner/active length of the basic patch. Here the beams are not cut in a 45° angle at both ends, but have two perpendicular endings. When the model is 'activated', the SMP shows excessive non-linear behaviour in the corners. In order to prevent the model from diverging, a small triangular area has been left out in all four corners of the SMP sheet. The final simplified FEM design of the aluminium discrete patch is shown in figure 2.16. The beams are connected to each other in the corners with a kinematic coupling constraint. This constraint inhibits translation, but allows rotation in all directions. Subsequently, the four modelled beams are connected to the SMP sheet with a tie constraint.

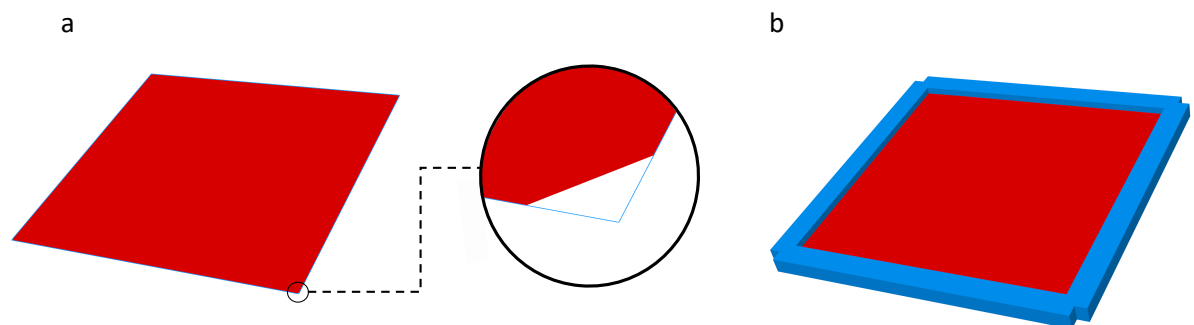


Figure 2.16: The simplified FEM design of the aluminium discrete patch. a: The SMP sheet (red) and beams (blue) are shown as shell and wire parts and a close-up of the corner design is given. b: The SMP sheet (red) and beams (blue) with their modelled dimension.

2.5.2. Material properties

Most material properties for the SMP sheet are based on the previous research of Mailen et al. and are shown in table 2.5 [39], including the prony series coefficients in order to model viscoelastic behaviour. The linear thermal expansion however is based on our own findings. In the SMP verification experiment, it is found that an unrestricted isotropic sheet shrinks approximately 45 % in length. In this model the patch is heated from 20 °C to 170 °C. This means that the total temperature difference during activation is 150 °C. assuming that the SMP shrinks linearly the same amount for every degree, the sheet will shrink approximately by a factor of 0.0054 per °C (2.5). For the aluminium frame an elastic modulus of 150 *Gpa* is defined, which is more than twice the real E modulus of aluminium. This is done in order to make sure that the four beams will act as rigid parts and will not bend. When the real elastic modulus of aluminium was used in the model, the frame showed an unrealistically large deformation. The Poisson ratio of aluminium is based on literature [14]. It is assumed that temperature will not have any effect on the beams. This is why other material properties were not implemented int the model for the aluminium.

$$(1 - 0.0054)^{150} \approx 0.45 \quad (2.5)$$

Table 2.5: In the left table the material properties for the SMP material and frame material in the finite element model are shown. In the right table the prony series coefficients for the SMP material are shown in order to model viscoelastic behaviour. All values are based on the research of Russel et al. except the values with an *, which are based on own research and assumptions [40] [39].

	SMP material	Frame material		g_i	$t_i(s)$
Young's modulus (<i>Pa</i>)	$1.78 \cdot 10^9$	$150 \cdot 10^9^*$	1	0.2089	1.182
Poisson's ratio	0.33	0.33*	2	0.3654	14.77
Conductivity (<i>W/mK</i>)	0.14	-	3	0.3037	114.8
Density (<i>kg/m³</i>)	1050	-	4	0.1011	402
Linear thermal expansion (<i>K⁻¹</i>)	-0.0054*	-	5	0.01243	3096
Specific heat (<i>J/kgK</i>)	1300	-	6	0.004661	25680

2.5.3. Mesh

For the modelled SMP sheet material a 2D quad-dominated thermally coupled mesh was used with an approximate global size of 0.7 mm. This was done in order to model the part as a shell and to make it possible to model temperature and displacement effects. For the beams, a conventional 2D linear beam mesh was used as the beams are modelled as wires and will not be affected by temperature differences in the model. The approximate global size of the beam mesh was set at 0.175 mm, which means there is a 1/4x difference between the SMP mesh size and beam mesh size. The complete meshed assembly consists out of 6712 nodes and 6553 elements. In order to test the converge of the model, the model will be also run with different numbers of nodes. The lowest amount of nodes is 400 and the highest 17940 with eight intermediate steps. The total strain energy will be monitored in order to test this convergence. The max von Mises will also be taken in to account, to make sure no irregular high stress peaks occur in the model. A maximum difference of 5% , between two consecutive steps, is chosen as the convergence boundary for both values. Important to note is that the 1/4 difference between the SMP mesh size and the beam mesh size, stays constant for every number of nodes.

2.5.4. Activation

The activation of the patch is modelled by three consecutive non-linear coupled temp-displacement steps. These different steps are visualized in figure 2.17. Important to notice is that the starting temperature of the model is pre-defined at 20 °C.

1. In the first step a small perturbation is applied to the patch. This is done to initiate out-of-plane folding. The perturbation is applied by fixing one opposite corner pair, while moving the other opposite corner pair up with a small distance of 7 mm. The step time is set at 6 seconds.
2. In the following step the boundary conditions from the first step are propagated and the patch is heated with an uniform surface radiation of 100 °C for a short time period of 5 seconds. This causes the SMP to shrink to a small extent and ensures that the patch will not fold back when the boundary conditions are removed.

3. In this step both boundary conditions are removed and the patch is heated with a uniform surface radiation of 170 °C for a time period of 200 seconds.

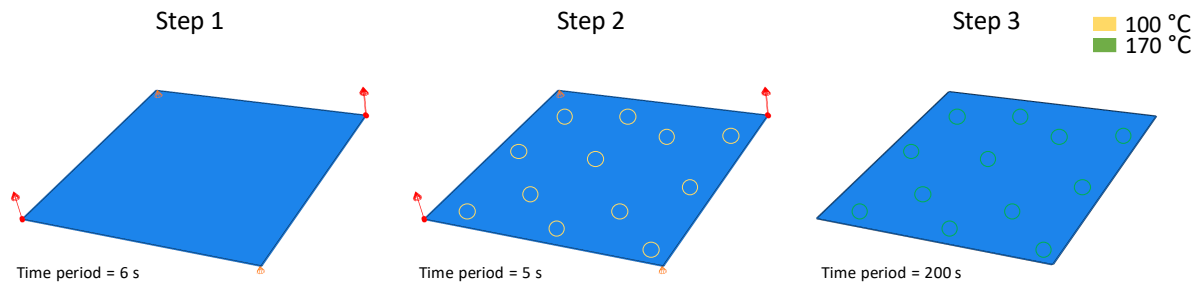


Figure 2.17: The three consecutive steps used to model the activation process. step 1: A small perturbation is applied to the patch. This is done by fixing one opposite corner pair (orange), while moving the other corner pair up with a small distance (red). step 2: The boundary conditions of the first step are propagated and the patch is heated with a uniform surface radiation of 100 °C for a short time period of 5 seconds. step 3: The boundary conditions are removed and the patch is heated with a uniform surface radiation of 170 °C for a time period of 200 seconds.

2.6. Abbreviations & Acronyms

To provide clarity to the reader a list of most important abbreviations and acronyms, of earlier explained terms and concepts, is introduced. These abbreviations will be used in the remainder of the report.

Al continuous patch	Aluminium continuous patch
Al discrete patch	Aluminium discrete patch
AR frame	All rotation frame
C_d	Dimensionless parameter to define aluminium continuous patch
FEM model	Finite element method model
H_{RMS}	Dimensionless Root Mean Square of the mean curvature
K_{avg}	Dimensionless average Gaussian curvature
NH frame	No hinge frame
PC	Polycarbonate
S_{beam}	Bending stiffness of the beams of aluminium discrete patch
S-B frame	Slide-Bend frame
SMP	Pre-stressed Shape-Memory Polymer
TPMS	Triply periodic minimal surfaces

3

Results

In this section, first the results of the experiments qualifying the different unrestricted SMP's will be discussed. Next, the shape-shifting of the printed patches is discussed and the effects of their corresponding input parameters. Subsequently, the same is done for the shape-shifting experiments with the AL discrete patches and the AL continuous patches. Lastly, The stress and strain analysis and the convergence of the FEM model is introduced and the model is compared to the real experiments and to its corresponding 'idealized' surface.

3.1. Shape memory polymer behaviour

The shrink percentage for every chosen SMP was measured for different activation temperatures starting from 30 °C until 210 °C with intermediate steps of 20 °C and is shown in figure 3.1a. The foil SMP's started to melt above a threshold temperature, which is the reason why there is no data measured for the foils at higher temperatures. It is clearly demonstrated that most materials do not shrink until a certain temperature and subsequently completely shrink in one temperature step. The isotropic foil is an exception and keeps shrinking with increasing temperatures. Interestingly, this foil shrinks isotropically until a certain temperature (110 °C), after which a difference between the shrink percentage of both the horizontal and vertical direction is visible (figure 3.1b). In the other experiments, we selected the activation temperature of patches with this foil to be below 110 C, which is within the isotropic range and therefore this difference in shrink percentage does not occur. Figure 3.1c shows the shrink percentage of the SMP's at the chosen activation temperature, which is 100 °C for the foils and 170 °C for the sheet material. The isotropic materials shrink by almost the same extent in horizontal and vertical directions. The uneven bidirectional foil, however, shrinks to a different extent in both directions. The uniform foil only shrinks in one direction, while in the other direction it even extends with a small percentage. There is also a difference in the shrink percentage of the area. The foils typically shrink less compared to the isotropic sheet($\approx 80\%$). The isotropic foils shrinks the least with a percentage of approximately 29 %.

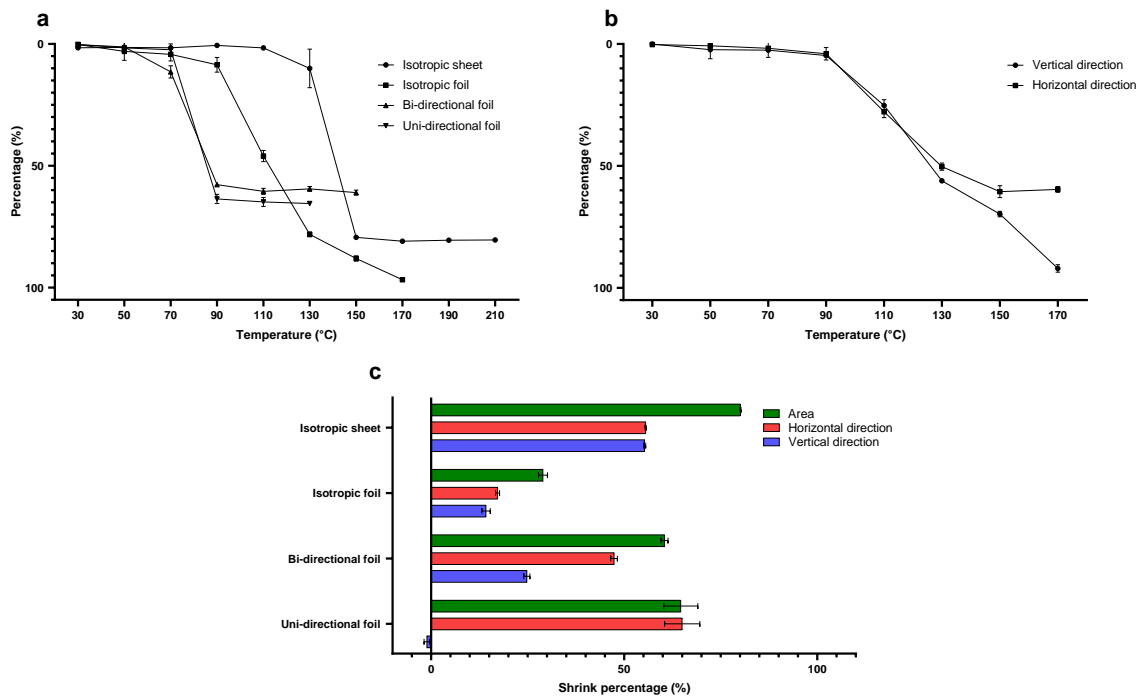


Figure 3.1: a: Area shrink percentage of different SMP's as a function of temperature. b: Shrink percentage of horizontal and vertical directions of Isotropic foil material as a function of temperature. c: Shrink percentage of different SMP's at their chosen activation temperature.

3.2. Behaviour of 3D-printed patches

Three patches of every printed patch type were fabricated and activated. In total 10 different patch types were created, which therefore results in a total of 30 printed patches. First, the effect of different hinge types on patches with isotropic foil will be presented. Subsequently, the effect of different foils on the printed patches will be shown.

3.2.1. Effect of hinge type

Even though all patches were fabricated using the same isotropic foil, clear differences could be observed between the saddles formed with different frame types. The frame that consists out of four separate beams without hinges (NH frame), does not form a saddle. This frame forms an irregular, collapsed shape with little stiffness as shown in figure 3.2a. Therefore it was not possible to further analyse this patch. The other two frame types both form a clear saddle, although the AR frame shows irregular wrinkles on the surface as shown in 3.2b. The different stiffness variations of the S-B frame, clearly show that the stiffness of the bend hinge is a dominant factor in determining saddle formation. If the bend hinge stiffness is lower, the frame folds more. The stiffness of the slide hinge has a similar effect, but to a much lesser extent as shown in figure 3.2c.

In case of the AR frame, figure 3.3a shows that both opposite corner pairs bend to the same extent. There is a significant difference, however, between the opposite corner pairs of the S-B frames, if the bend corner pair has a lower stiffness. For a higher stiffness of the bend pair, there is no significant difference between the folded corner pairs and the patch almost does not fold as shown in figure 3.2c. The bending corner pair is clearly dominant since changing the stiffness of the slide corner has a smaller effect. These corner angle measurements confirm the observations introduced previously. Investigating the angle of the folded corners separately as shown in figure 3.3b, it is clearly visible that opposite corners always fold similarly and show no significant difference. This indicates that the average angle of a folded corner pair is a good representation of opposite corners.

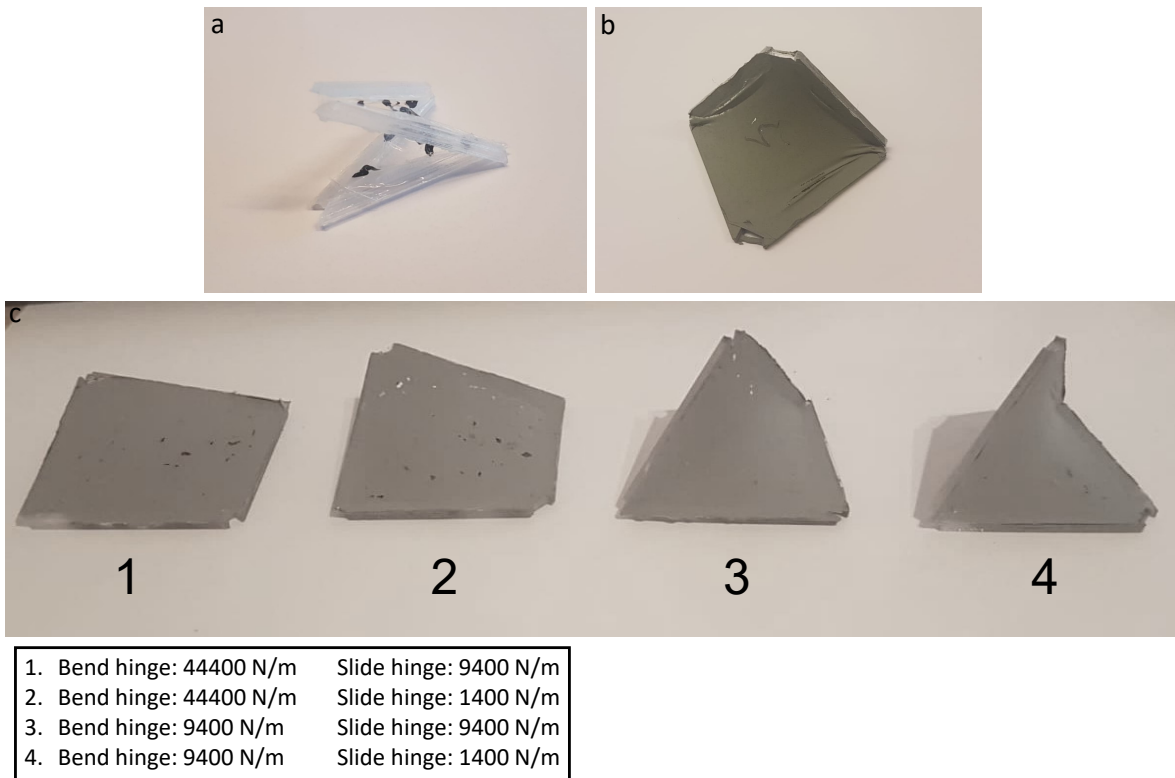


Figure 3.2: The folded printed patches with different frames(hinge types), all with isotropic foil. a: Folded patch with four separate rigid beams (NH frame). b: Folded patch with AR frame, note the wrinkles on the sheet. c: Folded patch with S-B frame, four different variations of hinge stiffness are shown.

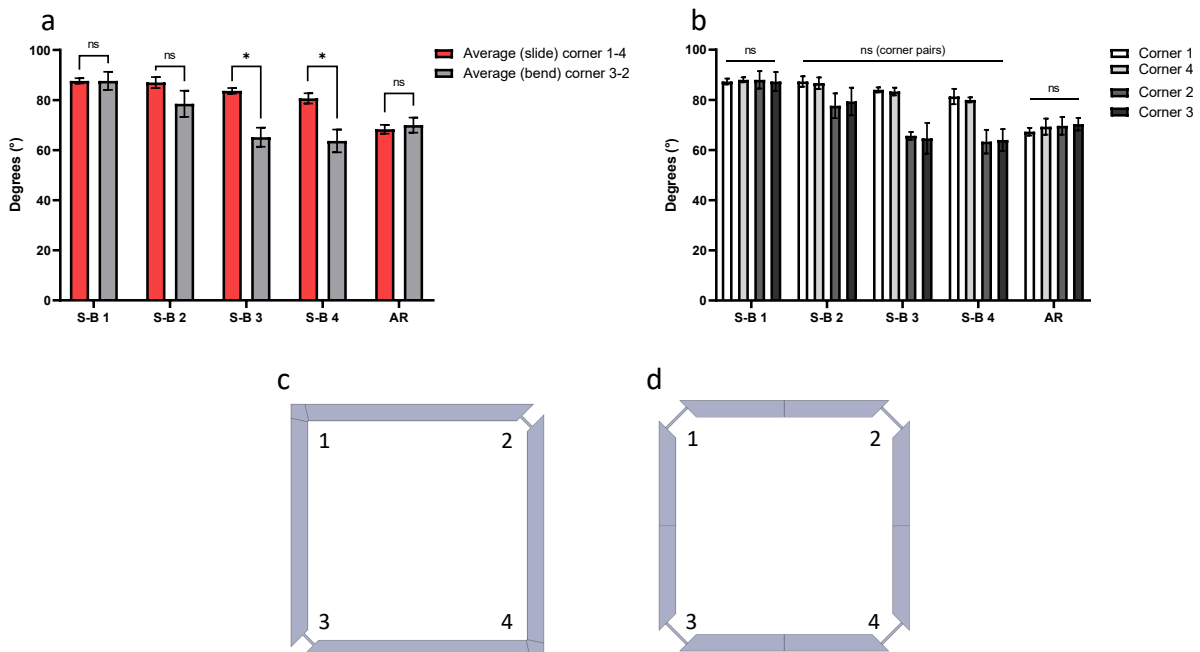


Figure 3.3: a: The average folded corner angle for opposite corner pairs for different printed frame types. S-B frames are numbered based on figure 3.2c. b: The folded corner angle of each corner for different printed frame types. c: Example of S-B frame with numbered corners. Corner 1 and 4 form the opposite (slide) corner pair and corner 2 and 3 form the opposite (bend) corner pair. d: Example of AR frame with numbered corners. Corner 1 and 4 form an opposite corner pair as do corner 2 and 3. *p < 0.01.

Figure 3.4 shows the calculated mean and Gaussian curvature for the different frame types. The mean curvature of the AR patch is relatively close to zero and therefore predominantly green in the figure. Large disturbances can, however, be seen on the sides due to the wrinkled surface. The Gaussian curvature is predominantly negative for the 'all rotation' patch. This indicates that the 'all rotation' patch clearly forms a saddle (negative Gaussian). The S-B patches are closer to a zero mean curvature compared to the 'all rotation' patch. Also there is less disturbance and a clear peak is shown around zero in the histogram of the patches. The further the patches fold due to the lower stiffness of the hinges, the more the mean curvature deviates from zero mean curvature. It is noteworthy that the first S-B patches fold to a very small extent, which means that they are close to a flat surface (which has zero mean curvature). So although the mean curvature is close to zero and therefore close to a minimal surface, this is not meaningful as the patch is almost not folded. The Gaussian curvature substantiates this. As the Gaussian curvature becomes more negative (red in the figure), the patch is folded more. This means that the patch becomes more hyperbolic. This clearly shows a trade-off between mean and Gaussian curvature, when the patches are folded. For a Gaussian curvature that is more negative, the mean curvature deviates more from zero.

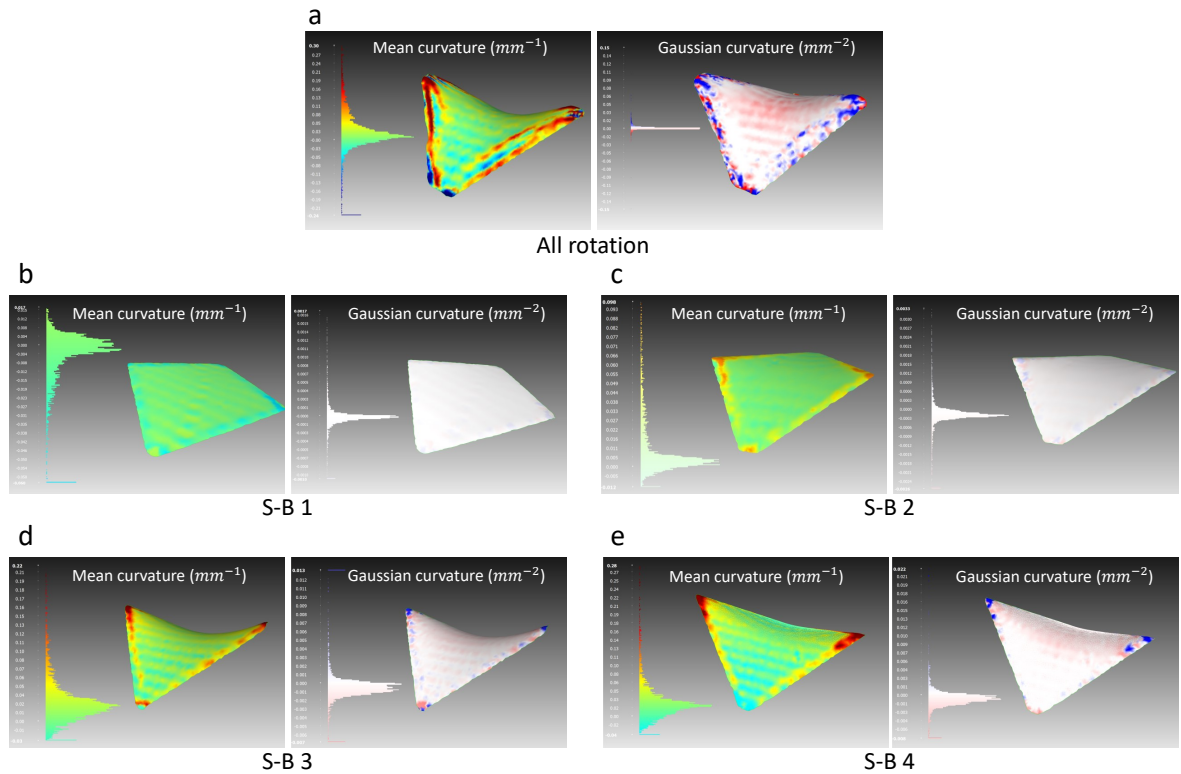


Figure 3.4: The mean curvature(mm^{-1}) and Gaussian curvature(mm^{-2}) for the different frame types of the printed patches, all with isotropic foil. The mean curvature is shown on the left in RGB colours and the Gaussian curvature on the right in RWB colours.

This trade-off is also visible in the different curvature measurements. The H_{RMS} rises, when the patch is folded more, while the K_{avg} becomes more negative as shown in figure 3.5a. Interestingly the 'all rotation' patch shows a higher H_{RMS} , but an K_{avg} that is less negative compared to the S-B patches. Although the pictures clearly show that the 'all rotation' patch is folded further. This could be due to the irregularities on the surface as shown earlier. The two global principal curvatures also show an upward trend when folded more as shown in figures 3.5b and 3.5c. A significant difference occurs between k_1 and k_2 for the S-B patches with a lower bend hinge stiffness, which is probably due to the different hinge types used. The 'all rotation' patch also shows a difference between the two global principal curvatures, but this difference is smaller (figure 3.5d). Figure 3.5e shows the area of the different patches with different frames and is subsequently compared with the maximum shrink percentage of the isotropic foil. It is thus compared with how much the foil would shrink if it was not restrained by a frame. A downward trend in area is shown, when the patch is folded more. There is however a significant difference between the area of every patch and the maximum shrinkage of the isotropic foil. This shows that due to the frame, the shrinkage of the isotropic foil is opposed.

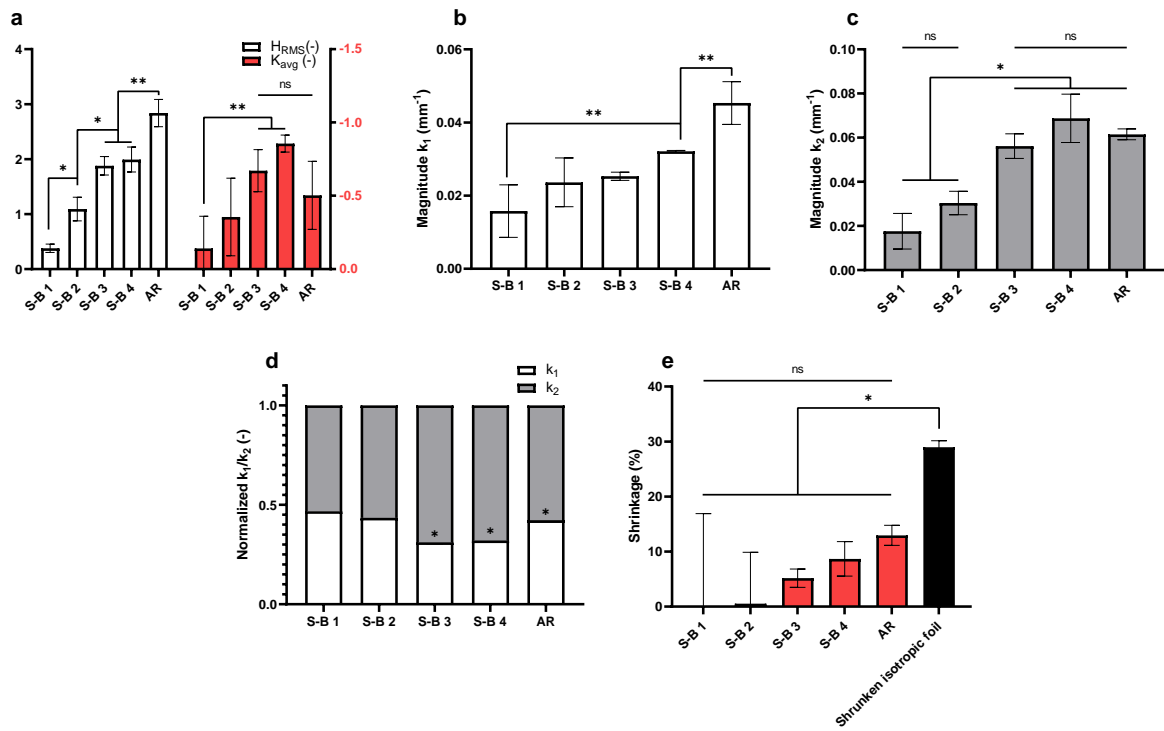


Figure 3.5: a: H_{RMS} and K_{avg} for different printed frame types. b: Global principal curvature k_1 for different printed frame types. c: Global principal curvature k_2 for different printed frame types. d: Normalized ratio between k_1 and k_2 for different printed frame types. e: Area shrink percentage of the SMP for different printed frames compared with area shrinkage of isotropic foil without constraints. ** $p < 0.05$, * $p < 0.01$.

Figure 3.6a shows that for all frame types that use the isotropic foil, the height of the saddle is significantly lower than the middle point. We therefore assume that this is not caused by differences in hinge types and has a different cause. Figures 3.6b and 3.6c show that, although the differences in distance are significant, the saddle point is relatively close to the middle of the patch in the horizontal projected plane for all printed patches.

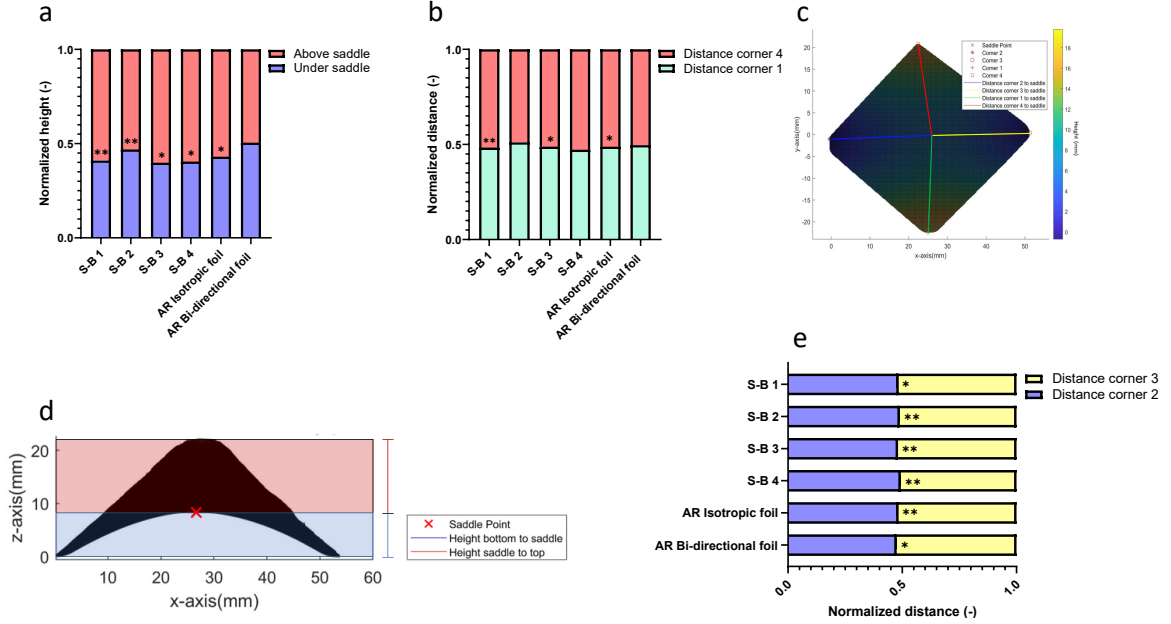


Figure 3.6: a: Normalized ratio of height of the saddle point to the corners in the vertical projected plane for all printed patches. b: Normalized ratio of distance of the saddle point to corners 1 and 4 in horizontal projected plane for all printed patches. c: Example of distance of saddle point to corners calculated in horizontal plane. d: Example of height of saddle point to corners calculated in vertical projected plane. e: Normalized ratio of distance of the saddle point to corners 2 and 3 in horizontal projected plane for all printed patches. ** $p < 0.05$, * $p < 0.01$.

3.2.2. Effect of foil type

The three different foil types were applied on two types of frames. A frame without hinges, consisting out of four separate rigid beams (NH frame) and the so called AR frame. For every foil type, the frame without hinges does not create a clear saddle. The created surfaces are completely irregular and the patches are not rigid as shown in figures 3.7a-c. Therefore, these three patches will not be taken into account in further measurements. The different foil types all form a saddle in combination with the AR frame as shown in figures 3.7d-e. There are, however, clear irregular wrinkles visible on the surface. For the isotropic foil these disturbances remain limited to the sides of the frame. The distortions for the uneven bidirectional and especially the unidirectional foil are visible over the complete frame. In addition, the unidirectional foil clearly skews the frame during folding. It is noteworthy that due to these irregularities, only the patches with uneven bidirectional foil and isotropic foil could be scanned. This means that for the unidirectional foil not all measurements could be performed. The first measured effects are visible in the previously introduced figure 3.6, where also the 'all rotation' patch with uneven bidirectional foil is incorporated. When the uneven bidirectional foil is used, the height of the saddle point lies almost perfectly in the middle, in contrast to the patches that use isotropic foil. This could be due to the difference in foil or due to the wrinkled disturbances on the surface of the uneven bidirectional foil patch. In the horizontal projected plane the saddle point of the uneven bidirectional patch is, similarly to the isotropic patches, relatively close to the middle point. Figure 3.8 shows that the mean curvature of the uneven bidirectional foil patch shows major disruptions on the spanned surface. This differs from the ideal situation, where the mean curvature would be zero everywhere. The mean curvature of the isotropic foil is closer to zero, but still a disturbance can be seen due to the wrinkled surface. The Gaussian curvature is predominantly negative for both patches. This indicates that both patches clearly form a saddle (negative Gaussian). For the uneven bidirectional foil patch however, this Gaussian curvature is more negative, which indicates that it is more hyperbolic. This is substantiated by the measured H_{RMS} and K_{avg} . The H_{RMS} is higher for the uneven bidirectional patch and the K_{avg} is more negative as shown in figure 3.9d.

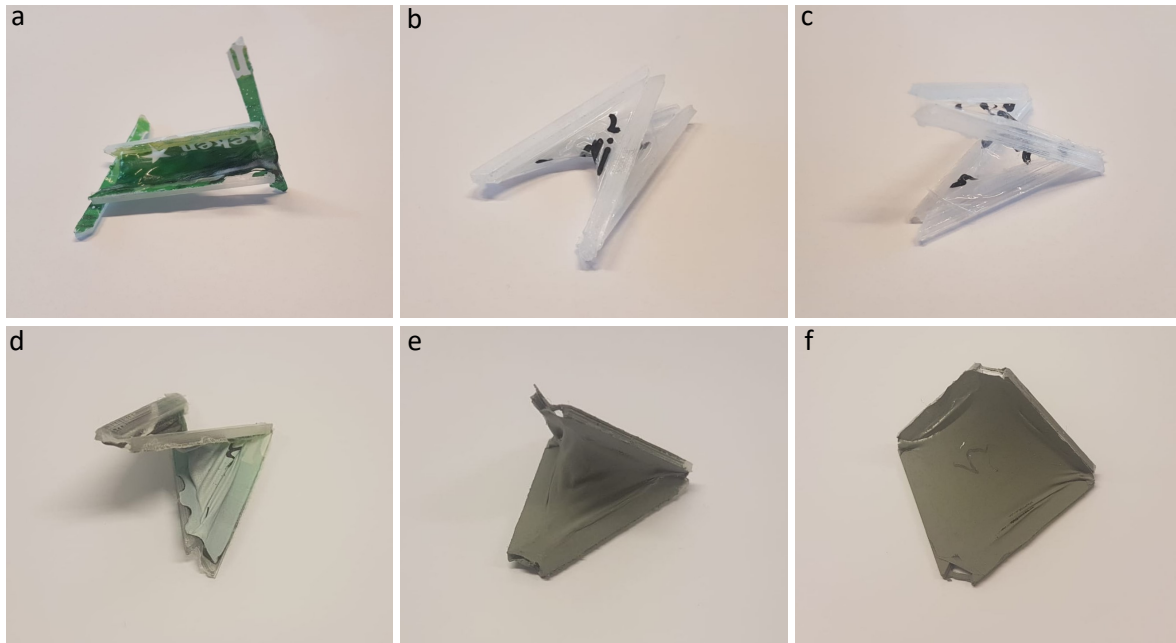


Figure 3.7: The folded printed patches with different foil types. a: Folded patch with unidirectional foil and frame without hinges b: Folded patch with uneven bidirectional foil and frame without hinges c: Folded patch with isotropic foil and frame without hinges d: Folded patch with unidirectional foil and AR frame. e: Folded patch with uneven bidirectional foil and AR frame. f: e: Folded patch with Isotropic foil and AR frame.

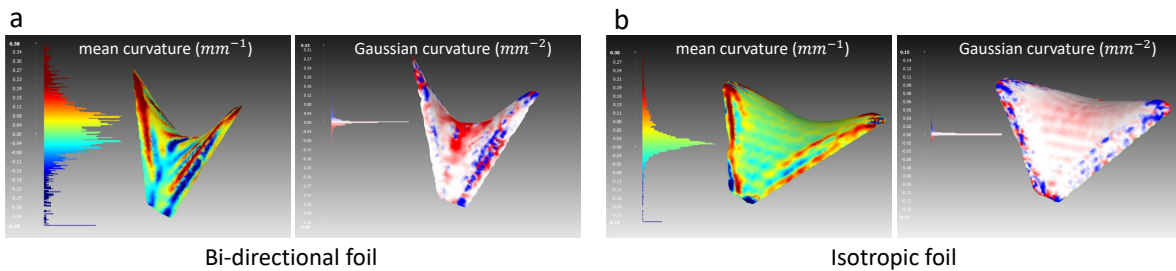


Figure 3.8: The mean curvature(mm^{-1}) and Gaussian curvature(mm^{-2}) for different foil types in combination with the AR frame. The mean curvature is shown on the left in RGB colours and the Gaussian curvature on the right in RWB colours.

The measured average of the opposite folded corner pairs shows clear differences for different foil types. As shown in figure 3.9a, the isotropic foil does not show a significant difference between both corner pairs. For the uneven bidirectional foil a small but significant difference is shown and for the unidirectional foil this difference increases. Note that the AR frame is used. This means that all four hinges are similar and the difference in between the corner pairs must be due to the different foil types. Again it is shown in figure 3.9b, that opposite corners bend similarly and show no significant difference. This shows that the average corner pair is a good representation of opposite corners for the printed patches with different foils. Next to the previously introduced difference in RMS mean and K_{avg} , the two global principal curvatures also show major differences. The k_1 and k_2 are larger for the uneven bidirectional foil compared to the isotropic foil. This could again be seen as an indication that shows that the uneven bidirectional foil is curved more. Furthermore, it is shown that there is no difference between k_1 and k_2 for the uneven bidirectional foil, where for the isotropic foil a significant difference is visible (figures 3.9c and 3.9f). Figure 3.9d shows the shrink percentage of the area of both the isotropic patch and uneven bidirectional patch, compared to the shrinkage of both foils without boundaries. Again it clearly demonstrates a significant difference between the patches and the unrestricted foils. This means that also the uneven bidirectional foils shrinkage is restrained by the frame. Note that the different observed effects can occur due to the difference in shrink type, but could also arise due to the difference in area shrink percentage of the different foil materials.

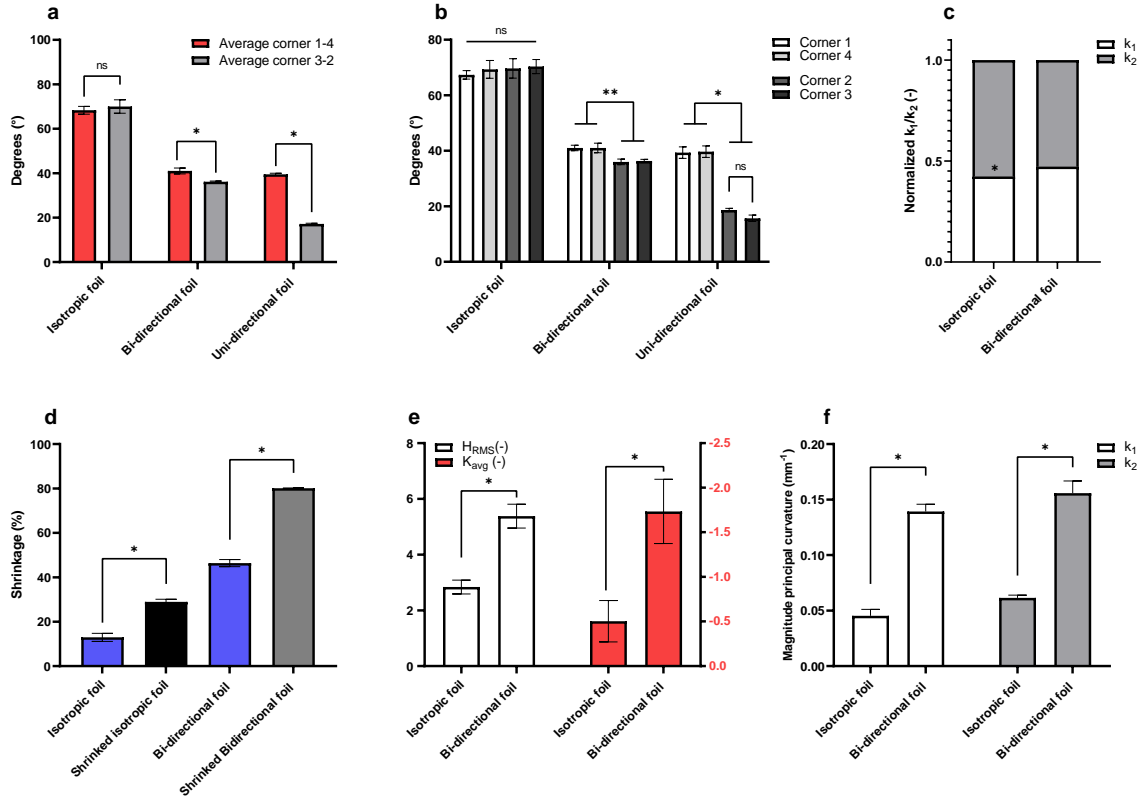


Figure 3.9: a: The average folded corner angle of opposite corner pairs for the AR frame with different foil types. b: The folded corner angle of each corner separately for the AR frame with different foil types. c: Normalized ratio between k_1 and k_2 for the AR frame and the uneven bidirectional and isotropic foil. d: Area shrink percentage of the different foils in combination with the AR frame compared with area shrinkage of isotropic and uneven bidirectional foil without constraints. e: H_{RMS} and K_{avg} for the AR frame in combination with isotropic and uneven bidirectional foil. f: global principal curvatures k_1 and k_2 for the AR frame in combination with different foil types. ** $p < 0.05$, * $p < 0.01$.

3.3. Behaviour of aluminium discrete patches

Three patches of every Al discrete patch type were made and activated. In total 21 different Al discrete patch types were created, which resulted in a total of 63 Al discrete patches. First the general effects will be presented and subsequently the effects of orientation, corner aspect ratio, temperature and time, beam thickness and scaling.

The folded Al discrete patch shows that the two opposite corner pairs bend in a different way, as shown in figure 3.10a. One pair slides towards each other, but stays (almost) in the same plane, while the other corner pair clearly bends out of plane. These different corner pairs are subsequently called the sliding and bending corners. Their axes of rotation are shown in figure 3.10b. It is arbitrary, which of the opposite corners will form the bending corner pair and which of the corners will form the sliding corner pair as shown in figure 3.10c. In other results, it will be shown that in general this bending corner pair folds further, compared to the sliding corner pair. It is visible that the patch forms a smooth saddle without distortions. Additionally, the folded patches are substantially stiffened due to the hardening of the SMP after cooling. For both examples below, the basic Al discrete patch design is used. This is the patch without any parameter differing from the basic Al discrete design and basic activation process.

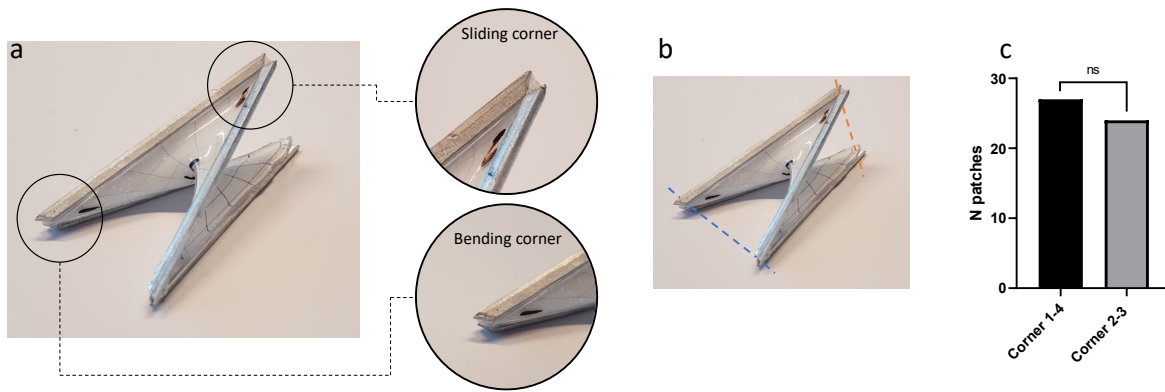


Figure 3.10: a: Example of folded Al discrete patch with two different corner types. Namely the sliding and bending corner. b: Example of folded Al discrete patch, where the two different axes of rotation are shown. c: Which of both opposite corner pairs forms the bending corner pair for all different square Al discrete patches $N_{total} = 52$.

The grid analysis of the basic Al discrete patch, shown in figure 3.11, shows an interesting effect. In the corners of the patch, the diagonal length of the grid stays almost similar in the direction towards the saddle and does not shrink. In the opposite direction, however, the length is 5.4 mm. Because the diagonal of the grid was initially 14.14 mm, this means that in this direction the grid shrinks approximately 61%. This is more than the 55% of length shrinkage that an unrestricted isotropic sheet would have. This difference shows that in the corners, the isotropic sheet is compressed in one direction, while the length stays almost constant in the other direction. Around the saddle, the grid has shrunk approximately 55% and 47% in both diagonal directions. These differences could be due to the fact that the grid is not perfectly in the middle of the saddle. However, it shows that the isotropic sheet in the middle shrinks approximately the maximum amount in length, or in other words, the same amount as an unrestricted isotropic sheet. Note that this measurement is qualitative and slightly distorted due to the curved surface.

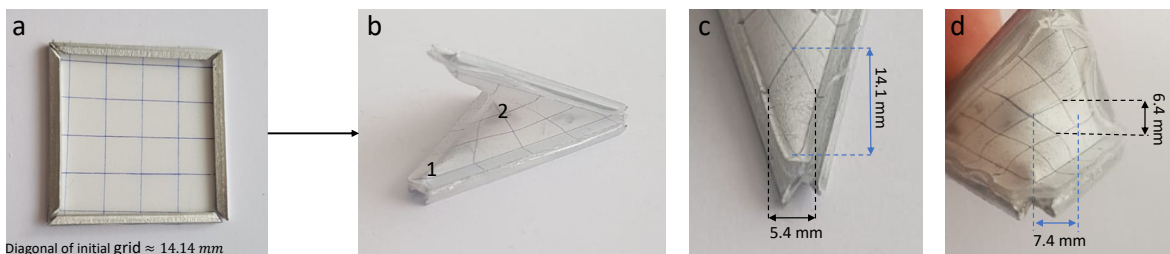


Figure 3.11: Grid analysis of the Al discrete patch. a: The grid applied on a patch before activation. b: Folded Al discrete patch after activation. The two locations focused on are marked (corner and saddle). c: Zoomed in picture of the grid in the corner area. d: Zoomed in picture of the grid in the saddle area.

3.3.1. Effect of orientation

Figure 3.12 shows that the orientation of the patch before activation does not have an effect on the folding process, as no significant differences are shown between the patches with these different orientations. Figure 3.12a shows that there is a clear difference between the folded corner angle of the bending and sliding corners, as previously introduced. This is remarkable since the Al discrete patch has no hinges in the corners and therefore all corners are the same before activation. This difference in folded corner angle subsequently results in a difference in the two global principal curvatures as shown in figure 3.12b. Lastly, there is a difference between the height above and under the saddle for the Al discrete patch in the vertical projected plane (figure 3.12c). This means that the formed saddle point is situated below the middle of the patch. This significant difference is noteworthy, as for an ideal patch the saddle would lie exactly in the middle.

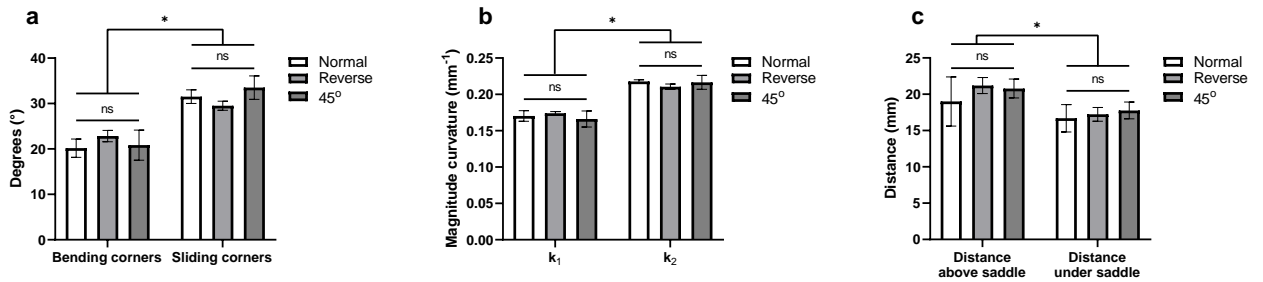


Figure 3.12: Results for different orientations of the Al discrete patch. a: Folded corner angle for different orientations of the Al discrete patch. b: Average global principal curvature for different orientations of the Al discrete patch ($\frac{k_1+k_2}{2}$). c: Height to saddle in the vertical projected plane for different orientations of the Al discrete patch. * $p < 0.01$.

3.3.2. Effect of corner aspect ratio

For the corner aspect ratio, it is shown that the opposite corner pair with the smallest angle (corner 1 and 4) always forms the bending corners. In other words, if the ratio between the two corner pairs is smaller than 1, the smaller corner pair will form the bending corners and the bigger corner pair will form the sliding corners (figure 3.13c). Figure 3.13a shows that the corner aspect ratio has a significant effect on the sliding corner pair. Its folded corner angle is lower if the corner aspect ratio is lower, or in other words, the sliding corner pair folds further in case of a lower aspect ratio. The average folded bending corner pair, however, shows no significant difference for different aspect ratio's. This means that the difference between the two folded opposite corner pairs increases, if the corner aspect ratio of the patch becomes lower. For this reason, one would expect the global principal curvatures to show an increased difference for a lower aspect ratio. However, this is not the case and the two global principal curvatures get closer to each other until for the lowest aspect ratio no difference is visible anymore. There are no significant differences shown for the shrunken area, H_{RMS} and K_{avg} for the patches with different aspect ratio's as shown in figures 3.13d and 3.13f. Figure 3.13f also indicates that the area shrink percentage of the isotropic sheet material of the patches is approximately 60 %. This again shows a clear difference with the maximum area shrinkage of 80 %, that an unrestricted isotropic sheet would shrink. This means that the Al discrete frame inhibits the shrinkage of the isotropic sheet material. Lastly, figure 3.13e shows that saddle of the patch becomes lower (closer to the bending corner pair) if the corner aspect ratio becomes lower.

3.3.3. Temperature and time effects

For the temperature and time effects, boundaries have been chosen for the average folded corner angle and the average global principal curvatures. Between these boundaries, the patch can be seen as a correctly folded patch. These conditions were based on the results of the initial Al discrete patch without any changed parameter, as previously introduced in figure 3.12. The boundaries were set on 25° and 28° for the folded corner angle and 0.19 mm^{-1} and 0.2 mm^{-1} for the average global principal curvatures. Both boundaries are shown in black in figures 3.14a and 3.14b and show similar results. For the average folded corner angle, the 'optimal' area is shown to be around an activation temperature of 170°C and an activation time of +/- 60 seconds. When a higher temperature is used, the patch should be initiated shorter and for a lower activation temperature the patch should be initiated longer. Under an activation temperature of 150°C, the patch will not fold at all. It shows that the ideal and most robust temperature is 170 °C. For this activation temperature, the patch will always fold correctly as long as the activation time is longer than 60 seconds. The measured global principal curvatures show a similar effect and a similar ideal temperature. For an activation time longer than 30 seconds in combination with an activation temperature of 190 °C, the global principal curvatures could not be measured. This was due to the fact that the patch collapsed and no saddle was formed as shown in figure 3.14c. This again proves that an activation temperature of 190 °C is not ideal.

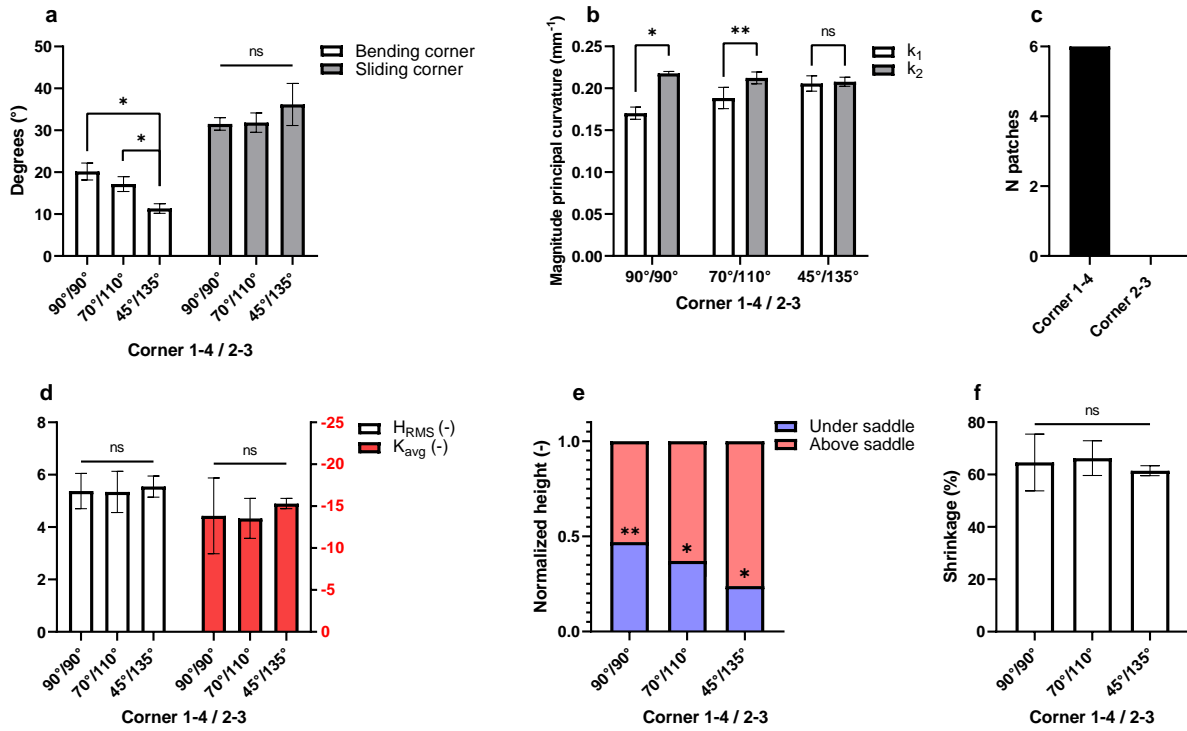


Figure 3.13: Results for different corner aspect ratio's of the Al discrete patch. A visualisation and explanation of the corner aspect ratio is given in section 2.2.2. a: The average folded corner of opposite corner pairs for different corner aspect ratio's. b: The global principal curvatures k_1 and k_2 for different corner aspect ratio's. c: This figure indicates which opposite corner pairs forms the bending corner pair. In this case only patches with corner aspects ratio's lower than 1 were selected ($N_{total} = 6$). d: H_{RMS} and K_{avg} for different corner aspect ratio's. e: Normalized ratio of the height of the saddle point to the corners in the vertical projected plane for different aspect ratio's. f: Area shrink percentage of the isotropic sheet materials for different aspect ratio's. **p < 0.05, * p < 0.01.

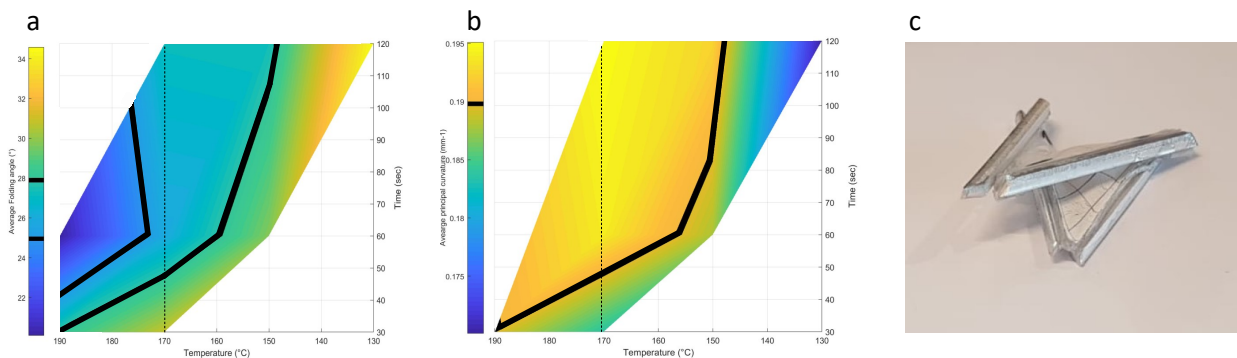


Figure 3.14: a: Activation temperature and activation time effect on the average folded corner angle of the Al discrete patch. b: Activation temperature and activation time effect on the average of the global principal curvatures of the Al discrete patch ($\frac{k_1+k_2}{2}$). c: Example of collapsed patch due to an activation temperature of 190°C in combination with an activation time longer than 30 seconds.

3.3.4. Effect of beam thickness

For a beam thickness lower than 0.1 mm, the Al discrete patch did not form a single saddle and a wrinkled and irregular surface was created as shown in figure 3.15e. A beam thickness of 0.3 mm did form a single saddle, but still the beams are clearly bend as shown in figure 3.15f. This is undesirable for the Al discrete patch, as the frame should act as a rigid constraint to the sheet. Therefore, in the measured results, we started with a beam thickness of 0.5 mm. With this beam thickness, a clear saddle was formed and the beams did not bend. Noteworthy is that the differences between the folded corner pairs, global principal curvatures and saddle height all disappear for a beam thickness lower than 1 mm as shown in figures 3.15a, 3.15c and 3.15d. The H_{RMS} shows no clear difference for different beam thicknesses and the Gaussian curvature shows an unexpected peak for a beam thickness of 4mm thickness. This is attributed to the thicker beams that caused distortion during the scanning process.

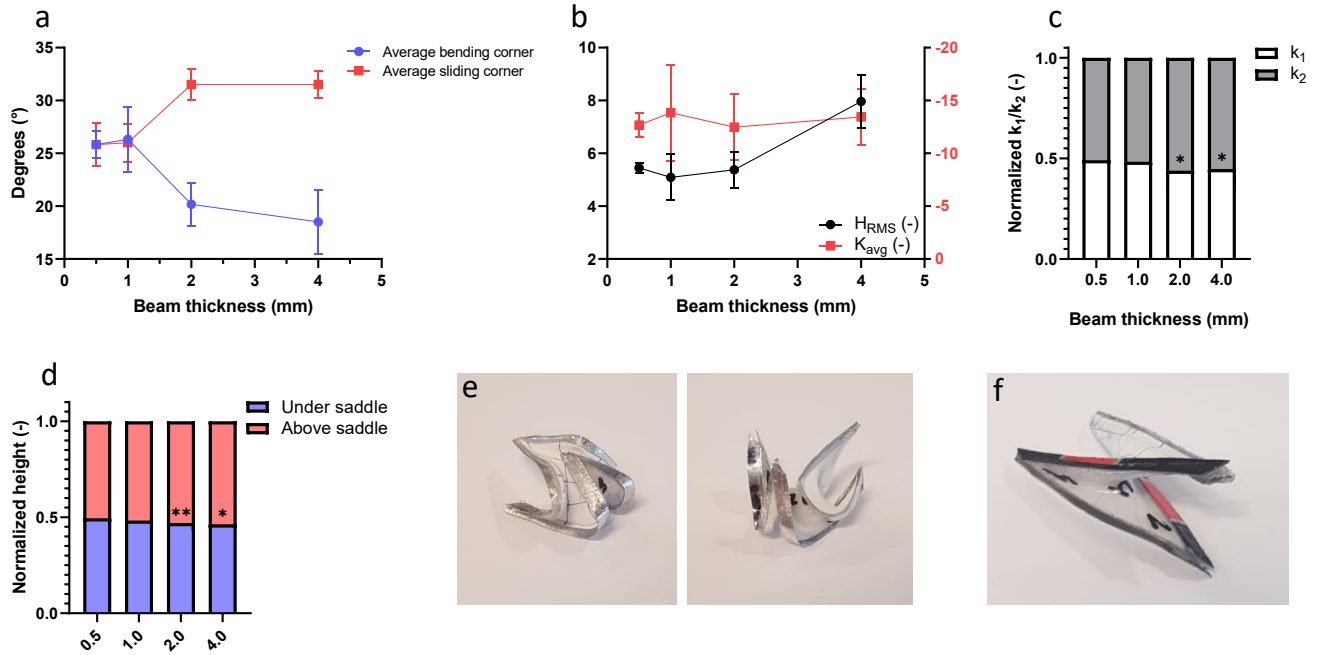


Figure 3.15: a: Average folded corner angle of combined corner pair for different beam thicknesses of the Al discrete patch. b: H_{RMS} and K_{avg} for different beam thicknesses of Al discrete patch. c: Normalized ratio between the global principal curvatures k_1 and k_2 for different beam thicknesses of Al discrete patch. d: Normalized ratio of the height of the saddle point to the corners in vertical projected plane for different beam thicknesses of Al discrete patch. e: Picture of folded patches with beam thickness of 0.1 mm. f: Picture of folded patch with beam thickness of 0.3 mm. ** $p < 0.05$, * $p < 0.01$.

3.3.5. Scaling effects

The patch scaled with a factor of 0.44x formed a clear saddle similar to the normal scale patches (1x). The 1.55x scale patch, however, did not form a saddle for two of the three tests. In these two cases the patch collapsed and therefore not all measurements could be performed for these patches. It is clearly shown that the difference between the bending corner pair and sliding corner pair increases if the scale increases (figure 3.16e). For the scale factor of 0.44x no difference is shown between the corner pairs at all. However, the 1.55x scaled patch shows an increased difference between both folded corner pairs. Interestingly, when the cross cross section of the beam is kept constant, while the rest of the patch is scaled, different results are shown. For these 0.44x scaled patches a significant difference between the folded corner pairs is shown. The 1.55x scaled patches, with a constant cross section, still show a significant difference between both folded corner pairs, but to a much lesser extent compared to the completely scaled 1.55x patch (figure 3.16d). The H_{RMS} clearly increases for an increasing scale, although for the 1.55 scale only one patch was scanned as discussed earlier. The K_{avg} showed a clear difference between the different scales as shown in figure 3.16f. The area of the patch obviously increases as the patch scale increases, there is however also a difference in shrink percentage noticed as shown in figure 3.16g.

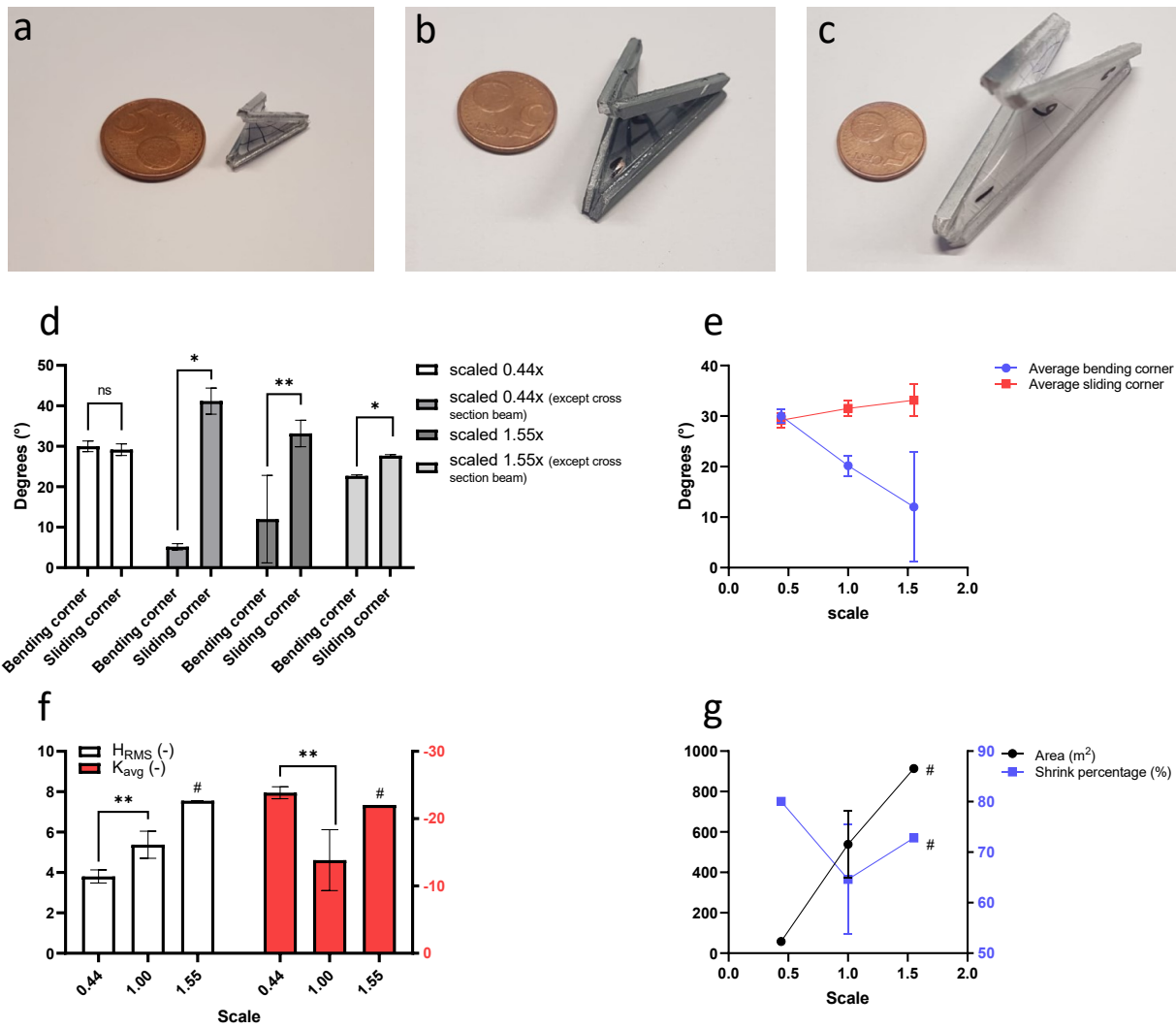


Figure 3.16: a: Al discrete patch scaled with a factor of 0.44x. b: Al discrete patch with normal scale. c: Al discrete patch scaled with a factor of 1.55x. d: Average folded corner angle of combined corner pairs for different scale with or without scaled cross section of the beam. e: Average folded corner angle of combined corner pairs for different scales of the Al discrete patch. f: H_{RMS} and K_{avg} for different scales of the Al discrete patch. g: Area and area shrink percentage for different scales of the Al discrete patch. Note: # Indicates that only one patch has been included in the calculation, as the other two patches collapsed. ** $p < 0.05$, * $p < 0.01$.

3.4. Behaviour aluminium continuous patches

The Al continuous patch clearly shows different effects for different values of the C_D coefficient introduced in the methodology. For a higher C_D the patch does not fold and the isotropic sheet material annihilates itself during activation. For a lower C_D the frame is bent and a saddle is formed. At a certain point, however, the C_D becomes too low and an irregular and warped surface is created. The results of the patch for different C_D are shown in figure 3.17a. Only the patches that form a clear saddle, or in other words the patches with a C_D of $2.63 \cdot 10^{-4}$ and of $1.45 \cdot 10^{-4}$, will be taken into account. For $C_D = 2.63 \cdot 10^{-4}$, the corners of the folded Al continuous frame are all equal as shown in figure 3.17b. For $C_D = 1.45 \cdot 10^{-4}$, however, differences between the corners are shown and a great deviation is found in the measurements. It should be noted that the SMP in the corners of these patches is damaged, as shown in figure 3.17d. This could explain the difference and inconsistency between the folded corner angles. The damage is probably caused by a too high tension in the material. For $C_D = 2.63 \cdot 10^{-4}$, this problem does not occur. Therefore, this patch will be taken into account in further measurements. Interestingly, all four corners of this patch show a similar bending effect and no differences can be seen between the folded corner pairs in contrast to the Al discrete patches. All corners bend outwards to the same extent and have a similar axis of rotation as shown in figure 3.17c.

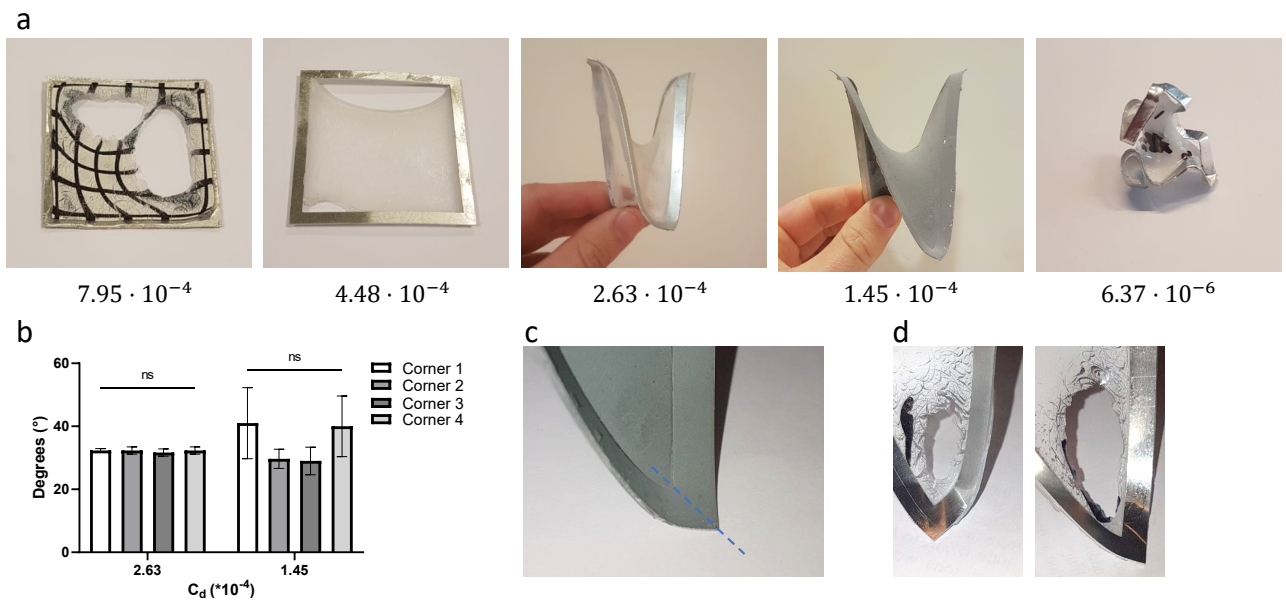


Figure 3.17: a: The folded Al continuous patch for different C_D 's. b: Folded corner angle of the Al continuous patch with $C_D = 2.63 \cdot 10^{-4}$ and $C_D = 1.46 \cdot 10^{-4}$. c: Example of bending axis for the Al continuous patch with $C_D = 2.63 \cdot 10^{-4}$. d: Example of damaged isotropic material in the corners of the continuous discrete patch with $C_D = 1.46 \cdot 10^{-4}$.

3.5. FEM model

3.5.1. Convergence

For a nodal distribution smaller than 6721 nodes, a time increment failure will occur and the model will not converge. For a higher amount of nodes, the model clearly converges. There is a maximum difference of 2.14% for the maximum von Mises stress and a maximum difference of 2.04% for the total strain energy, between all model runs with a nodal distribution higher than 6712. This is shown in figure 3.18. These percentages are clearly between the chosen maximum boundary of 5% and therefore a nodal distribution of 6721 nodes can be seen as sufficient for this model.

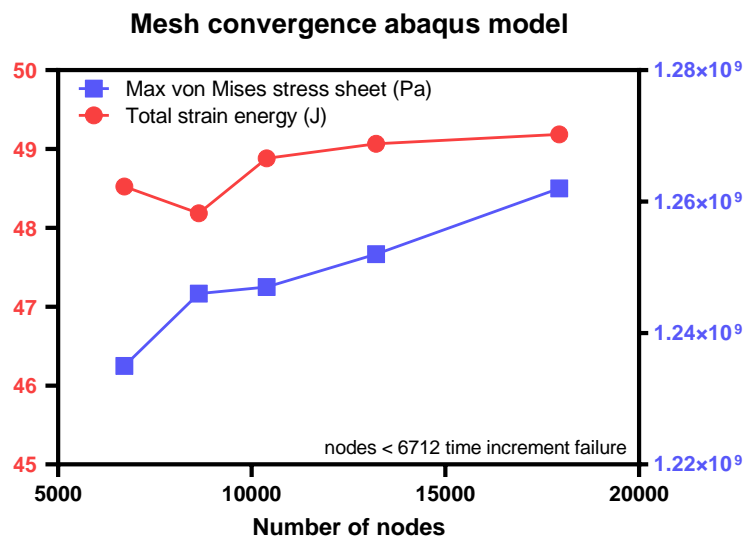


Figure 3.18: Maximum von Mises stress and maximum total strain energy of the Abaqus FEM model for different number of nodes.

3.5.2. Analysis of stress and strain distribution

In figure 3.19 the von Mises stress distribution during the simulated activation process is shown. When the folding process starts, a stress peak can be seen in the corners of the patch. Note that one opposite corner pair encounters a higher stress compared to the other opposite corner pair. This is attributed to the small perturbation applied in the beginning in order to initiate the folding process, as explained in the methodology. These corner differences disappear as the folding process progresses. The stress increases and slowly moves towards the middle of the patch, while the highest stress remains in the corners and the lowest stress occurs around the saddle. After approximately 70 seconds the stress in the patch starts to decrease slowly. When the folding process is almost finished the stress in the patch further decreases and a small area of higher stress arises around the saddle, which means that the stress in this area decreases more slowly compared to its surroundings. The process of relaxation after approximately 70 seconds can also be seen in figures 3.20a and 3.20b. The von Mises stresses in both the corner of the patch and around the saddle point of the patch show a clear peak and relaxation afterwards. Although this peak occurs earlier in the corner and the von Mises stress in the corner is significantly higher. The total strain energy of the model, shown in figure 3.20c, substantiates this relaxation and clearly shows a peak around 70 seconds. Afterward, the total strain energy decreases and becomes constant.

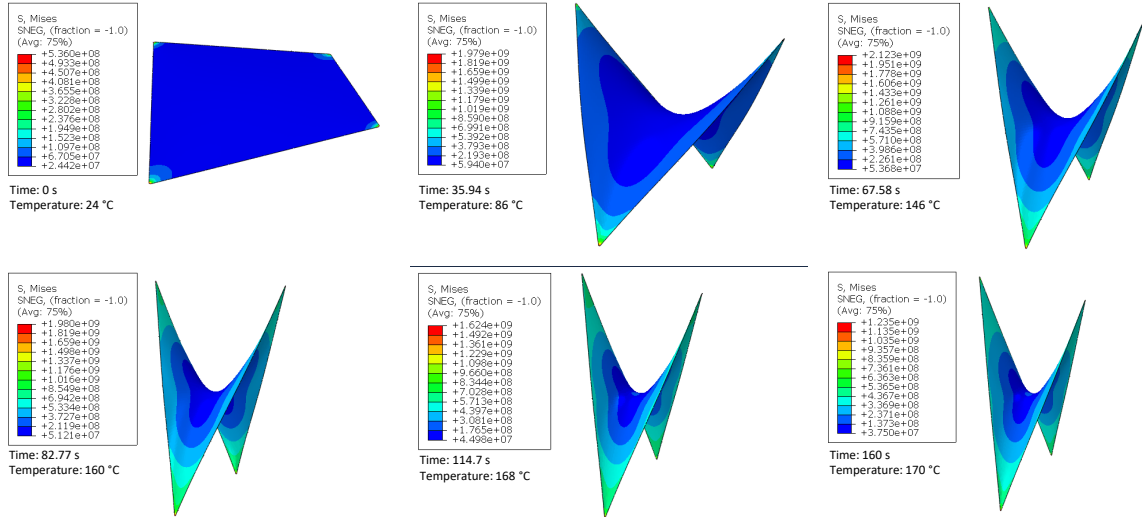


Figure 3.19: Changes in von Mises stress in the SMP of the Abaqus FEM model during activation. Note: stresses in the rigid frame are not taken into account.

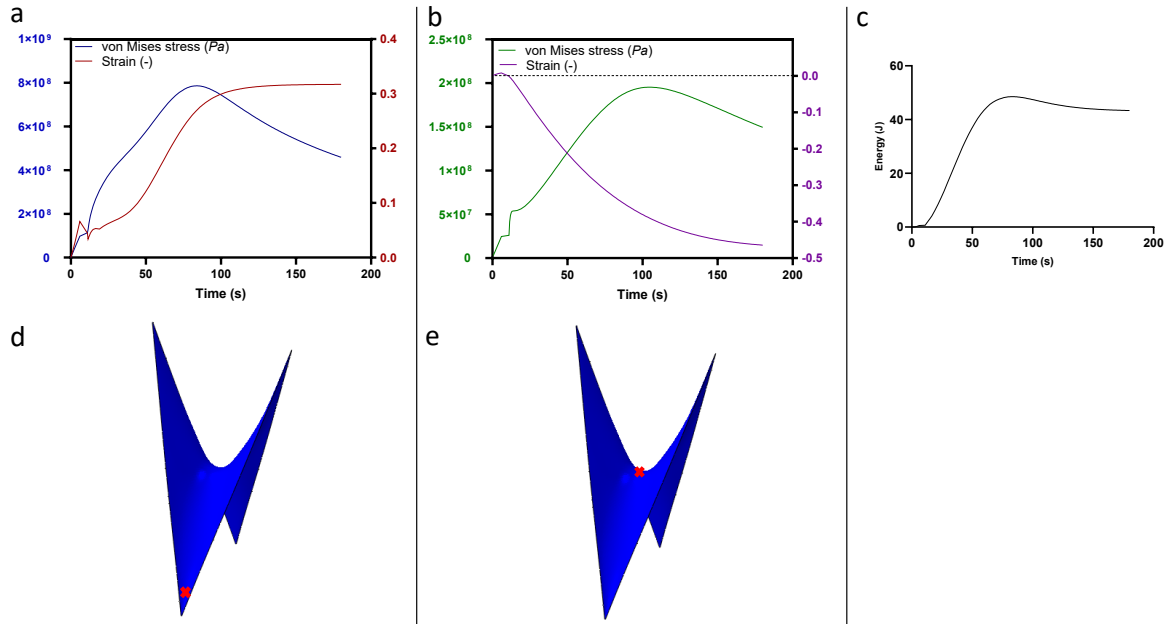


Figure 3.20: a: von Mises stress and engineering strain in a corner element of the Abaqus FEM model during activation. b: von Mises stress and engineering strain in a saddle element of the Abaqus FEM model during activation process. c: Total strain energy of the complete Abaqus FEM model during activation. d: Visualisation of the corner element used in 3.20a. e: Visualisation of the saddle element used in 3.20b.

In figure 3.21 the logarithmic strain, or so called true strain, during the activation process of the FEM model is shown. This logarithmic strain is linked to 'general' engineering strain with the equation shown below (3.1). Where ϵ_{log} is the logarithmic strain, ϵ_{eng} the engineering strain and λ the extension ratio.

$$\epsilon_{log} = \ln(\epsilon_{eng} + 1) \rightarrow \epsilon_{eng} = \lambda - 1 \quad (3.1)$$

In the beginning, a small extension can be seen in the corners. Again, this is the result of the small perturbation applied in the beginning. Subsequently, during the activation process the sheet material around the corners shows an increasing positive logarithmic strain, which means that this part of the sheet is extended. This is interesting as the SMP itself is programmed to shrink with increasing temperature. Towards the middle of the patch, an opposite effect is demonstrated and the logarithmic strain becomes increasingly negative,

which means that the sheet shrinks at this location. There is a transition area from the corners towards the middle, where the sheet extension turns into sheet shrinkage. This area is shown in light green. This result is substantiated by graphs a and b of figure 3.20, where the engineering strain in a corner element and a saddle element are shown. In the corner element the strain clearly is increasingly positive, until it becomes constant when the patch is completely shrunk. The saddle elements shows an opposite effect and the strain becomes increasingly negative, during the activation process. In the beginning, however, there is a small positive strain shown in the saddle element. This is due to the initial perturbation.

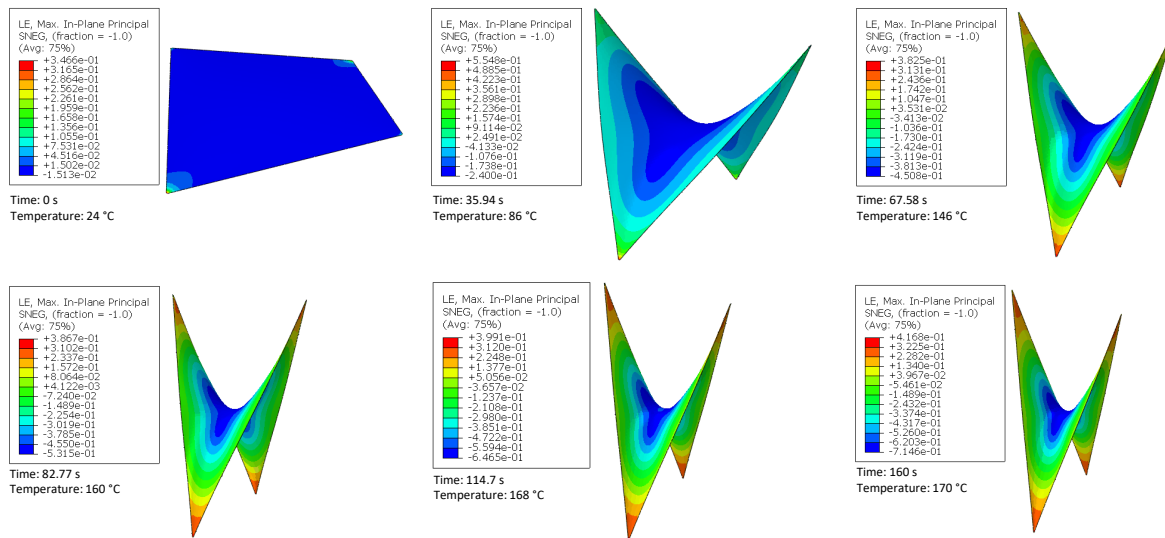


Figure 3.21: Changes in logarithmic strain in the SMP of the Abaqus FEM model during activation process. Note: strain in the rigid frame is not taken into account.

3.5.3. Validation

First the FEM model is compared with the Al discrete patch as the model is based on this design. The first notable difference between the model and the experiment patch is the activation time. The activation time of the experiment patch is approximately 60 seconds at a temperature of 170 °C, while activation of the FEM model takes 160 seconds. This difference is attributed to the chosen sheet thickness of the model. The thickness of the real isotropic sheet material starts around 0.2 mm and increases to 2 mm during activation. The thickness of the sheet in the FEM model was immediately set on 2 mm. This means that heating this material takes longer compared to the experiment patch. The folded corner angles and saddle height of the activated model are compared with the 'standard' Al discrete patch with a beam thickness of 2 mm and with the thinner Al discrete patch with a beam thickness of 0.5 mm. As shown in figure 3.22, the FEM model shows a great resemblance with the 'thinner' Al discrete patch for both the folded corner angles and the saddle height.

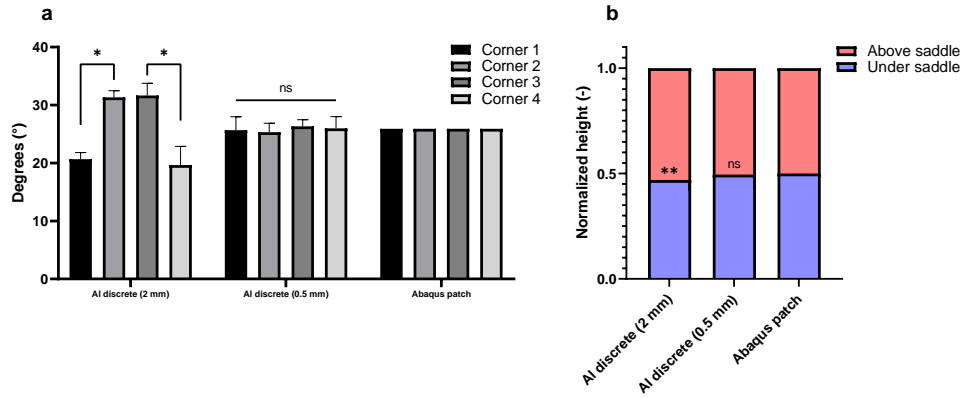


Figure 3.22: a: Folded corner angle of the Abaqus FEM model and the AI discrete patch with a beam thickness of 2 mm and 0.5 mm. b: Normalized ratio of height of saddle point to the corners in the vertical projected plane for the Abaqus FEM model and the AI discrete patch with a beam thickness of 2 mm and 0.5 mm. * $p < 0.01$.

This resemblance is further shown in figure 3.23. In this figure the scanned AI discrete patch, with 0.5 mm beam thickness, is superimposed over the final FEM model and compared using the Hausdorff distance. Around the saddle and at the sides of the patch clear differences are shown. However, with a RMS Hausdorff distance of 0.71 mm, the FEM model fairly resembles the real AI discrete patch.

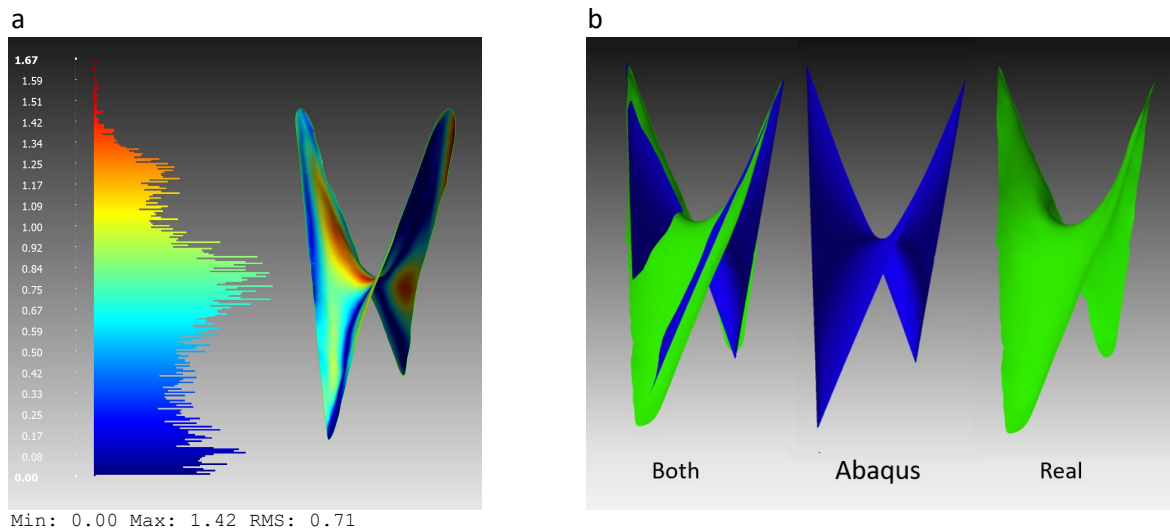


Figure 3.23: a: Hausdorff distance between activated AI discrete patch (with 0.5 mm beam thickness) and the Abaqus FEM model, the distance is projected on to the AI discrete patch. b: The 0.5 mm beam thickness AI discrete patch superimposed over the Abaqus FEM model.

Lastly, the outer boundaries of the activated FEM model were imported as a constraint into Surface evolver. The surface area between these boundary conditions is numerically minimized, which results in the surface shown in figure 3.24b. Subsequently, this 'idealized' surface is compared with the surface created with the FEM Model. While the saddle height and the edges of the patch show great resemblance, clear differences are shown in the areas between the corners and the saddle. The comparison shows that the surface of the 'idealized' patch rises steeper towards the saddle, compared to the surface of the FEM model.

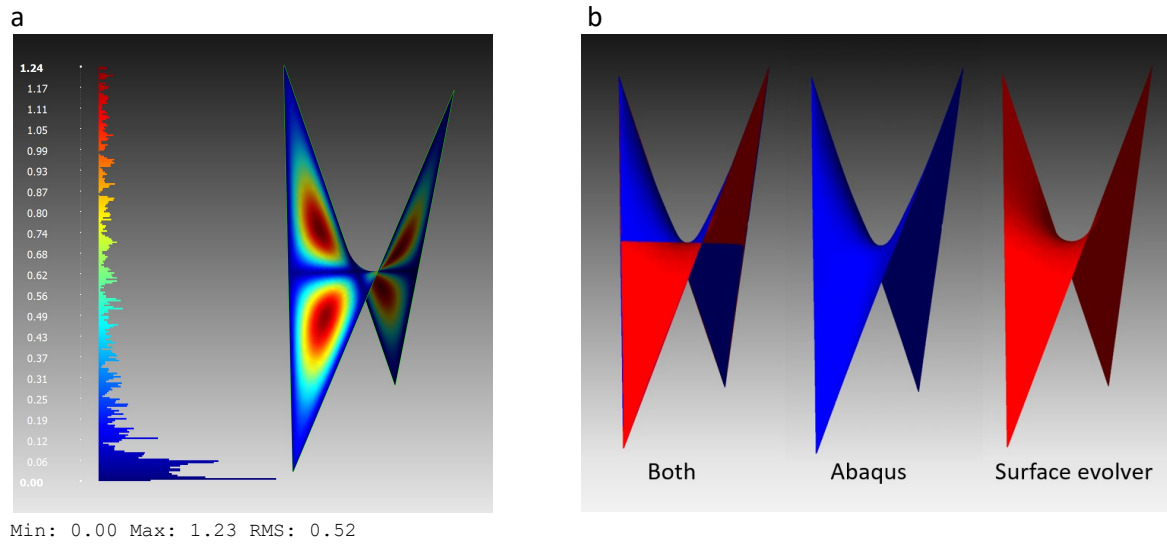


Figure 3.24: a: Hausdorff distance between the 'idealized' surface created in surface evolver and the FEM model, the distance is projected on to the surface of the FEM model. b: The 'idealized' surface created in surface evolver superimposed over the surface created with the FEM model.

4

Discussion

4.1. Patch design for hyperbolic shape-shifting

In this research, it is demonstrated that the frame design has different major influences on the shape-shifting process of the patch. First, the specific design and the stiffness of the hinge could influence the folding process. Lowering the stiffness of the hinges ensures that the patch has a higher folding angle. Subsequently, this results in the patch being more hyperbolic. This was shown by an K_{avg} that became more negative and by the increase of both global principal curvatures, when the patch was folded more. The downside of the lower hinge stiffness was, however, that the further the patches were folded, the more their H_{RMS} increased and deviated from zero. This result shows a trade-off: On the one hand, it is important for the shape-shifted patch to be curved in order to be able to create various hyperbolic surfaces, but on the other hand the H_{RMS} needs to be as close to zero as possible. The latter is desirable because the lower H_{RMS} means that the substrate is closer to a minimal surface. The patches with an average folded corner angle of $\pm 88^\circ$, for example, have a very low H_{RMS} . The surface is, however, close to a flat surface and therefore this low H_{RMS} is not valuable. This trade-off is substantiated in figure 4.1, where the average global principal curvatures, K_{avg} and H_{RMS} are given as a function of the folded corner angle of the patch. The average folded corner angle is seen as an indication for how much the shape-shifted patch is folded. An unfolded patch obviously has an average corner angle of 90° : the further the patch is folded, the lower this average corner angle will be.

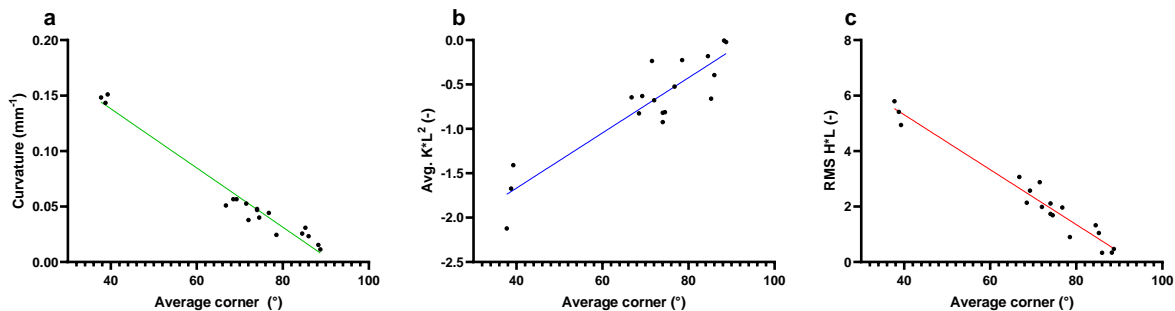


Figure 4.1: a: Average global principal curvature as a function of folded corner angle for every printed patch ($\frac{k_1+k_2}{2}$). b: K_{avg} as a function of folded corner angle for every printed patch. c: H_{RMS} as a function of folded corner angle for every printed patch.

Next to the stiffness of the hinges, the hinge type also has a major influence on the shape-shifting of the patch. For the 3D-printed patches, a frame with hinges is needed in order for the patch to form a saddle. This was demonstrated since the NH frames formed an irregular, collapsed shape with little stiffness. Which also means that the SMP foil itself, used in case of the printed frames, cannot provide this rigidity to the patch. The frames with hinges create differences in the folding process of the patch. The 3D-printed AR frame shows that all corners fold to the same extent, when all four hinges of the patch are equal. The 3D-printed S-B frame, however, clearly induces a difference between the folded opposite corner pairs. The bend hinge pair folds to

a large extent, while the slide hinge pair shows a small degree of folding. This indicates that with different hinge combinations, a difference between the opposite folded corner pairs can be created as shown in figure 4.2a. In order for the patch to fold with an equal degree for every corner, the bending axis at the hinges has to change during the folding process. The AR frame and the aluminium discrete and continuous frame allow this change in bending axis, while the S-B frame does not. Both the slide and bend hinges have one single bending axis, that does not change during the folding process. Therefore, a difference between the folded opposite corner pairs can be observed for the folded S-B patches. A kinematic approach of how the patch folds, assuming that all corner angles remain equal, is added to appendix D.1. This approach confirms that the bending axes of the corners change during the folding process. It is not determined whether the patches actually fold this way, as only the start and end point of the folding process is reviewed for the experimental patches. The FEM model, however, shows a similar folding pattern as this kinematic approach.

Apart from the effect on the folding process, the hinges have another notable effect. The 3D-printed patches (with hinges) all show that their saddle point lies closer to the middle in the horizontal projected plane as shown in figure 4.2b and 4.1c. Both aluminium patch types, however, show a significant deviation from the saddle to the middle point. This measure, the location of the saddle point, could be seen as a quantification of how uniform the folding process of the patches took place. Seemingly, the hinges of the 3D-printed patches ensure a more uniform folding process, compared to the aluminium patches (which have no hinges). However, this difference could also be caused by the difference in SMP of the 3D-printed and aluminium patches and the difference in activation method of both patch types. The isotropic sheet SMP, used for all aluminium patches, shrinks more compared to the isotropic foil (used for the 3D-printed frames). This increase in shrink percentage could also cause the deviation of the location of the saddle point.

Interestingly, the folding process could also be changed by the corner aspect ratio without the need of hinges. Our experiments have shown that this corner aspect ratio, for example, could determine which corner pair forms the bending corners and which corner pair the sliding corners for the Al discrete patch, and could induce changes in the curvature of the folded patch. For an overview of the corner aspect ratio effects, reference is made to figure 3.13.

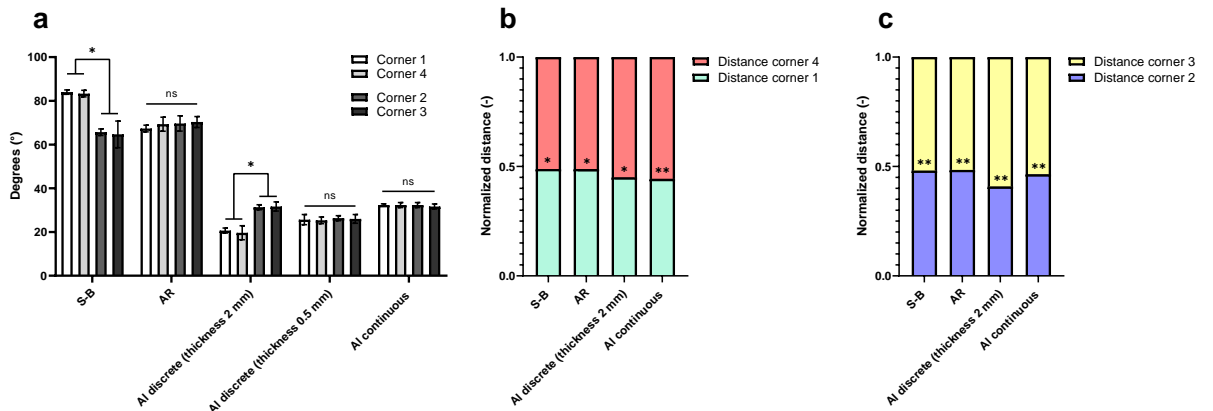


Figure 4.2: a: Folded corner angle for different patch types. b: Normalized ratio of distance of the saddle point to corners 1 and 4 in horizontal projected plane for different patch types. c: Normalized ratio of distance of the saddle point to corners 2 and 3 in horizontal projected plane for different patch types. $p < 0.05, p < 0.01$. Note: for the S-B patch, the frame with a stiffness of 9400 N/m for both hinge types was selected and for the Al discrete patch the frame with a thickness of 2 mm and 0.5 mm. The Al continuous patch with $C_d = 2.63 \cdot 10^{-4}$ is shown. For all patches in this figure the isotropic foil or isotropic sheet SMP was used.

From the different experiments, it can also be concluded that the thickness, and thus stiffness, of the frame plays an important role in the shape-shifting process. For the Al discrete patch, it was shown that with a beam thickness under a certain threshold, the stiffness of the frame became too low and an irregular and warped surface was created (beam thickness < 0.3 mm). For all Al discrete patches with a higher beam thickness, a single saddle was formed. There are, however, still significant differences between these patches with a higher frame thickness. For the beam thicknesses of 2 mm and 4 mm, differences between the opposite

folded corner pairs were formed. Subsequently, differences between the global principal curvatures and saddle height were observed. This difference, however, disappeared for a beam thickness of 0.5 mm and 1 mm and all folded corner angles became equal (figure 3.15). A possible explanation for this difference might be the effect of gravity on the frame. For a higher beam thickness, the beams have an increased mass. Because of this mass, the frame collapses to a small extent during the folding process. For thinner frames this effect does not occur. This could also explain why the FEM model corresponds to the Al discrete patch with a thickness of 0.5 mm and not to the patch with a thickness of 2 mm. In the FEM model, gravitational effects are not taken into account. This line of thought can be extended to the effects observed during the scaling of the Al discrete patches. The SMP thickness is constant, which means that the SMP is only scaled by its area. The frame, however, is scaled by its volume. This means that when the patch is scaled with a factor of 0.44, the volume of the sheet increases compared to the volume of the frame. This has the consequence that the shrink force of the sheet increases compared to the mass of the frame. This could substantiate why for the patch, scaled with factor 0.44, no difference between the folded corner angles is shown as the influence of mass diminishes. For the patch, scaled with factor 1.55, this concept works the other way around and the shrink force of the sheet becomes smaller compared to the mass of the frame. Subsequently, the difference between the opposite folded corner pairs becomes larger for this patch, as previously shown in figure 3.16. This also explains why this effect is opposed, when the cross section of the frame is kept constant during scaling. Now the mass of the frame is scaled with its length, while the SMP is still scaled with its area. In this case the patch scaled with a factor of 0.44 shows an increased difference between the opposite corner pairs, while the patch scaled with a factor of 1.55 shows a decrease in this difference. This is shown in figure 3.16f.

The differences observed between the Al continuous patches can be explained in a similar way. The constant parameter C_d , introduced in the methodology and repeated below (equation 4.1), contains the thickness of the sheet and the stiffness of the frame. For a lower C_d , the stiffness of the frame decreases compared to the volume of the sheet. In other words, the shrink force of the complete sheet increases compared to the stiffness of the frame. Subsequently, for a high C_d the patch does not fold and for a lower C_d the frame does. Under a certain threshold the C_d becomes too low and the shrink force of the sheet is too high compared to the stiffness of the frame. This results in a patch that forms an irregular and warped surface, when activated.

$$C_d = \frac{E_f b_f t_f^3}{E_s t_s L^3} \quad (4.1)$$

This result shows similarities to the research of Giomi et al [24]. In this research, a so-called Euler-Plateau equation is formulated for a minimal surface bounded by elastic lines. The physical realisation of this idea is a soap film bounded by a deformable wire frame as shown in figure 4.3a. This equation links the surface tension of the soap film to the stiffness of the wire frame and is noted below 4.2. In this equation σ is the surface tension of the soap film, L the length of the wire frame, E is the Young modulus and I is the area moment of inertia of the wire frame. If the value C_e increases, the surface tension becomes larger compared to the stiffness of the wire frame. This results in a surface that becomes more hyperbolic as shown in figure 4.3b. As mentioned above, this is similar to what is shown for the Al continuous patches, only in this case the shrink force generated by the SMP is considered, instead of the surface tension. In order to substantiate this resemblance, aluminium circular frames were designed with an increasing diameter. These frames were combined with an isotropic sheet SMP and activated. For a larger diameter, the trade-off between the shrink force and the stiffness of the circular frame increases, which corresponds to a higher C_e . These shape-shifted frames indeed follow the same trend and become more hyperbolic for larger diameters as shown in figure 4.3c.

$$C_e = \frac{\kappa L^3}{EI} \rightarrow \kappa = \sqrt{\frac{3\sigma}{4}} \quad (4.2)$$

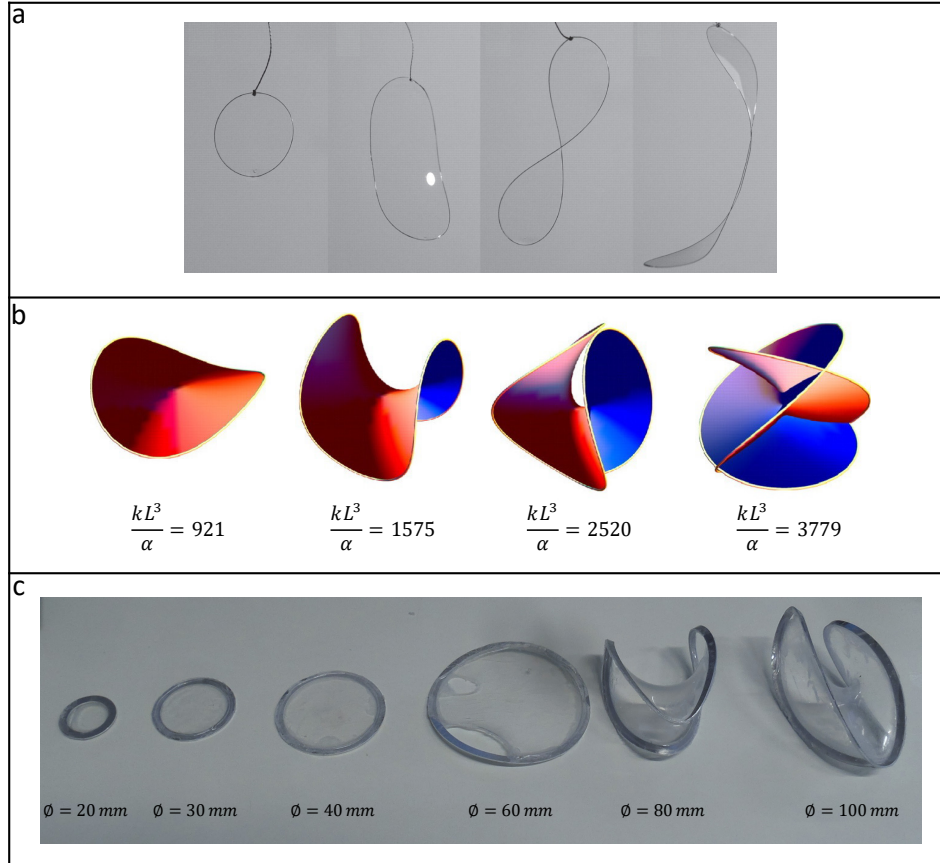


Figure 4.3: a: Different examples of soap films bounded by a deformable wire frame [24]. b: Solutions of the Euler-Plateau problem for increasing values of C_e [24]. Shape-shifted aluminium circular frames with an increasing diameter, as SMP the isotropic sheet material is used.

A last important finding considering the frame design for hyperbolic shape-shifting, is that seemingly the orientation of the frame does not influence the shape-shifting process. This is a positive outcome considering the different future applications of the hyperbolic shape-shifting concept. When larger structures of different connected patches are created, these patches will be orientated in different ways. It seems that these different orientations will not influence the folding process of the single patches. However, it is expected that mass will play an increasing role in these larger structures and this probably will influence the folding process.

4.2. Material selection for hyperbolic shape-shifting

An important trade-off needs to be made, when selecting the SMP and frame material for the shape-shifting process. In order to prevent melting or softening of the frame material, it should be able to withstand the activation temperature needed to activate the SMP. Aluminium, for example, could be seen as an ideal frame material as its melting point is far above the activation temperature of SMP's. The downside of an aluminium frame is, however, that the fabrication of compliant hinges is difficult and that it is a relatively heavy material compared to plastics. Therefore in our experiment, we chose the more complex frames to be 3D-printed with Polycarbonate. This material has a glass transition temperature around 112 °C and was therefore only compatible with the SMP foil's and not with the isotropic sheet. Metal 3D-printers could solve this problem and it is shown that, for example, compliant hinges can be made with this fabrication method [11] [43]. Unfortunately, during our research no metal printer was available and the simple compliant hinges used in our research probably cannot be realized in metal, let alone with metal 3D-printers.

Interesting differences were observed between the foils and the sheet material. This section first addresses the difference between the isotropic sheet and the isotropic foil (the other two foils will be discussed later). The first main difference is the rigidity of the SMP after activation. It is shown that the foil on itself cannot

maintain the stiffness of the frame and that a foil patch without hinges forms an irregular collapsed shape with little stiffness. When the frame has hinges, the foil can tighten itself between the frame which results in a higher stiffness and a saddle formation. The isotropic sheet does not need hinges, as the SMP sheet itself can provide the rigidity of the patch. This difference is probably caused by the difference in thickness of both materials, as the sheet is approximately ten times thicker than the foil. Next to that, the elastic modulus of the SMP sheet material (PS) is also approximately four times larger than the elastic modulus of the foil material (PE) [21]. Another interesting difference is the wrinkled surface created on some isotropic foil patches. The patches with the isotropic sheet material never exhibited this effect. As shown in the grid analyses and in the strain analysis of the FEM model, the complete sheet does not shrink to the same extent. In the corners of the patch the sheet is, for example, compressed, while around the saddle point maximum shrinkage of the SMP takes place. This strain difference in the sheet could induce this wrinkling (buckling) of the sheet material. The reason that the foil buckles and the sheet material does not, is again attributed to the thickness of the material. Since the sheet SMP is thicker, it can resist this buckling of the sheet more easily and, therefore, no wrinkled surface is formed.

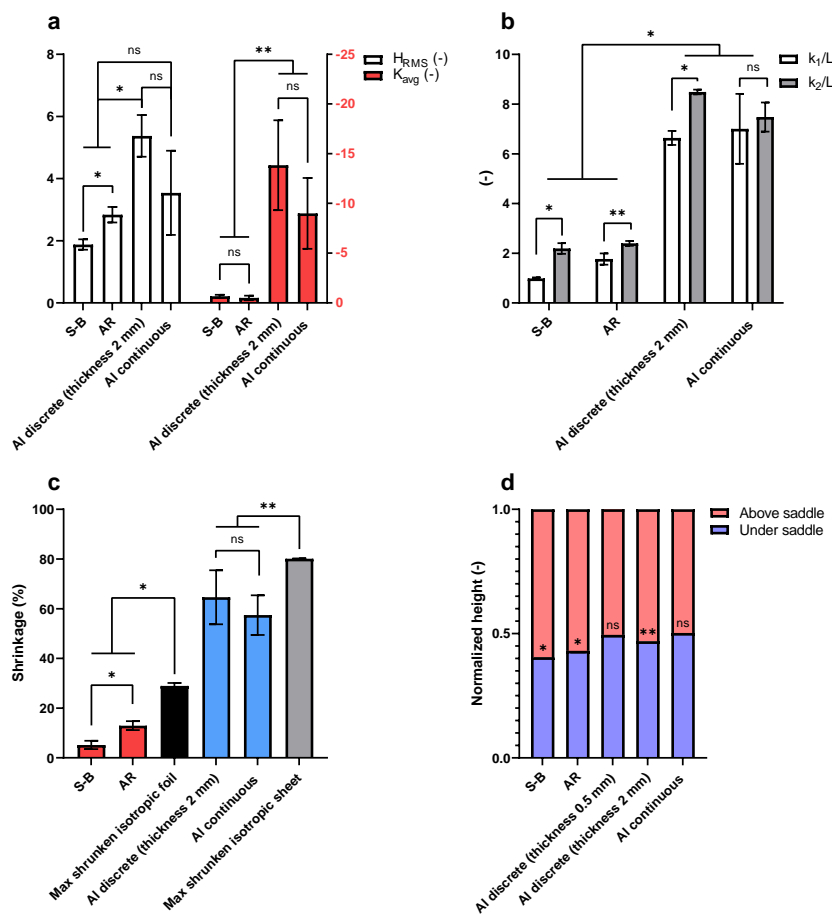


Figure 4.4: a: H_{RMS} and K_{avg} for different patch types. b: The dimensionless global principal curvatures $k_1 \cdot L$ and $k_2 \cdot L$ for different patch types, the global principal curvatures are made dimensionless by multiplying them with the patch length. c: Area shrink percentage of different patch types compared with maximum area shrinkage of isotropic foil and isotropic sheet. d: Normalized ratio of height of saddle point to the corners in the vertical projected plane for different patch types. $p < 0.05, p < 0.01$. Note: for the S-B patch, the frame with a stiffness of 9400 N/m for both hinge types was selected and for the Al discrete patch the frame with a thickness of 2 mm and 0.5 mm. The Al continuous patch with $C_d = 2.63 \cdot 10^{-4}$ is shown. For all patches in this figure, the isotropic foil or isotropic sheet SMP was used.

Figure 4.4a and 4.4b show that the global principal curvatures are higher for the aluminium patches, compared to the printed patches. Next to that, the K_{avg} is approximately 25x more negative for the aluminium

patches. Both measures indicate that the folded aluminium patches are more hyperbolic. This difference can be attributed to the different SMP's used for both patches. The SMP sheet has a higher shrink percentage compared to the foil. The aluminium patches, that all use an SMP sheet, therefore fold further compared to the printed patches, that all use an SMP foil. It is also shown that the H_{RMS} increases for the aluminium patches. This corresponds to previous results, that show that the H_{RMS} increases, when patches are folded further (figure 4.1). Figure 4.4d shows that the saddle point for the printed patches, that all use isotropic foil, lies lower than the middle of the patch. For most aluminium patches, that all use an isotropic sheet, the saddle point is almost in the middle. A possible explanation for this difference might again be the foil and sheet material used. The printed frames have hinges and the used foil is relatively thin. When the printed patches fold, the foil tightens itself between the frame. This presumably results in a high tension in the foil. The combination of this high tension and thin foil, ensures that the foil is slightly stretched. Subsequently, the saddle point of the patches with foil becomes lower. The SMP sheet is thicker and will therefore be stretched less, therefore the saddle point is not lowered for the aluminium patches. This idea is substantiated by the results shown in figure 4.4c. In this figure the different area shrink percentages of the patches are compared with the maximum shrink percentage of their corresponding SMP. As demonstrated, the maximum shrink percentage of the foil is approximately two/four times larger than the shrink percentage of the printed patches (that use foil). The difference between the aluminium patches and the maximum shrink percentage of the SMP sheet is much lower. This indicates that the shrinkage of the foil patches is indeed opposed more, compared to the shrinkage of the sheet patches. This substantiates that the foil is stretched.

A last notable difference between the SMP sheet and the SMP foil, is that the sheet material tore itself in some cases as previously shown in figure 3.17c. The patches that used foil, however, never showed this effect. Especially for SMP sheet patches with a large sheet area, this tearing effect was shown. It is assumed that the stresses in the sheet become too high locally and subsequently, the sheet ruptures. The foil does not show this effect as the foil has a lower shrink force, moreover the foil can behave more elastic as the foil is significantly thinner. This allows the foil to better absorb these stress peaks.

The use of different foil types than isotropic foil, showed negative results. The unidirectional foil completely skews the frame and creates a wrinkled surface. The uneven bidirectional foil also creates a wrinkled surface, but to a lesser extent. Because of these wrinkles, the H_{RMS} of these patches is larger compared to the same patches with isotropic foil. As discussed earlier, an increase in H_{RMS} is undesirable. Interestingly, the uneven bidirectional foil also induces a difference in the folded opposite corner pairs. By using this effect, the folding of the patches can be manipulated in different ways, without the need for hinges. The undesired wrinkled surface is probably again caused by the relatively low thickness of the foils in combination with the anisotropic behaviour explained earlier. This anisotropic behaviour increases the strain differences in the SMP and thus increases the wrinkling of the surface of the SMP. It would be interesting to test whether anisotropic sheet SMP's show similar behaviour. Unfortunately, anisotropic sheet SMP could not be obtained and therefore was not used in this research.

4.3. SMP shape-shifting and the “idealized” minimal surface

Significant differences are shown between the 'idealized' surfaces created with surface evolver and all experimental patches, as shown in figure 4.5. The printed patches have saddle points that are lower compared to their 'idealized' patches (4.5a and 4.5b). As discussed, this could be attributed to the stretching behaviour of the foils. The aluminium patches have a saddle point that lies in the middle of the frame, which explains their lower RMS and max Hausdorff distance as shown in figure 4.5c. Still, however, both the aluminium discrete and continuous patches show a deviation from their 'idealized' surface. This deviation is shown in figures 4.5d and 4.5e. Although the saddle point of the aluminium patches is in the middle, their 'idealized' surface rises steeper towards the saddle. The FEM model showed a similar deviation from its 'idealized' surface as shown earlier in figure 3.23. Since the FEM model also shows this deviation, there is little chance that an external factor is responsible for this observation. This in fact shows that with this shape-shifting method an ideal minimal surface can be approximated, but the surface will never form an exact minimal surface. An explanation for this difference is the fact that a minimal surface has a constant surface tension for the complete surface [23] [27]. This constant surface tension can be created in thin liquid films such as soap films. This constant surface tension can, however, not be created in the solid SMP's that are constrained by a frame, which subsequently results in the observed deviation. This explanation is substantiated by the FEM model,

whose stress analysis clearly shows that the tension in the surface of the SMP is not constant (section 3.5.2). Next to the Hausdorff distance, this deviation from a perfect minimal surface could also be observed by the earlier discussed H_{RMS} . For a minimal surface, the H_{RMS} would be zero everywhere. The 'idealized' patches indeed show a mean curvature of zero for the complete patch (shown in appendix D.2).

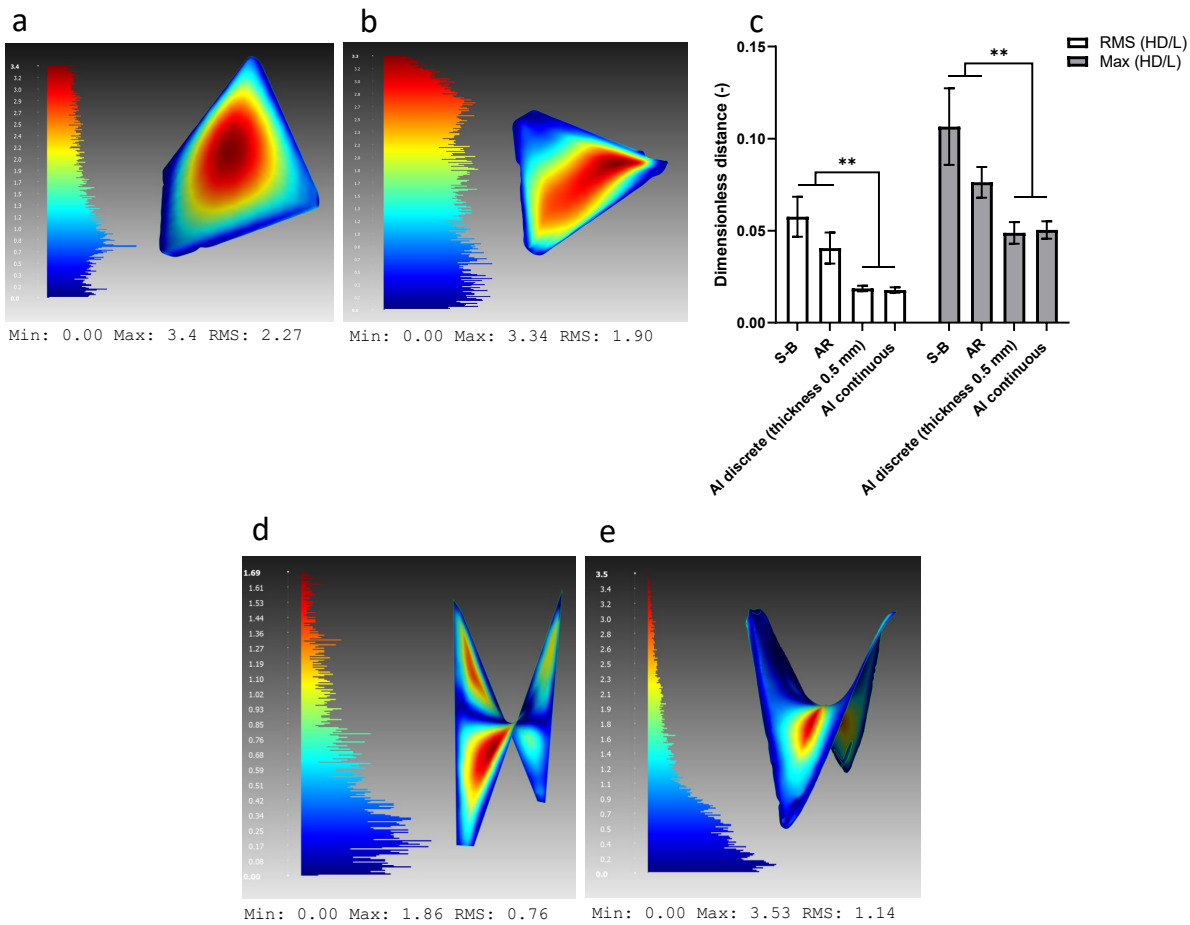


Figure 4.5: a: Hausdorff distance between the S-B isotropic foil patch and its 'idealized' surface. b: Hausdorff distance between the AR isotropic foil patch and its 'idealized' surface. c: Max and RMS of the Hausdorff distance for different patch types, both distances are made dimensionless by dividing them with the length of the patch. d: Hausdorff distance between the Al discrete patch and its 'idealized' surface. e: Hausdorff distance between the Al continuous patch and its 'idealized' surface. $p < 0.05, p < 0.01$. Note: for the S-B patch, the frame with a stiffness of 9400 N/m for both hinge types was selected and for the Al discrete patch the frame with a thickness of 2 mm and 0.5 mm. The Al continuous patch with $C_d = 2.63 \cdot 10^{-4}$ is shown. For all patches in this figure the isotropic foil or isotropic sheet SMP was used.

4.4. Measuring hyperbolic shape-shifted patches

The value of the different chosen output parameters was previously unknown. Fairly simple output parameters such as the folded corner angle and the grid analyses are self-evident. Other parameters, however, are more difficult to understand showing similarities as well as irregularities. Firstly, the sensitivity for human error is a problem for all values that are derived from the scanned patches. During the 3D-scanning process, the consistency of scanning will influence the results. Next to that, the scanned frame was deleted in the computer in order to only take the SMP surface into account. This cleaning process could influence the final results. This is why a measure such as patch area, which is completely based on the scanned patch, is quite rough and shows large deviations. It could be used to quantify the patch, but only for patches that show major differences. Quantifying differences between almost similar patches could not be accomplished with this measure. The same applies for the Hausdorff distance, the boundaries used in surface evolver in order to calculate the 'idealized' patches are coded manually into the script. Although this is done as consistently as

possible, this process could still be influenced by human error.

Next to the human error, there are similarities between different measures. Both the K_{avg} and the global principal curvatures can be considered a measure of how (hyperbolic) curved the patch's surface is. In most cases, this resemblance is also reflected in the results. An increase in both global principal curvatures, also showed a K_{avg} that is more negative. The difference between both measures and what makes them both important, however, is that the global principal curvatures can be seen as a measure of the complete patch. The K_{avg} can be seen as a zoomed-in measure of intrinsic curvature, since the Gaussian curvature is calculated for every point over a 0.3 mm radius sampled point cloud of the patch. In other words, this K_{avg} provides a quantification of intrinsic curvature with a smaller neighbourhood. By doing this, the intrinsic curvature can be measured on two completely different scales. A similar resemblance between different measures occurs for the H_{RMS} and the Hausdorff distance to the 'idealized' patch. Both are a measure of how much the patch deviates from a minimal surface with zero mean curvature. The Hausdorff distance, however, does this on a large scale for the complete patch, while the mean curvature is again calculated for every point over a 0.3 mm radius and provides a more zoomed-in value of this minimal surface deviation.

4.5. Outlook & applications

This research covers different aspects of the concept of hyperbolic shape-shifting with a rigid frame and a heat shrinkable polymer. The research, however, introduces new problems and questions that have yet to be solved. In this research, the trade-off between shrink force and the frame stiffness is introduced. However, no quantification is done for this shrink force and the precise working principle is not clear. The assumption has been made that a larger area and thickness of the SMP result in an increased shrink force. But the exact relation between those parameters remains unclear. In the research of Lui et al., it was shown that the force generated by an isotropic SMP sheet was not linearly proportional to the area of the material [37]. All samples had a height of 7.62 cm, while the width of the sheet was increased. For a doubling in sheet area, the maximum force did increase, but it did not double as shown in figure 4.6. Especially for larger areas, this increase declines. Lui et al. were the first to quantify the shrink force of sheet SMP and further study could provide more insight into the shape-shifting process.

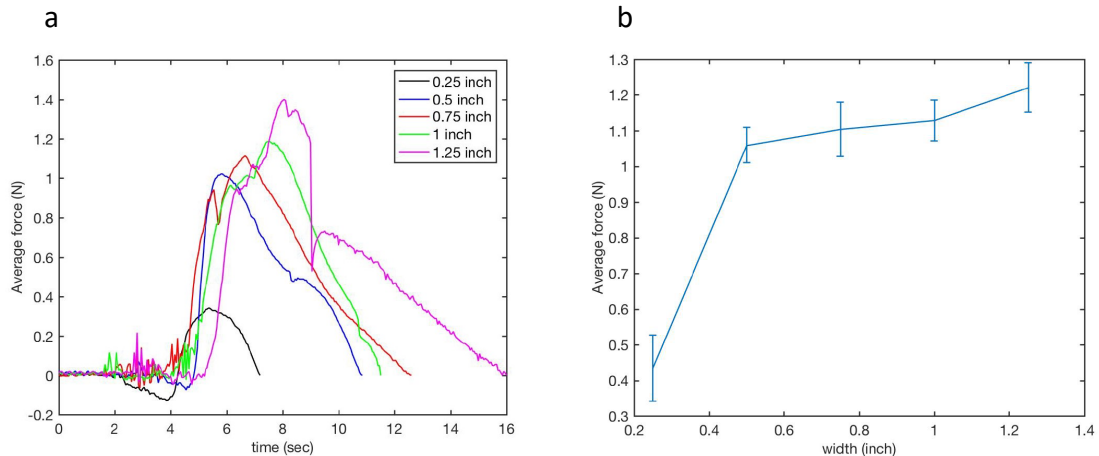


Figure 4.6: Results from the work of Liu et al [37], For an isotropic sheet SMP. During the tests, the samples are heated with a heat gun from a fixed distance. All samples have a height of 7,62 cm and a width that increases. a: The average force curve for different sample widths against time is given b: This graph shows the average maximum force generated by different sample widths. The standard deviation is given based on 10 samples.

New combinations of both the frame and SMP's should be tested in order to evaluate if similar effects occur and if the assumptions made in this research are actually correct. The thickness of the SMP could, for example, not be changed in this research, although it is expected to be of large influence on the folding process of the patch. This thickness will probably influence the scaling effects observed as well as the Euler-Plateau equilibrium. Another interesting effect of a change in SMP is that unidirectional and uneven bidirectional SMP sheets (i.o. foils) could influence the folding process. Today, however, these different materials are not yet commercially available and should be produced specifically for this application.

Analysing the effects of scaling, was one of the main objectives of this research as the concept has multiple applications in smaller (micro-scale) fields. The patch could, however, not be completely scaled as the SMP's thickness remained constant. Therefore, the SMP could only be scaled over its area, while the frame was being scaled completely by its volume. This resulted in the previously discussed scaling effects. It is expected that these effects would not occur, if the SMP was also scaled completely and not only by its area. In this case, the volume ratio between the SMP and the frame would remain constant and thus the ratio between the shrink force and the frame mass would stay constant, assuming that the shrink force of the SMP is proportional to the SMP's volume. Hans Goosen, assistant professor at the department of Precision and Microsystems Engineering at the TU Delft, also uncovered other important effects of scaling. First, the fabrication and especially the assembly of the patches would become more difficult on smaller (micro) scales. A solution for this problem could be to directly print the frames on top of the SMP's by using a 3D-printer. Another interesting aspect is the stiffness of the frame and the hinges. The stiffness of both will increase compared to the shrink force of the sheet, when down-scaling the concept. This will, in all probability, influence the folding effect of the patches as previously is shown that hinge and frame stiffness has a major influence on the shape-shifting process.

Furthermore, in this research the patch is only measured after activation. It remains unclear, however, what happens during the folding of the patch. This could, for example, be accomplished with a digital image correlation analysis (DIC). This is, however, challenging as the patch folding process takes place in a very short time span and in an oven or in boiling water. A small insight in the folding process was given by the FEM model, but it cannot be concluded with certainty that this corresponds to the folding process of the real patch. Information of this folding process could, however, be valuable for some applications of shape-shifting.

As discussed earlier, this research showed that a minimal surface can be approximated with SMP shape-shifting in combination with a rigid frame. A real minimal surface, however, can never be created with this process, because of the non-liquid behaviour and thickness of the SMP. A solution to this problem could be to separate the folding process and the minimal surface folding process by the use of two materials. One material can be responsible for the folding of the patch, while the other material is responsible for the forming of the surface. In this case the surface forming material does not need to have a high shrink force and can be relatively thin. By doing this, the shape-shifted surface could more closely approximate a minimal surface. A proof-of-concept of this idea is given in figure 4.7.

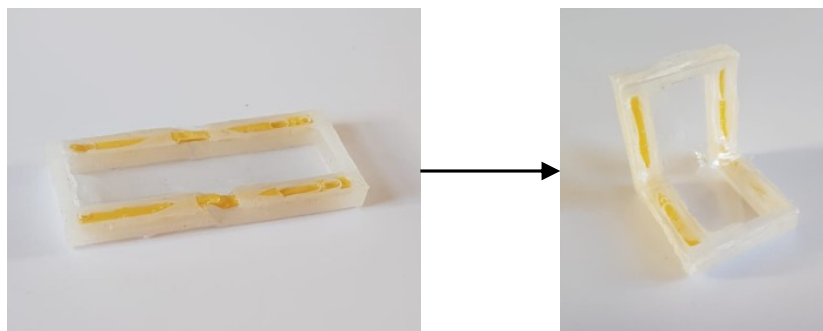


Figure 4.7: Example of two different SMP's used for the shape-shifting of hyperbolic surfaces. The strong yellow SMP is responsible for the folding of the patch, while the thin transparent SMP is responsible for the formation of the (curved) surface.

Larger and more complicated curved structures can be shape-shifted, by connecting multiple patches. In this study, effects and problems for the shape-shifting of one single patch have been revealed. It is likely that larger structures will behave differently and that different aspects such as frame mass and folding sequence will become more important. Two examples of the shape-shifting of multiple connected patches are shown in figures 4.8 and 4.9. In figure 4.8 multiple Al discrete patches are connected together and form, when activated, an extensively curved surface. The example in figure 4.9 shows that the idea introduced in the paper of Callens et al., can also be realised with the use of sheet memory polymers. Callens et al. shows in his research that TPMS structures can be created by connecting relatively simple self-folding patches, that can be formed through 2D-to-3D shape-shifting [9].

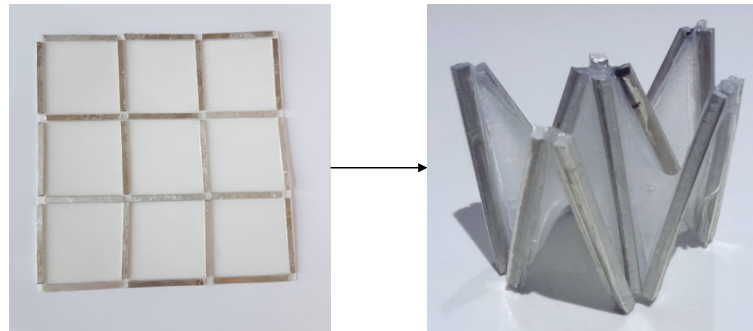


Figure 4.8: Multiple Al discrete patches connected in a square set-up form an extensively curved surface when activated.

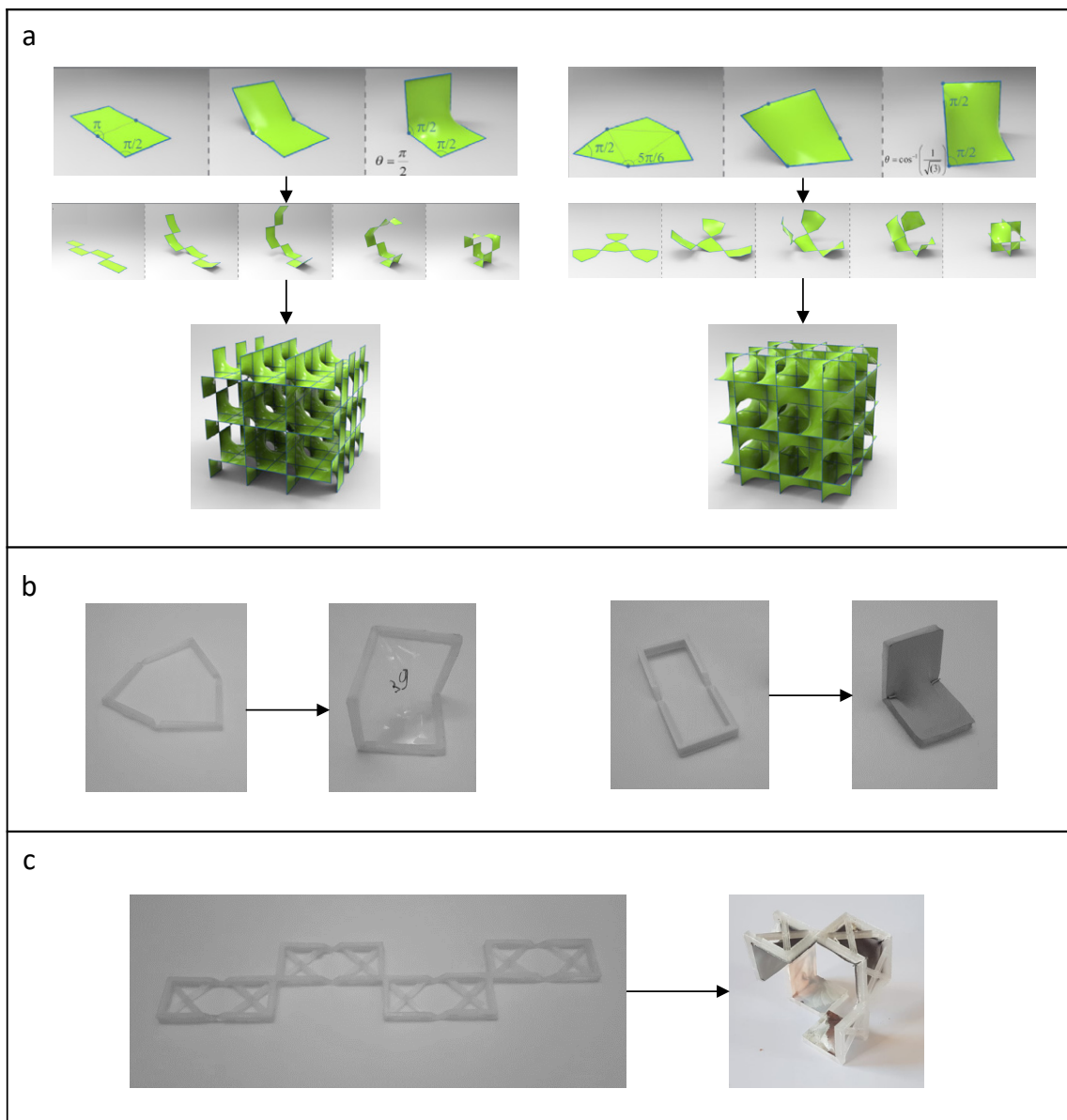


Figure 4.9: a: Realisation of the idea of Callens et al. Different complex TPMS structures can be folded by the 2D-to-3D shape shifting of relatively simple connected patches [9]. b: Example of one single shape-shifted patch with the use of a rigid frame and a SMP, based on the research of Callens et al. c: Example of multiple shape-shifted patches connected to each other, in the end large complex TPMS structures can be formed.

5

Conclusion

In this research the basic and most important principles of shape-shifting of hyperbolic surfaces are explored. This is done with the use of a passive rigid frame and an active shape memory polymer (SMP). The active SMP generates the force in order to create the deformation and movement, while the passive material determines how and where the patch will fold. A simple square patch design consisting of four rigid beams and an SMP was used as the basis of this research. When activated, this patch forms a saddle shaped surface. The design, activation and materials of the patch were changed and manipulated in different ways in order to perform a parametric study. In order to quantify and assess the quality of the patch and the effects of the manipulations, different test set-ups were made and the most valuable output parameters were chosen. Lastly, a finite element model of the concept was developed and analysed.

1. What are the different ways hyperbolic shape-shifting with rigid frame can be designed and manufactured, what are the advantages and disadvantages of these different designs? A simple square patch design consisting of four rigid beams and an SMP was used as the basis of this research. The design can be manipulated and changed in different ways. Firstly hinges can be added to the design. These hinges have a clear effect on the folding process. They not only influence how the patch folds, but also to what extent. In general, the following correlation is found: the further the patch folds and thus the more hyperbolic the shape-shifted patch becomes, the further the surface deviates from a minimal surface. Furthermore, it is shown that hinges ensure that the patch folds more uniformly, compared to patches that do not have hinges. This research also demonstrated that by changing the corner aspect ratio of the unfolded frame, the folding process can also be influenced without the use of hinges. Another important input parameter is the thickness of the frame. Below a certain thickness threshold, the frame is not stiff enough and an irregular and wrinkled surface will be formed. Inversely, when the thickness becomes too high its mass will influence the folding of the patch. When using a continuous frame (i.e. a frame that extends in the corners) an equilibrium between the stiffness of the patch and the shrink force of the sheet was created. In order to clarify this principle, a dimensionless parameter (C_d) is formulated that permits a quantification of this relationship. Lastly, the activation method forms an important consideration when fabricating shape-shifted hyperbolic surfaces. Different activation methods were discovered, each with their own (dis)advantages. In conclusion, it can be stated that it is possible to approximate a perfect minimal surface with this shape-shifting method. However, this research also shows that it is not possible to exactly resemble a minimal surface. This is attributed to the non-liquid behaviour of the SMP's.

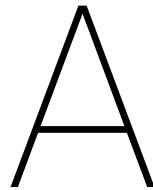
2. What are suitable materials to be used in hyperbolic shape-shifting for both the frame and sheet? The distinction can be made between the active SMP's and the rigid passive materials, also called the frame in this research. For the active materials two different main aspects play a role. Firstly, the shrink type of the material is important, or in other words, how the patch shrinks. The SMP can show uni-directional, uneven bi-directional or isotropic shrink behaviour. In this research, it is shown that in most cases the uni-directional SMP and bi-directional SMP show undesirable behaviour. A wrinkled surface is formed and the patch is skewed. The isotropic SMP's, however, let the patch fold consistently and uniformly, unless influenced by certain frame designs. The other main aspect when considering the active SMP, is its material type. The first group consists out of SMP's which are relatively thick with a high shrink percentage and a high activation tem-

perature. In this research they are called sheets. The high shrink percentage of such sheets generally results in patches that are more hyperbolic. The other materials used were foils, that are approximately ten times thinner and have a lower shrink percentage and lower activation temperature. The thinner foils alone are not able to sustain the rigidity of the patch itself. The foils can only tighten themselves between a rigid frame with hinges. Without hinges, an irregular and collapsed shape with little stiffness is obtained. The sheet material itself is strong enough to give rigidity to a patch without hinges. When selecting the frame material for the shape-shifting process, an important trade-off needs to be made. The frame material should be able to withstand the activation temperature needed to activate the SMP, in order to prevent melting or softening of the frame material. Aluminium shows to be a good example of such a material. However, fabrication of more complex frames is difficult and aluminium is relatively heavy. Therefore, in some cases it is more convenient to use other materials.

3. How can the quality of the self-folding methods be experimentally quantified, taking into account different important aspects of the shape-shifted hyperbolic surfaces? Different qualitative and quantitative measurements are introduced in order to assess the shape-shifting process. Fairly simple output parameters such as the folded corner angle, the grid analyses and the distance to the saddle point are self-evident. Other parameters, however, are more difficult to understand and show some similarities. It is shown that both the Gaussian and mean curvature of the surface can be quantified in different ways. First a zoomed-in quantification with a small neighborhood is introduced for both values, the H_{RMS} and K_{avg} . Next to that, a more global quantification is introduced to quantify both values for the complete patch. These are the global principal curvatures and RMS Hausdorff distance to the 'idealized' surface. It is expected that all four measures can also be used for surface curvature research other than shape-shifting. The limitation of all measurements used, is that the patch is only assessed after the activation. It is not taken into account what happens during the folding process. Another limitation is that the measures are sensitive for human error which could have an important undesired influence.

4. How can the basic patch design be modelled and is it possible to subsequently analyse the folding process with this model? The basic patch can be modelled in the finite element method program Abaqus. This FEM model resembles the real shape-shifted patches. The model makes it possible to analyse the stress and strain in the sheet. Large stress differences were shown in the modeled SMP surface. Around the saddle, the stress was relatively low and the negative strain almost reached its maximum shrink percentage. In the corners of the modeled patch, however, the stress was high and the strain positive, indicating that the material extends at this location. This strain analysis shows again a large resemblance to the grid analyses of the experimental patches. The stress differences found in the modeled sheet, also substantiate why a minimal surface can be approximated, but not mimicked, with the shape-shifting method. A perfect minimal surface should have a constant surface tension over the complete surface. This model makes it also possible to analyse what happens during the folding of the patch itself, as this was not possible for the experimental patches.

5. What are the difficulties and important key factors when scaling the concept? The patch could not be completely scaled as the SMP's thickness was constant. Therefore, the SMP could only be scaled over its area, while the frame was being scaled completely. This inconsistent scaling resulted in a change in volume ratio between the frame and the SMP. For a smaller scale (< 1), the volume of the sheet increased compared to the volume of the frame. This resulted in a stronger SMP and less influence by the mass of the frame. When the scale increased (> 1), the opposite effect was shown and some patches even collapsed under the mass of the frame. It is expected that this effect would not occur, if the SMP was also scaled completely and not only by its area. In this case the volume ratio between the SMP and the frame would remain constant. Other difficulties of scaling the concept would be difficulties in assembly and fabrication as well as changes in the design such as the hinges. This because, hinge stiffness will scale differently compared to the sheet force.



Decisions for basic design

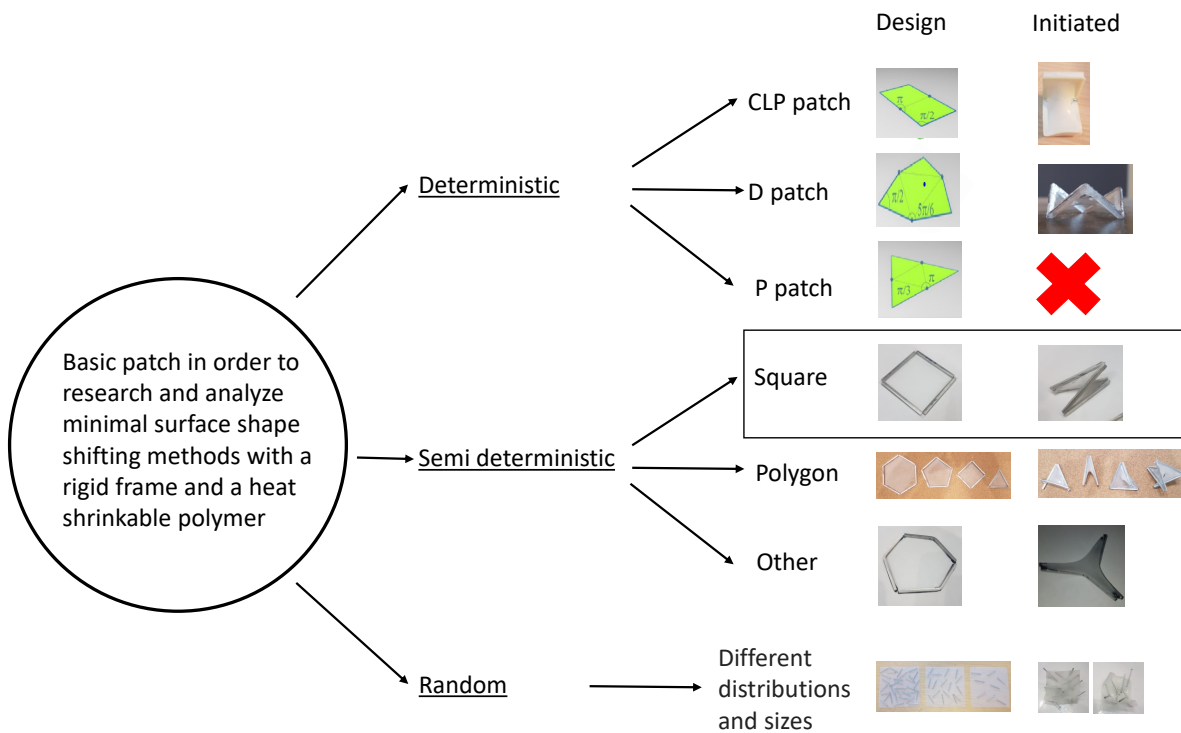


Figure A.1: Different ideas for design of the basic patch, final design is outlined in black.

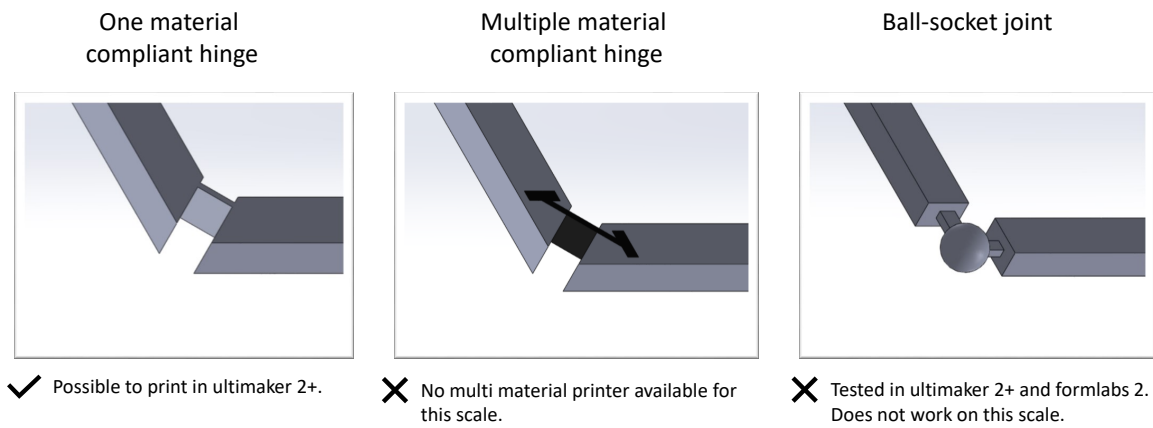


Figure A.2: Three main ideas for hinges in the basic patch. The one material compliant hinge is chosen as it is the only one that can be 3D printed in this scale.

Submerge in water



- + Uniform heating
- Max 100 °C
- No sequential folding

Hot air (oven)



- + Uniform heating (thick patches)
- No sequential folding

Hot air (heat gun)



- + Possibility sequential folding
- Uniform heating difficult

IR lamp



- + Easy sequential folding
- Uniform heating not possible

Figure A.3: four main ideas for activation of the pre-stressed shape memory polymer sheets, with their main advantages and disadvantages. For our experiments the decision is made to use "the submerge in water" or "oven method", Depending on the SMP sheet used

B

Test matrix for different patch groups

Table B.1: Here the complete test matrix for the printed patch is shown. All changing input parameters are documented. All other constant values for the experiment can be found in the methodology.

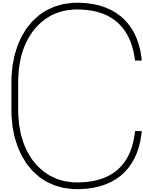
Combination #	Hinge type (1-4)	Hinge type (2-3)	Hinge stiffness (1-4) (N/m)	Hinge stiffness (2-3) (N/m)	Pre-stressed SMP material
1	bend	slide	+9400	+9400	Isotropic foil
2	bend	slide	+9400	+1400	Isotropic foil
3	bend	slide	+44400	+9400	Isotropic foil
4	bend	slide	+44400	+1400	Isotropic foil
5	rotation	rotation	+1300	+1300	Isotropic foil
6	rotation	rotation	+1300	+1300	Bi-directional foil
7	rotation	rotation	+1300	+1300	Uni-directional foil
8	no hinge	no hinge	-	-	Isotropic foil
9	no hinge	no hinge	-	-	Bi-directional foil
10	no hinge	no hinge	-	-	Uni-directional foil

Table B.2: An overview of all different input parameter combinations for the continuous aluminium patch and their corresponding C_d . All changing parameters are documented. All other constant input values for the experiment can be found in the methodology.

Combination #	Length (mm)	Thickness frame (mm)	Width frame (mm)	C_d
1	45	0.5	3	$7.95 \cdot 10^{-4}$
2	60	0.5	4	$4.48 \cdot 10^{-4}$
3	80	0.5	5	$2.36 \cdot 10^{-4}$
4	100	0.5	6	$1.45 \cdot 10^{-4}$
5	45	0.1	3	$6.37 \cdot 10^{-6}$

Table B.3: Here the complete test matrix for the aluminium discrete patch is shown. All changing input parameters are documented. All other constant values for the experiment can be found in the methodology.

Combination #	Hinge thickness (1-4)	Hinge thickness (2-3)	Width (mm) : Thickness (mm)	Bar length (mm)	Corner aspect ratio	Sheet orientation (°)	Sheet activation temperature (°C)	Sheet activation time (sec)	Beam orientation	Pre-stressed SMP material
1	0	0	3:2	45	90:90	Perpendicular	170	60	below	Isotropic sheet
2	0	0	3:2	20	90:90	Perpendicular	170	60	below	Isotropic sheet
3	0	0	3:2	70	90:90	Perpendicular	170	60	below	Isotropic sheet
4	0	0	1.5:1	20	90:90	Perpendicular	170	60	below	Isotropic sheet
5	0	0	6:4	70	90:90	Perpendicular	170	60	below	Isotropic sheet
6	0	0	3:0.1	45	90:90	Perpendicular	170	60	below	Isotropic sheet
7	0	0	3:0.3	45	90:90	Perpendicular	170	60	below	Isotropic sheet
8	0	0	3:0.5	45	90:90	Perpendicular	170	60	below	Isotropic sheet
9	0	0	3:1	45	90:90	Perpendicular	170	60	below	Isotropic sheet
10	0	0	3:4	45	90:90	Perpendicular	170	60	below	Isotropic sheet
11	0	0	3:2	45	90:90	45 degrees	170	60	below	Isotropic sheet
12	0	0	3:2	45	90:90	Perpendicular	170	60	above	Isotropic sheet
13	0	0	3:2	45	110:70	Perpendicular	170	60	below	Isotropic sheet
14	0	0	3:2	45	45:135	Perpendicular	170	60	below	Isotropic sheet
15	0	0	3:2	45	90:90	Perpendicular	190	60	below	Isotropic sheet
16	0	0	3:2	45	90:90	Perpendicular	190	30	below	Isotropic sheet
17	0	0	3:2	45	90:90	Perpendicular	170	120	below	Isotropic sheet
18	0	0	3:2	45	90:90	Perpendicular	170	30	below	Isotropic sheet
19	0	0	3:2	45	90:90	Perpendicular	150	60	below	Isotropic sheet
20	0	0	3:2	45	90:90	Perpendicular	150	120	below	Isotropic sheet
21	0	0	3:2	45	90:90	Perpendicular	130	120	below	Isotropic sheet



Additional experiments

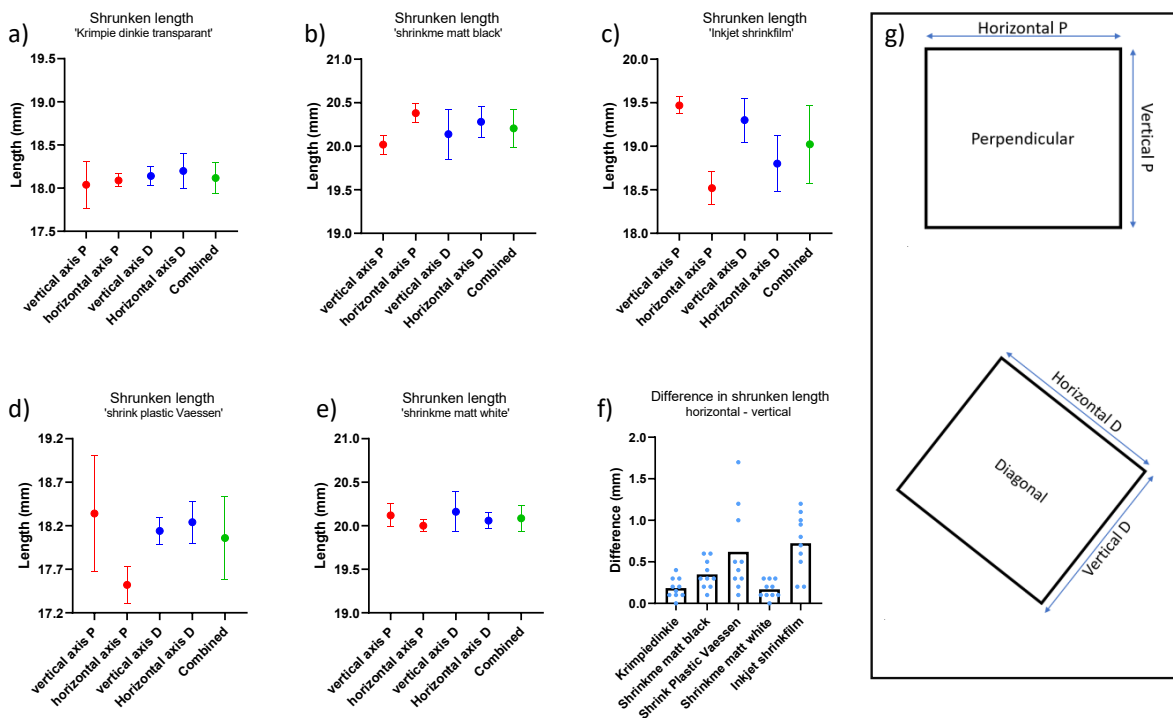


Figure C.1: Initially five isotropic sheet materials were found. In order to find the most ideal isotropic sheet material for the experiments all sheets were initiated at their ideal temperature. The experiment was conducted in the same way as the other SMP validation tests explained in the methodology 2.3.a-e shows the shrunken length of the different isotropic sheets. It clearly shows that the length of the 'Shrinkme matt white' material is the most constant and the closest to each other. This is also shown in f where the differences between the vertical and horizontal axis are shown for each material. This is why the Shrinkme matt white is chosen as the optimal isotropic sheet material and is used in the rest of the paper. For the foil materials this validation was not needed as only one material for each type was found. g shows how the different lengths are measured.

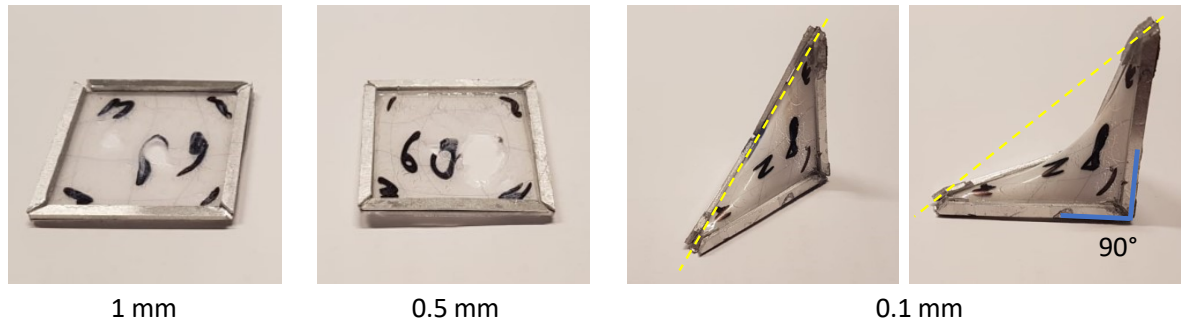
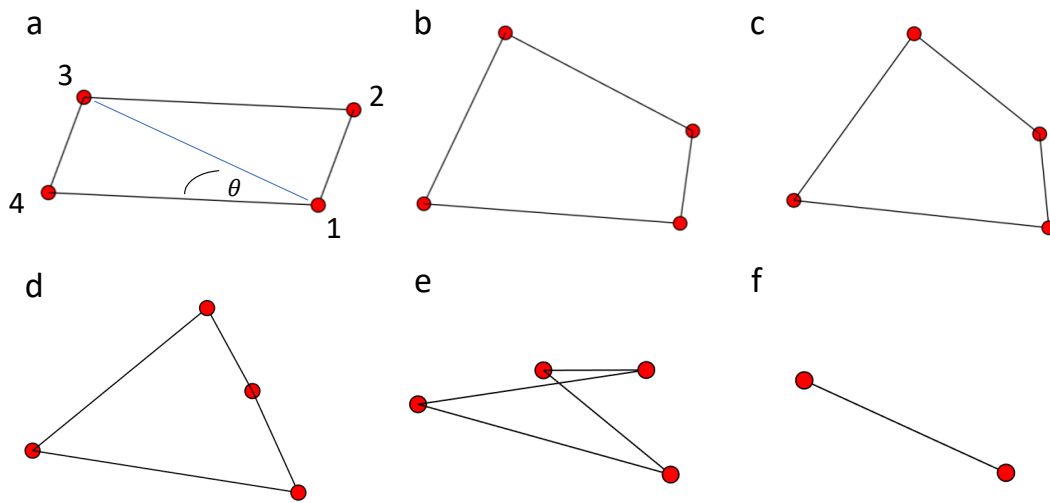


Figure C.2: Simple hinge with different thicknesses made for aluminium basic patch. Shows that only one hinge pair will bend, while the other pair stays 90° . This shows that slide-bend hinges are needed and is due to the fact that the basic patch has a different bending axis. By changing the thickness of this hinge, the extent the corner pair bends can be changed. For higher thicknesses the patch does not bend at all.

D

Other



$$\mathbf{z}_1 = [0,0,0]$$

$$\mathbf{z}_2 = [\sin \theta, \cos \theta, 0]$$

$$\mathbf{z}_3 = \left[0, \frac{\cos(2\theta) - \sin^2(\theta)}{-\cos \theta} + \cos \theta, \sqrt{1 - \sin^2(\theta) - (\mathbf{z}_{3y}^* - \cos(\theta))^2} \right]$$

$$\mathbf{z}_4 = [-\sin \theta, \cos \theta, 0]$$

$$\mathbf{z}_{3y}^* = \frac{\cos(2\theta) - \sin^2(\theta)}{-\cos \theta} + \cos \theta$$

Figure D.1: Kinematic approach of basic patch with 4 equal corners in every position.

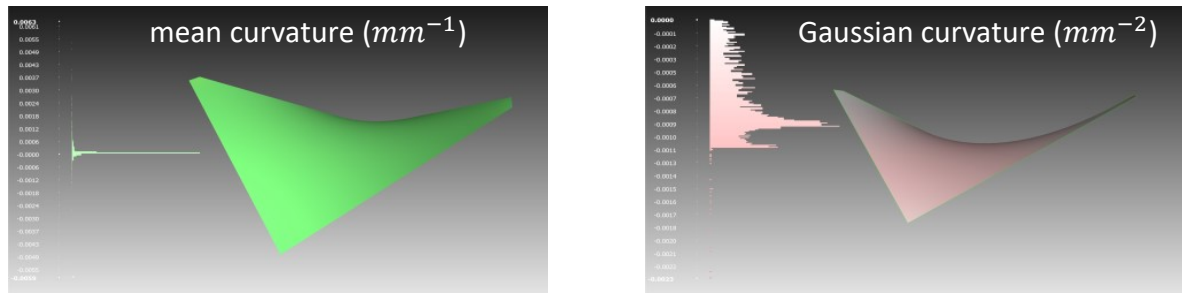


Figure D.2: Example of mean curvature(mm^{-1}) and Gaussian curvature(mm^{-2}) of "idealized patch", constructed in surface evolver. This example is based on outer boundaries of the bend-slide hinge 3D-printed patch (Bend hinge: 9400 N/m, Slide hinge: 9400 N/m). It substantiates that the mean curvature is indeed zero, for every element on the 'idealized' patch.

Bibliography

- [1] S. Alben, B. Balakrisnan, and E. Smela. Edge Effects Determine the Direction of Bilayer Bending. *Nano Letters*, 11(6):2280–2285, 2011.
- [2] N. Aspert, D. Santa-Cruz, and T. Ebrahimi. Mesh: Measuring errors between surfaces using the Hausdorff distance. *Proceedings. IEEE International Conference on Multimedia and Expo*, 1:705–708, 2002.
- [3] N.D. Bade, T. Xu, R.D. Kamien, R.K. Assoian, and K.J. Stebe. Gaussian Curvature Directs Stress Fiber Orientation and Cell Migration. *Biophysical Journal*, 114(6):1467–1476, 2018.
- [4] C. Blum. *Curvotaxis and Pattern Formation in the Actin Cortex of Motile Cells*. PhD thesis, Department of Physics of Biological and Complex Systems, Georg-August University School of Science, 2015.
- [5] K.A. Brakke. The Surface Evolver. *Experimental Mathematics*, 1(2):141–165, 1992.
- [6] M.L. Brongersma, Y. Cui, and S. Fan. Light management for photovoltaics using high-index nanostructures. *Nature Materials*, 13(5):451–460, 2014.
- [7] R. Budynas and K. Nisbett. *Shigley's Mechanical Engineering Design*. McGraw-Hill Science, 8th edition, 2006.
- [8] S.J.P. Callens and A.A. Zadpoor. From flat sheets to curved geometries: Origami and kirigami approaches. *Materials Today*, 21(3):241–264, 2018.
- [9] S.J.P. Callens, N. Tümer, and A.A. Zadpoor. Hyperbolic origami-inspired folding of triply periodic minimal surface structures. *Applied Materials Today*, 15:453–461, 2019.
- [10] S.J.P. Callens, R.J.C. Uyttendaele, L.E. Fratila-Apachitei, and A.A. Zadpoor. Substrate curvature as a cue to guide spatiotemporal cell and tissue organization. *Biomaterials*, 232:119739, 2020.
- [11] Z. Chen, X. Jiang, and X. Zhang. Damped circular hinge with integrated comb-like substructures. *Precision Engineering*, 53:212–220, 2018.
- [12] P. Cignoni, C. Rocchini, and R. Scopigno. Metro: Measuring Error on Simplified Surfaces. *Computer Graphics Forum*, 17(2):167–174, 1998.
- [13] P. Cignoni, M. Callieri, M. Corsini, M. Dellepiane, F. Ganovelli, and G. Ranzuglia. MeshLab: an Open-Source Mesh Processing Tool. *Eurographics Italian Chapter Conference, The Eurographics Association*, 1: 129–136, 2008.
- [14] C. Comte and J. von Stebut. Microprobe-type measurement of Young's modulus and Poisson coefficient by means of depth sensing indentation and acoustic microscopy. *Surface and Coatings Technology*, 154(1):42–48, 2002.
- [15] M. Corsini, P. Cignoni, and R. Scopigno. Efficient and flexible sampling with blue noise properties of triangular meshes. *IEEE Transactions on Visualization and Computer Graphics*, 18(6):914–924, 2012.
- [16] J. Cui, F.R. Poblete, and Y. Zhu. Origami/Kirigami-Guided Morphing of Composite Sheets. *Advanced Functional Materials*, 28(44):1802768, 2018.
- [17] D. Davis, R. Mailen, J. Genzer, and M.D. Dickey. Self-folding of polymer sheets using microwaves and graphene ink. *RSC Advances*, 5(108):89254–89261, 2015.
- [18] U. Dierkes, S. Hildebrandt, A. Küster, and O. Wohlrab. *Minimal Surfaces I*, volume 295 of *Grundlehren der mathematischen Wissenschaften*. Springer Berlin Heidelberg, 1992.

- [19] D.E. Discher, P. Janmey, and Y.L. Wang. Tissue cells feel and respond to the stiffness of their environment. *Science*, 10:1139–1143, 2005.
- [20] S. Dobbenga, L.E. Fratila-Apachitei, and A.A. Zadpoor. Nanopattern-induced osteogenic differentiation of stem cells – A systematic review. *Acta Biomaterialia*, 46:3–14, 2016.
- [21] J. G. Drobný. *Handbook of Thermoplastic Elastomers*. Elsevier Inc., 2nd edition, 2014.
- [22] A. Elbourne, R.J. Crawford, and E.P. Ivanova. Nano-structured antimicrobial surfaces: From nature to synthetic analogues. *Journal of Colloid and Interface Science*, 508:603–616, 2017.
- [23] J.C. Eriksson and S. Ljunggren. The Mechanical surface tension and stability of minimal surface structures. *Journal of Colloid And Interface Science*, 167(2):227–231, 1994.
- [24] L. Giomi and L. Mahadevan. Minimal surfaces bounded by elastic lines. *Proceedings of the Royal Society A: Mathematical, Physical and Engineering Sciences*, 468(2143):1851–1864, 2012.
- [25] L.T. de Haan, C. Sánchez-Somolinos, C.M.W. Bastiaansen, A.P.H.J. Schenning, and D.J. Broer. Engineering of Complex Order and the Macroscopic Deformation of Liquid Crystal Polymer Networks. *Angewandte Chemie International Edition*, 51(50):12469–12472, 2012.
- [26] G.A. Hansen, R.W. Douglass, and A. Zardecki. *Mesh Enhancement: Selected Elliptic Methods, Foundations And Applications*. Imperial College Press, 2005.
- [27] T. Hoang and E. Fried. Influence of a spanning liquid film on the stability and buckling of a circular loop with intrinsic curvature or intrinsic twist density. *Mathematics and Mechanics of Solids*, 23(1):43–66, 2018.
- [28] W. Hu, G.Z. Lum, M. Mastrangeli, and M. Sitti. Small-scale soft-bodied robot with multimodal locomotion. *Nature*, 554(7690):81–85, 2018.
- [29] S. Janbaz, R. Hedayati, and A.A. Zadpoor. Programming the shape-shifting of flat soft matter: From self-rolling/self-twisting materials to self-folding origami. *Materials Horizons*, 3(6):536–547, 2016.
- [30] H. Jinnai, Y. Nishikawa, M. Ito, S.D. Smith, D.A. Agard, and R.J. Spontak. Topological Similarity of Sponge-like Bicontinuous Morphologies Differing in Length Scale. *Advanced Materials*, 14(22):1615–1618, 2002.
- [31] H. Jinnai, H. Watashiba, T. Kajihara, Y. Nishikawa, M. Takahashi, and M. Ito. Surface curvatures of trabecular bone microarchitecture. *Bone*, 30(1):191–194, 2002.
- [32] S.C. Kapfer, S.T. Hyde, K. Mecke, C.H. Arns, and G.E. Schröder-Turk. Minimal surface scaffold designs for tissue engineering. *Biomaterials*, 32(29):6875–6882, 2011.
- [33] M. Kazhdan and H. Hoppe. Screened poisson surface reconstruction. *ACM Transactions on Graphics*, 32(3):1–13, 2013.
- [34] P.S. Laplace. *Traite de mecanique celeste, De l'attraction et de la repulsion des spheres, et des lois de l'equilibre et du mouvement des fluides elastiques*. l'Imprimerie de Crapelet 1799, 1825.
- [35] S.J. Lee and S. Yang. Micro glass ball embedded gels to study cell mechanobiological responses to substrate curvatures. *Review of Scientific Instruments*, 83(9):094302, 2012.
- [36] A. Lendlein and R. Langer. Biodegradable, elastic shape-memory polymers for potential biomedical applications. *Science*, 296(5573):1673–1676, 2002.
- [37] J. Liu, J.C.C. Liu, M. Eggers, and J.E. Sabin. Responsive Kirigami: Context-Actuated Hinges in Folded Sheet Systems. *Proceedings of the Symposium on Simulation for Architecture and Urban Design*, (22): 1–8, 2018.
- [38] Y. Liu, J.K. Boyles, J. Genzer, and M.D. Dickey. Self-folding of polymer sheets using local light absorption. *Soft Matter*, 8(6):1764–1769, 2012.
- [39] R.W. Mailen, Y. Liu, M.D. Dickey, M. Zikry, and J. Genzer. Modelling of shape memory polymer sheets that self-fold in response to localized heating. *Soft Matter*, 11(39):7827–7834, 2015.

- [40] R.W. Mailen, Y. Liu, M.D. Dickey, M. Zikry, and J. Genzer. Supplemental information: Modeling of shape memory polymer sheets that self-fold in response to localized heating. Technical report, Soft matter, 2015.
- [41] T. van Manen, S. Janbaz, and A.A. Zadpoor. Programming 2D/3D shape-shifting with hobbyist 3D printers. *Materials Horizons*, 4(6):1064–1069, 2017.
- [42] T. van Manen, S. Janbaz, and A.A. Zadpoor. Programming the shape-shifting of flat soft matter. *Materials Today*, 21(2):144–163, 2018.
- [43] E.G. Merriam, J.E. Jones, and L.L. Howell. Design of 3D-Printed Titanium Compliant Mechanisms. Technical report, NASA, 2014.
- [44] C.K.M. Ng and K.N. Yu. Proliferation of epithelial cells on PDMS substrates with micropillars fabricated with different curvature characteristics. *Biointerphases*, 7(1-4):1–8, 2012.
- [45] M. Nikkhah, F. Edalat, S. Manoucheri, and A. Khademhosseini. Engineering microscale topographies to control the cell-substrate interface. *Biomaterials*, 33(21):5230–5246, 2012.
- [46] C. Ohm, M. Brehmer, and R. Zentel. Liquid Crystalline Elastomers as Actuators and Sensors. *Advanced Materials*, 22(31):3366–3387, 2010.
- [47] A. Papadopoulou, J. Laucks, and S. Tibbits. From Self-Assembly to Evolutionary Structures. *Architectural Design*, 87(4):28–37, 2017.
- [48] L. Pieuchot, J. Marteau, A. Guignandon, T. Dos Santos, I. Brigaud, P.F. Chauvy, T. Cloatre, A. Ponche, T. Petithory, P. Rougerie, M. Vassaux, J.L. Milan, N. Tusamda Wakhloo, A. Spangenberg, M. Bigerelle, and K. Anselme. Curvotaxis directs cell migration through cell-scale curvature landscapes. *Nature Communications*, 9:3995, 2018.
- [49] W.D. Pilkey. *Formulas for Stress, Strain, and Structural Matrices*. Wiley, 2nd edition, 2008.
- [50] M. Smith. *ABAQUS/Standard User's Manual*. Dassault Systèmes Simulia Corp, 6.9th edition, 2019.
- [51] S. Tibbits. 4D Printing: Multi-Material Shape Change. *Architectural Design*, 84(1):116–121, 2014.
- [52] M.T. Tolley, S.M. Felton, S. Miyashita, D. Aukes, D. Rus, and R.J. Wood. Self-Folding Origami: Shape Memory Composites Activated by Uniform Heating. *Smart Materials and Structures*, 23(9):094006, 2014.
- [53] X. Trepas, L. Deng, S.S. An, D. Navajas, D.J. Tschumperlin, W.T. Gerthoffer, J.P. Butler, and J.J. Fredberg. Universal physical responses to stretch in the living cell. *Nature*, 447(7144):592–595, 2007.
- [54] Ultimaker. Technical and safety material data sheets. Retrieved October 10, 2019, from <https://ultimaker.com/en/resources/50461-technical-and-safety-data-sheets>.
- [55] G. Wang, H. Yang, Z. Yan, N.G. Ulu, Y. Tao, J. Gu, L.B. Kara, and L. Yao. 4D Mesh: 4D printing morphing non-developable mesh surfaces. *UIST 2018 - Proceedings of the 31st Annual ACM Symposium on User Interface Software and Technology*, pages 623–635, 2018.
- [56] L. Wang, S. Di, W. Wang, H. Chen, X. Yang, T. Gong, and S. Zhou. Tunable Temperature Memory Effect of Photo-Cross-Linked Star PCL–PEG Networks. *Macromolecules*, 47(5):1828–1836, 2014.
- [57] M. Werner, S.B.G. Blanquer, S.P. Haimi, G. Korus, J.W.C. Dunlop, G.N. Duda, D.W. Grijpma, and A. Petersen. Surface Curvature Differentially Regulates Stem Cell Migration and Differentiation via Altered Attachment Morphology and Nuclear Deformation. *Advanced Science*, 4(2):1600347, 2017.
- [58] M. Werner, N.A. Kurniawan, G. Korus, C.V.C. Bouten, and A. Petersen. Mesoscale substrate curvature overrules nanoscale contact guidance to direct bone marrow stromal cell migration. *Journal of the Royal Society Interface*, 15(145):162, 2018.
- [59] Q. Xiao-dong and Y. Wang. Novel techniques for the preparation of shape-memory polymers, polymer blends and composites at micro and nanoscales. In *Shape Memory Polymers, Blends and Composites, Advanced Structured Materials*, volume 115, pages 53–83. Springer, 2020.

-
- [60] A.A. Zadpoor. Bone tissue regeneration: The role of scaffold geometry. *Biomaterials Science*, 3:231–245, 2015.
- [61] A.A. Zadpoor. Meta-biomaterials. *Biomaterials Science*, 8:18–38, 2020.
- [62] Q. Zhao, H.J. Qi, and T. Xie. Recent progress in shape memory polymer: New behavior, enabling materials, and mechanistic understanding. *Progress in Polymer Science*, 49-50:79–120, 2015.
- [63] J. Zhou and S.S. Sheiko. Reversible shape-shifting in polymeric materials. *Journal of Polymer Science Part B: Polymer Physics*, 54(14):1365–1380, 2016.